

MARKKU JÄRVELÄ

Cloud Enhancement Phenomenon

Characteristics of overirradiance events and
their effect on photovoltaic power generation

MARKKU JÄRVELÄ

Cloud Enhancement Phenomenon
Characteristics of overirradiance events and
their effect on photovoltaic power generation

ACADEMIC DISSERTATION

To be presented, with the permission of
the Faculty of Information Technology and Communication Sciences
of Tampere University,
for public discussion in the S2
of Sähkötalo, Korkeakoulunkatu 3, Tampere,
on 1 September 2023, at 12 o'clock.

ACADEMIC DISSERTATION

Tampere University Faculty of Information Technology and Communication Sciences
Finland

*Responsible
supervisor
and Custos*

Professor
Seppo Valkealahti
Tampere University
Finland

Pre-examiners

Professor
Alexandros Charalambides
Cyprus University of Technology
Cyprus

Professor
Kimmo Kauhaniemi
University of Vaasa
Finland

Opponent

Professor
Samuli Honkapuro
LUT University
Finland

The originality of this thesis has been checked using the Turnitin OriginalityCheck service.

Copyright ©2023 author

Cover design: Roihu Inc.

ISBN 978-952-03-2969-3 (print)

ISBN 978-952-03-2970-9 (pdf)

ISSN 2489-9860 (print)

ISSN 2490-0028 (pdf)

<http://urn.fi/URN:ISBN:978-952-03-2970-9>



Carbon dioxide emissions from printing Tampere University dissertations have been compensated.

PunaMusta Oy – Yliopistopaino
Joensuu 2023

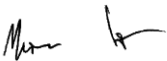
PREFACE

This dissertation was prepared at Tampere University of Technology and Tampere University between years 2017 and 2022. The research work was mainly funded by Finnish Solar Revolution and Solar X projects by Business Finland.

First and foremost, I want to express my deepest gratitude to Professor Seppo Valkealahti for supervising my dissertation and providing guidance and support throughout this long journey. I am also thankful for D.Sc. (Tech.) Kari Lappalainen who helped me with my initial steps in my research work. I would also like to thank Professor Emeritus Teuvo Suntio, D.Sc. (Tech.) Aapo Aapro, D.Sc. (Tech.) Jyri Kivimäki, D.Sc. (Tech.) Matias Berg, D.Sc. (Tech) Jenni Rekola, D.Sc. (Tech) Tuomas Messo, M.Sc. Roosa-Maria Sallinen, M.Sc. Antti Hildén, M.Sc. Heidi Kalliojärvi-Viljakainen, and all the other friends and former colleagues. You made my stay at the university truly memorable. I will never forget you nor the interesting discussions on professional matters, life, and stuff. I am also thankful for all my friends and former colleagues at ABB Oy Solar Inverters. Without you, I would have never started this project.

Finally, one should never forget family and friends who are an endless source of support and encouragement. I am especially thankful for Ava and Henri who have filled my life with sunshine and joy. And most importantly, thank you, Irene. I would have never finished this project without your love and unwavering support — and constant reminders that I should have been done with this a long, long time ago.

Hyvinkää, May 2023

A handwritten signature in black ink, appearing to be 'Matti' followed by a stylized flourish.

ABSTRACT

While the cloud enhancement (CE) of solar irradiance is a well-known phenomenon, its effects on the operation of photovoltaic (PV) power plants have not been thoroughly analyzed. The maximum power point (MPP) power of a PV generator depends mainly on irradiance; therefore, if it is enhanced, the actual MPP power can occasionally exceed the nominal nameplate power. This dissertation analyzes overirradiance and overpower events caused by the CE phenomenon from a PV power generation point of view. The analyses are based on irradiance measurement data from an array of irradiance sensors, and PV panel operating and ambient temperature data.

The diameters of overirradiance areas are typically several tens of meters, and at maximum they can be several kilometers so that they can affect the operation of all PV power plants sizes. The diameter and occurrence of overirradiance events decreases with increasing irradiance. The diameter of the strongest overirradiance areas is of the order of some tens of meters. The duration of the overirradiance events varies typically from some seconds to some tens of seconds, and at maximum they can be several minutes. The size of the photovoltaic generator was not found to affect the maximum duration of the events, but the occurrence and irradiance decreases with increasing PV generator size.

The duration of overpower events is typically from some seconds to some tens of seconds, and at maximum, it can be several minutes. Because the decrease of the operating temperature of PV panels increases the open circuit voltage, the shade periods preceding the overirradiance events were found to be prerequisites for the strongest overpower events. Overpower events increase the operating voltage, because photovoltaic power systems are operating in power-limiting mode during them. Because the duration of the most extreme overpower events is short, the increase of operating voltage does not unduly affect the lifetimes and operation of system components.

TIIVISTELMÄ

Pilvien auringonsäteilyä vahvistava vaikutus on yleisesti tiedostettu ilmiö, mutta sen vaikutuksia aurinkosähkövoimalaitoksen toimintaan ei ole tutkittu kattavasti. Aurinkosähkövoimalan maksimitehopisteen teho riippuu lähinnä säteilyvoimakkuudesta. Jos säteilyvoimakkuus on odotettua korkeampi, voimalan maksimitehopisteen teho voi olla ajoittain korkeampi kuin voimalan nimellinen teho. Tämä väitöskirja analysoi pilvivahvistusilmiöstä johtuvien auringonsäteilyn vahvistusalueiden ja aurinkosähkövoimalaitosten ylitehotapahtumien ominaisuuksia. Tulokset perustuvat auringon säteilytehon mittauksiin usealla anturilla, sekä ympäristön ja aurinkopaneelien toimintalämpötilan mittauksiin.

Pilvivahvistusilmiön aiheuttamien säteilyvahvistusalueiden halkaisijat ovat tyypillisesti useita kymmeniä metrejä ja enimmillään useita kilometrejä, eli ne voivat vaikuttavaa kaiken kokoisten aurinkosähkövoimalaitosten toimintaan. Vahvistusalueiden halkaisijat ja esiintyvyys kuitenkin pienenee mitä voimakkaammasta tapahtumasta on kyse. Voimakkaimpien vahvistusalueiden halkaisijat ovat joitakin kymmeniä metrejä. Vahvistustapahtumien kesto on tyypillisesti useista sekunneista joihinkin kymmeniin sekunteihin, ja enimmillään näiden kesto voi olla useita minuutteja. Aurinkosähköjärjestelmän koon ei havaittu vaikuttavan vahvistustapahtumien maksimikeston, mutta tapahtumien esiintyvyys pienenee voimalaitoksen koon kasvaessa. Myös säteilyn voimakkuus pienenee voimalaitoksen koon kasvaessa.

Ylitehotapahtumien kesto on tyypillisesti useista sekunneista joihinkin kymmeniin sekunteihin, ja pisimmillään ne voivat olla joitakin minuutteja. Koska paneelin toimintalämpötilan laskeminen kasvattaa sen toimintajännitettä, auringon säteilyn vahvistustapauksia edeltävien varjojaksojen havaittiin olevan edellytys kaikkein voimakkaimmille ylitehotapahtumille. Ylitehotapahtumat nostavat entisestään paneelien toimintajännitettä, koska aurinkosähköjärjestelmä toimii näiden aikana tehonrajoitustilassa. Koska ylitehotapahtumat ovat kestoltaan lyhyitä, toimintajännitteiden nousulla ei ole merkittävää vaikutusta komponenttien elinikään tai toimintaan.

CONTENTS

1	Introduction	1
2	Theoretical background.....	9
2.1	Operation of PV cells.....	9
2.2	Construction and control of PV power systems	14
2.3	Solar irradiance	28
3	Research data	30
3.1	Measurement system	30
3.2	Measurement data.....	32
3.3	Data quality assurance.....	34
3.4	Cloud shadow speed data	37
4	Research methods	39
4.1	Determining overirradiance event characteristics	39
4.2	Determining the effect of overirradiance events on PV generators and PV power plants.....	49
4.3	Analysis of the overirradiance and overpower events	53
5	Characteristics of overirradiance events.....	57
5.1	Occurrence and diameters of overirradiance areas	57
5.2	Occurrence and durations of overirradiance events over land areas of PV generators of different sizes	61
5.3	Possible effects on the operation of PV generators.....	65
6	Overpower events caused by the cloud enhancement phenomenon.....	67
6.1	Characteristics of the overpower events	67
6.2	Operation of the PV power plant during overpower events.....	74
6.3	Possible effects on the operation of solar inverters.....	82
7	Conclusion.....	86
	APPENDIX A. PV panel simulink model.....	99

APPENDIX B. Matlab functions	102
------------------------------------	-----

SYMBOLS AND ABBREVIATIONS

ABBREVIATIONS

AC	Alternating current
AM	Air mass
CE	Cloud enhancement
c-Si	Crystalline silicon
DC	Direct current
DHI	Diffuse horizontal irradiance
DNI	Direct normal irradiance
ESR	Equivalent series resistance
EVA	Ethylene vinyl acetate
GHI	Global horizontal irradiance
GTI	Global tilted irradiance
HV	High voltage
IEC	International Electrotechnical Commission
ISO	International Organization for Standardization
IGBT	Insulated-gate bipolar transistor
I3RC	Intercomparison of 3D Radiation Cores
MPP	Maximum power point
MPPT	Maximum power point tracking
MV	Medium voltage
NASA	National Aeronautics and Space Administration
NOCT	Normal operating cell temperature
P&O	Perturb and observe
PV	Photovoltaic
p.u.	Per unit
RRMSE	Relative root mean square error
STC	Standard test conditions
S1, S2, S3, ...	Irradiance sensor 1, 2, 3, etc. on Tampere University research power plant

TAU	Tampere University
T1, T2, T3, ...	Temperature sensor 1, 2, 3, etc. on Tampere University research power plant
US	United States
USA	United States of America

LATIN ALPHABET

A	Diode ideality factor
c	Speed of light in vacuum
E	Energy
E_g	Band gap energy
E_{sw}	Switching energy
E_{sw0}	Switching energy in reference conditions
G	Irradiance
G_{STC}	STC irradiance of 1000 W/m ²
h	Planck constant
I	Current
I_o	Dark saturation current
I_{o1}	Dark saturation current in quasi-neutral region
I_{o2}	Dark saturation current in depletion region
I_D	Current through diode
I_{ph}	Photocurrent
I_{MPP}	Maximum power point current
I_R	Ripple current
I_{R0}	Ripple current in reference point
I_{Ref}	Reference current
I_S	Reverse bias saturation current of a diode
I_{SC}	Short circuit current
$I_{SC, STC}$	Short circuit current in STC
I_{SH}	Current through shunt resistance
k_B	Boltzmann constant
K_I	Dependency coefficient for current
K_R	Dependency coefficient for ripple current
K_T	Dependency coefficient for temperature
K_U	Dependency coefficient for voltage

L	Lifetime
L_0	Nominal lifetime in reference conditions
n	Experimental dependency coefficient
N_S	Number of PV cells on one module
P	Power
P_{MPP}	Maximum power point power
$P_{MPP, STC}$	Maximum power point power in STC
q	Elementary charge of $1.602 \cdot 10^{-19}$ C
R_S	Series resistance
R_{SH}	Shunt resistance
T	Temperature
T_{amb}	Ambient temperature
T_{cell}	PV cell operating temperature
T_j	Junction temperature
T_{j0}	Reference junction temperature
T_{panel}	PV panel operating temperature
T_{STC}	STC temperature of 25 °C
T_0	Nominal temperature
U	Voltage
U_R	Reference voltage
U_T	Thermal voltage
U_{MPP}	Maximum power point voltage
$U_{MPP, STC}$	Maximum power point voltage in STC
U_{OC}	Open circuit voltage
$U_{OC, STC}$	Open circuit voltage in STC
U_{OP}	Operating point voltage
U_0	Nominal voltage

GREEK ALPHABET

λ	Photon wavelength
-----------	-------------------

1 INTRODUCTION

Although the photovoltaic (PV) effect was observed in 1839 (Becquerel, 1839), it was several decades before Albert Einstein explained it during his *annus mirabilis* in 1905 (Einstein, 1905), which led to him being awarded the Nobel prize in physics in 1921. The first PV cells were developed in the 1950s by Bell Labs and the United States Air Force, and one of the first practical applications was satellites, when Vanguard I was equipped with solar panels in 1958. The interest in renewables increased during the oil crisis in the 1970s, but it took until 1999 for the cumulative global installed PV capacity to reach 1 GWp. In 2018, the cumulative install base was already 500 GWp, and ever since it has been increasing by more than 100 GWp per year (REN21, 2021). The recent interest in solar PV is due to the fact that, in most parts of the world, it is already the cheapest way of producing electrical energy (International Energy Agency, 2020). To further emphasize this point, in the US it is now cheaper to build new solar PV power plants than it is to maintain and operate most of the existing coal power plants (Gimon et al., 2021).

Compared to traditional means of energy production, solar PV is intermittent in nature; that is, it is not continuously available. Because the maximum power point (MPP) power of a PV power plant depends primarily on irradiance, production varies naturally due to seasonal and daily cycles of irradiance. Because the operating principle of PV cells is based on photovoltaic effect, PV generators do not have natural inertia and the changes in irradiance are seen instantaneously on the MPP power of a PV generator. Therefore, the MPP power can occasionally have fast fluctuations due to moving cloud shadows, and even the largest multi-megawatt PV generators can ramp down from full power to 20 percent power in a matter of some tens of seconds (Javier Marcos et al., 2011). This intermittency and the increase of solar PV in the energy mix introduces problems to power grids regarding voltage and frequency stability, grid protection, flexibility, and harmonics (Gandhi et al., 2020). However, these problems can be mitigated to some extent by better forecast models, various voltage and frequency management techniques, harmonics compensation, reactive power management, adaptive protection schemes, and advanced dispatch strategies (Sampath Kumar et al., 2020).

Clouds are primarily decreasing the MPP power and total energy yield of PV generators by reducing the direct irradiance through absorption and scattering of photons. However, on partly cloudy days, clouds can occasionally boost the irradiance if conditions are favorable. This phenomenon is known as cloud enhancement (CE), but it is also referred as overirradiance or irradiance enhancement (Gueymard, 2017a). Multiple papers have reported high irradiance value measurements from all around the world at different altitudes and latitudes. For example, (Gueymard, 2017b) measured global tilted irradiance of 1998 W/m² at 40 degrees Northern latitude at an altitude of 1829 m, (Emck & Richter, 2008) measured a global horizontal irradiance of 1832 W/m² in Ecuador at the altitude of 3400 m, (do Nascimento et al., 2019) reported an overirradiance event with irradiance of 1845 W/m² at an altitude of 32 meters in Caucaia, Brazil, (Yordanov et al., 2015) measured approximately 1600 W/m² at sea level at 60 degrees of Northern latitude, and (Inman et al., 2016) measured a global horizontal irradiance of 1400 W/m² in San Diego, California.

The irradiance values reported in the above-mentioned and other publications are not always comparable because the installation arrangement and characteristics of measurement instruments can vary. For example, the irradiance value of 1998 W/m² reported in (Gueymard, 2017b) was measured with a photo-diode based irradiance sensor at a tilt angle of 40° and 1-s time resolution. In comparison, the global horizontal irradiance of this event was 1891 W/m², which is noticeably less but still a record-high value. The global horizontal irradiance of the 1832 W/m² event that was reported in (Emck & Richter, 2008) was measured with Kipp and Zonen CM3 thermopile (95% response time of 18 seconds) and 300 second (instantaneous) sampling time. The considerably slower response time of thermopile sensors in comparison to photodiode sensors introduces smoothing to the measured irradiance. This affects both up and down ramps so that the measured maximum values may be lower, the irradiance profile is wrong, or the event duration may be longer (Espinosa-Gavira et al., 2018). In addition, it is possible that due to low sampling frequency the real maximum values are not recorded, or smoothing can be introduced if time-averaged values are used instead of instantaneous values. In practice, it has been suggested that sub-second sampling frequency is needed when analyzing overirradiance events (Yordanov, Saetre, et al., 2013).

The CE phenomenon itself is well understood. In the past, it has been explained by reflections from cloud edges (Norris, 1968), but this is insufficient and overly general explanation of the complex phenomenon. The CE of solar irradiance is due to the scattering of photons from the water droplets within clouds (Gueymard,

2017a). (Yordanov, Midtgård, et al., 2013) stated that the CE phenomenon is mainly due to strong forward Mie scattering inside the cloud and that the strongest overirradiance events occur when a narrow gap is surrounded by thin clouds within 5° around the solar disk. Simplistically, the photon flux hitting a cloud is redistributed so that enhanced irradiance areas are formed on the surface of the earth. (Gueymard, 2017a) studied the effect of cloud and albedo enhancement to global horizontal and global tilted irradiance, and examined typical explanations of CE phenomenon so that the overirradiance events were categorized in three groups: (i) the traditional case when irradiance is enhanced by clouds near the sun disk; (ii) under a homogenous cloud deck, it is possible that the diffuse horizontal irradiance (DHI) can be large before and after the overirradiance event so that the cloud edges do not contribute much to the irradiance enhancement; and (iii) the sun is partially obscured by a thin cloud layer so that the DHI can get very high values while the direct irradiance has relatively low values. Especially in cases (ii) and (iii), high ground albedo (due to snow cover, for example) can further enhance the irradiance.

Simulations have been used to study how different parameters affect the characteristics of overirradiance events. For example, (Yordanov, 2015) studied the radiative transfer of photons through a gap in a cloud by utilizing NASA's I3RC 3D Monte Carlo model. Their simulation model showed that, in case of overhead sun, irradiance could be 1.8 times the clear-sky irradiance, which is in line with the papers reporting extreme irradiance values from 1800 to 2000 W/m². (Pecenak et al., 2016) studied the effect of cloud optical depth and solar zenith angle to the irradiance enhancement by utilizing the 2D Monte Carlo radiative transfer model. Their simulation model showed that irradiance could be enhanced by 1.47 times the clear-sky irradiance in case of one cloud and 1.63 times in case of two clouds, and that the irradiance enhancement increases with an increasing solar zenith angle.

When considering the effect of CE phenomenon on PV power systems, the spatial extent of the events needs to be taken into consideration. This has been studied in (Järvelä et al., 2018) where it was shown that the diameter of overirradiance areas in Nordic latitudes can be up to several kilometers decreasing with increasing irradiance. (Lappalainen & Kleissl, 2020) used similar methods in California and they reached the same conclusions. The duration of overirradiance events ranges from some seconds up to some minutes (Järvelä et al., 2020), but when the cloud shadow speed is low, the durations of the longest overirradiance events have been measured to be several minutes (Yordanov, Midtgård, et al., 2013). Similar findings on the spatial extent have been exemplified in some papers that have discussed the effects of CE phenomenon on the operational characteristics of PV power plants. For

example, (Giesler et al., 2011) provided operational data and discussed the operation of 1, 1.5 and 2 MW utility scale PV power systems during overpower events. They noted that the MPP power of a 2 MW PV generator can exceed its nominal value so that the inverter is operating in power limiting mode when the DC-to-AC power ratio is close to 1. They also provided examples of the increase of DC side operating voltage during the overpower events but did not perform more in-depth analysis on it. (Weigl et al., 2012) studied the spatial extent of overirradiance events by developing cloud velocity vector method to estimate the irradiance profile on large land areas with side lengths of some hundreds of meters. They used the irradiance profile estimate to simulate the operation of central and string inverters and proved that overirradiance events can affect the operation of large PV generators, but they did not provide detailed analysis on the characteristics of overirradiance or overpower events. The occurrence, duration, and energy content of the overirradiance events have been studied in (Zehner et al., 2011), but they used low-resolution data and compared the irradiance to expected clear-sky irradiance instead of some static value based on, e.g., inverter power.

The effect of CE phenomenon to solar inverters have been covered – for example, in (Luoma et al., 2012) – where the effect of inverter sizing to system losses was studied from the CE phenomenon point of view. They used a simulation model where the output power of a PV generator was estimated by time averaging the irradiance data based on average movement speed of the clouds. However, clouds do not move at a constant speed (Lappalainen & Valkealahti, 2016b) and using time-averaged data does not provide exhaustive results. (Tapakis & Charalambides, 2014) discussed the overirradiance events and their effect on PV power systems. They speculated that the overirradiance events may negatively affect the operation of solar inverters, especially if the DC side current or voltage increases considerably. (Chen et al., 2013) analyzed inverter sizing with an assumption that they can handle brief overloading due to overirradiance events. They performed cost saving analysis with different power-limiting delays and concluded that it may be beneficial to design the inverter in a such way that it can handle brief overloading. (Macêdo & Zilles, 2007) covered the effect of power limiting with different DC-to-AC power ratios. They exemplified the effect of power limiting to the operating voltage but did not perform thorough analysis on it and the focus was set mainly to power loss analysis. Also, (Toreti Scarabelot et al., 2021) analyzed how different DC-to-AC power ratios affect the occurrence of overpower events and the operational characteristics of solar inverters. They concluded that operating temperatures of inverters can increase during overpower events, but they did not provide detailed statistical analysis on

actual operating conditions during the overpower events. (Lappalainen & Kleissl, 2020) analyzed the characteristics of overirradiance events in San Diego, California. The analyzes were based on irradiance and cloud shadow speed data that was used to deduce the irradiance profile over different land areas. They used the irradiance profile estimates to simulate the operation of PV power systems and provided analyses on the DC side operating voltages during the overpower events. However, they assumed static operating temperature for the PV panels, which neglects the cooling during the shade periods preceding the overirradiance events.

Even though the CE phenomenon is well known, the characteristics of overirradiance events are not fully understood. Many papers have concentrated on reporting maximum irradiance values, and the event duration analysis is often missing, insufficient or not suitable to analyze the operation of PV power systems. Some papers have discussed and provided examples on the spatial extent of overirradiance events, but in general, thorough statistical analyses have not been published. In brief, it is known that the overirradiance events can affect the operation of large utility-scale PV power plants, but the occurrence, duration and intensity of these events is not known. Similarly, comprehensive statistical analyses on the effects of the CE phenomenon on the operational characteristics of PV power systems have not been done. These have been discussed briefly in some papers, but the statistical analyses have been insufficient or sometimes they are based on wrong assumptions, e.g., constant cloud shadow speed or constant PV panel operating temperature. In fact, the focus is often set on loss-analysis, which is not that relevant from a practical point of view. It would be more beneficial to analyze how overirradiance and overpower events changes the operating point of the PV generator so that the effect on different system components could be estimated.

The goal of the present dissertation is to address the shortcomings of previous publications. As explained above, there is a clear research gap in the understanding on the characteristics of overirradiance and overpower events, and how these events affect the operation of PV power systems. Therefore, the objectives of this dissertation are as follows:

- The spatial extent of overirradiance events is analyzed in a statistical and systematic manner. This is because existing literature has examples of different overirradiance area sizes, but thorough analyses have not been published.
- The effect of PV generator size on the characteristics of overirradiance events is studied in more detail. Existing literature has examples of overirradiance

events affecting the operation of different PV generator sizes, but thorough analyses on how the PV generator size affects the occurrence, duration and irradiance of the events have not been done.

- The characteristics of overpower events are analyzed in more detail. This is done by utilizing irradiance and temperature measurement data to simulate the operation of a large residential size PV power plant. The operating conditions during the overpower events are also analyzed to recognize typical conditions during the strongest overpower events.
- The effect of overpower events on the operation of PV power plants is studied in more detail. The focus of existing literature is typically on loss-analysis and the effect of overpower events on system components is often missing or speculative. Instead of loss analysis, this dissertation focuses on how power-limiting during overpower events affects the loading profile and operation of system components.

The main scientific contributions of this dissertation can be summarized as follows:

- The relation between the irradiance and the diameter of overirradiance areas was determined. It was shown that the typical diameter of overirradiance areas is several tens of meters slightly decreasing with increasing irradiance. The mean diameter is some hundreds of meters, and the maximum diameter can be several kilometers. The focus areas of the strongest overirradiance events are of the order of some tens of meters.
- The relationship between the size of the PV generator and the occurrence, duration, and irradiance of overirradiance events affecting it was determined. It was shown that the occurrence of the overirradiance events is decreasing with increasing PV generator size, but the maximum duration of the events does not depend on the PV generator size. In fact, the mean and median durations of overirradiance events increase with increasing PV generator size.
- The operating conditions during overpower events were studied in detail, and it was shown that the cooling of PV panels during shade periods preceding the overirradiance events further increased the power of the PV generator by increasing the voltage of the panels. In fact, together with relatively cool ambient temperature, the cooling of the PV panels was found to be a prerequisite for the strongest overpower events.

- It was shown that the operating voltage of PV power systems can be close to or even exceed the nominal open circuit voltage of the PV generator during overpower events. This is due to the combined effect of power limiting, enhanced irradiance, and cooling of the panels during a shade period before the overirradiance event.
- It was shown that the effect of the CE phenomenon on the loading of PV system component is almost negligible and increasing the DC-to-AC power ratio further mitigates the effect. This is because with increasing DC-to-AC power ratio, the system will in any case operate against its power limit for long periods of time and system components are designed accordingly. The extra loading from the extreme overpower events becomes negligible because their duration is reasonably short, and the average operating voltage is only slightly higher than during normal operation.

The author wrote this dissertation and performed all the simulations and analyses. PhD Lappalainen provided the cloud shadow speed data that the author used to create an estimate of the overirradiance area speeds. Professor Valkealahti provided valuable comments on the content and helped define relevant research questions. The analysis of the characteristics of overirradiance events has been already published in (Järvelä et al., 2020, 2018), and the analysis of overpower events has been published in (Järvelä & Valkealahti, 2020, 2019). The data sets used in this dissertation are larger than the ones used in above mentioned publications, and the discussion on the effects on PV power systems and system components has been extended.

This dissertation is structured as follows.

- Chapter 1 provides a brief introduction to the topic and to the goals of the dissertation; and introduces and discusses the shortcomings of some of the previous papers published on CE phenomenon and its effects on PV power systems.
- Chapter 2 presents the theoretical background to dissertation. The first section discusses the operating principle of PV cells and derives the equations that are used to model the operation of PV cells in this dissertation. The second section discusses the construction of PV generators and PV power systems, and how they are operated and controlled in energy production applications. The last section presents the properties and definitions related to solar irradiance.

- Chapter 3 presents the measurement setup and research data upon which the results of this dissertation are based.
- Chapter 4 presents the methods, models, and parameters that were used in simulations. The first section describes how the characteristics of overirradiance events were derived from the irradiance data, the second section presents the simulation model that was used to analyze the characteristics of overpower events, and the last section presents how overirradiance and overpower events were defined and counted when analyzing the results.
- Chapter 5 presents the results on the characteristics of overirradiance events. The first section discusses the diameter of the overirradiance areas, the second section discusses how the PV generator size affects the occurrence, duration, and irradiance of the overirradiance events it experiences, and the last section discusses possible effects on the operation of PV generators.
- Chapter 6 discusses the characteristics of overpower events. The first section discusses the MPP power, duration, and occurrence of the overpower events, the second section discusses how these overpower events affect the operating voltage of the PV power plant, and the last section discusses the possible effects of the overpower events on power components of the inverter.
- Chapter 7 summarizes the key findings of this dissertation and proposes some future research topics related to the CE phenomenon.

2 THEORETICAL BACKGROUND

This chapter provides the theoretical background to the dissertation. The first section presents the operating principle and modelling of PV cells. The second section discusses how PV power plants are constructed and controlled, and how they operate under varying operating conditions. The last section discusses solar irradiance in more detail.

2.1 Operation of PV cells

PV cells utilize photovoltaic effect to convert solar irradiance into electrical energy. In brief, PV cells are manufactured by joining two different types of semiconductor materials together so that a p-n junction is formed at the boundary layer. When the PV cell is exposed to solar irradiation, the semiconductor material absorbs photons so that electron-hole pairs are formed. Then, the electric field in the p-n junction separates the electron-hole pairs, and charge carriers are transported to the opposite surfaces of the PV cell. Finally, the PV cell is connected to an external load (Gray, 2011).

2.1.1 Operating principle

Conventional PV cells are manufactured from semiconductors, such as crystalline silicon (c-Si). When considering the energy band structure of pure semiconductors, in low temperature the valence band is full, and the conduction band is empty of electrons so that there are no free charge carriers. When the temperature is increased, electrons can be thermally excited from the valence band to the conduction band so that electron-hole pairs are formed. In other words, pure semiconductors possess some characteristics of insulators and conductors.

The electron-hole balance can be controlled by doping the semiconductor with impurities; that is, atoms from other groups are introduced into the crystal structure. In the case of silicon, which belongs to group IV atoms, n-type semiconductors are

doped with group V atoms, such as phosphorus, so that there is an excess of electrons, and p-type semiconductors are doped with group III atoms, such as boron, so that there is a lack of electrons (excess of holes). When p-type and n-type materials are joined, the boundary layer forms a p-n junction. In that junction, the holes from the p-type layer diffuse to the n-type layer, and the electrons from the n-type layer diffuse to the p-type layer. Due to the diffusion of electrons and holes, impurities (donors in n-type and acceptors in p-type layers) are no longer screened by charge carriers; consequently, an electric field is formed, which limits the further diffusion of electrons and holes. Because the transition region between p- and n-type layers is now void of holes and electrons, it is called depletion region, and the regions on both sides of depletion region are called quasi-neutral regions.

When a PV cell is exposed to solar irradiation, photons may be absorbed in the semiconductor material. An electron–hole pair can be formed if the energy of an absorbed photon is larger than the band-gap energy E_g , which is the energy that is required to excite electrons from valence band to conduction band. In practice, the full spectrum and energy of solar irradiation cannot be utilized. Some photons are reflected from the surface of the PV cell, and some will pass through without being absorbed. The energy E of a photon depends on its wavelength λ so that $E = hc/\lambda$, where h is Planck constant, and c is the speed of light in the vacuum. In case the energy of an absorbed photon is larger than the band gap energy, the excess energy is turned into heat, and if the energy is not sufficient to create an electron–hole pair, it is turned only into heat. Because one photon can create only one electron–hole pair, the efficiencies of single junction c-Si PV cells are relatively low (Green et al., 2022).

The operational characteristics of a PV cell depend primarily on the intensity of irradiance, and temperature of the semiconductor material. In absolute darkness, a PV cell is effectively a large diode. When it is exposed to light, a photocurrent is generated due to the formation of electron–hole pairs. The photocurrent is proportional to the number of photons; that is, the increase in irradiance (more photons) translates to higher photocurrent (more electron–hole pairs). The electric field in the p-n junction separates the electron–hole pairs and moves charge carriers to opposite sides of the PV cell. When the PV cell is short-circuited by connecting p-type layer to n-type layer through an external circuit, the photocurrent is the reverse bias current of the diode. In there, the built-in potential creates the force that moves the charge-carriers. When a voltage over the PV cell terminals is increased, it compensates the reverse bias current until it reaches the open circuit voltage.

Figure 1 exemplifies the effect of irradiance to the current–voltage ($I-U$) characteristics of a typical single-junction c-Si PV cell when the operating temperatures are the same. The short circuit current is directly proportional to the irradiance, and open circuit voltage increases slightly with increasing irradiance.

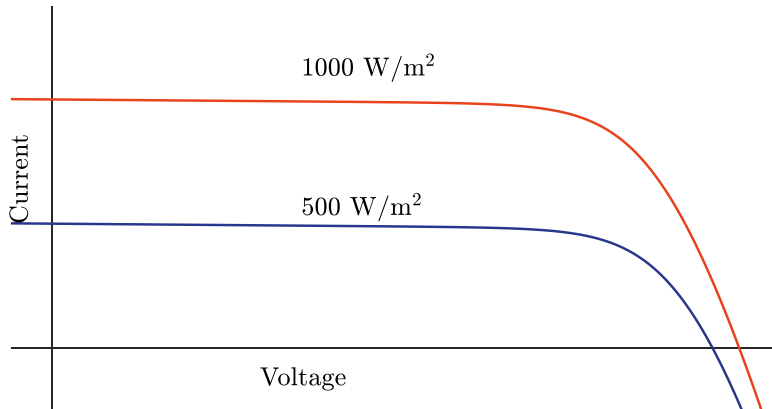


Figure 1. Effect of PV cell operating temperature on its $I-U$ characteristics.

Figure 2 presents the effect of semiconductor material temperature to the $I-U$ characteristics of a single-junction c-Si PV cell. Increasing the operating temperature decreases the open circuit voltage and slightly increases the short circuit current. The

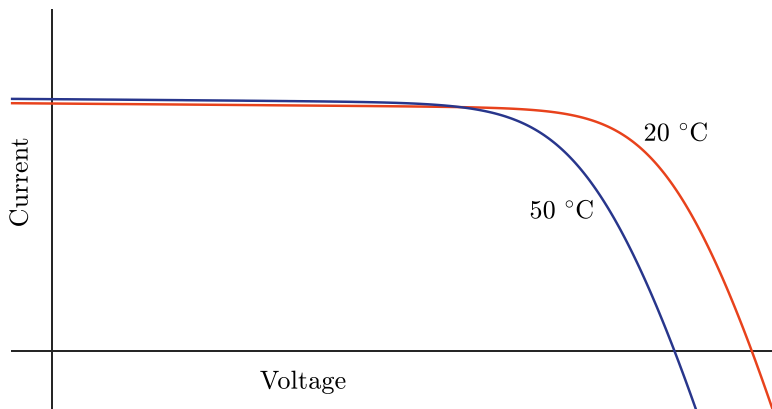


Figure 2. Effect of PV cell operating temperature on its $I-U$ characteristics.

decrease of operating voltage and the increase of short circuit current are due to decrease in band gap energy with increasing temperature, which decreases the open circuit voltage and allows photons with slightly less energy to create electron–hole pairs.

2.1.2 Modelling of PV cells

The current–voltage characteristics of a diode can be expressed by using the Shockley diode equation

$$I = I_S \left(e^{\frac{U}{AU_T}} - 1 \right), \quad (1)$$

where I_S is reverse bias saturation current, A is diode ideality factor, and U_T is thermal voltage. Thermal voltage is defined as

$$U_T = \frac{k_B T}{q}, \quad (2)$$

where k_B is Boltzmann constant, T is temperature and q is elementary charge (Shockley, 1949). Similarly, the current–voltage characteristics of an ideal PV cell can be expressed as

$$I = I_{SC} - I_{o1} \left(e^{\frac{U}{U_T}} - 1 \right) - I_{o2} \left(e^{\frac{U}{2U_T}} - 1 \right), \quad (3)$$

where I_{SC} is short circuit current, I_{o1} dark saturation currents due to recombination in the quasi-neutral region, and I_{o2} dark saturation currents due to recombination in the depletion region. When parasitic resistances are considered, the equation can be written as

$$I = I_{ph} - I_{o1} \left(e^{\frac{U+R_S I}{U_T}} - 1 \right) - I_{o2} \left(e^{\frac{U+R_S I}{2U_T}} - 1 \right) - \frac{U + IR_S}{R_{SH}}, \quad (4)$$

where I_{ph} is photocurrent, R_S series resistance, and R_{SH} shunt resistance. This two-diode model is often simplified by combining the effect of dark saturation currents so that the equation can be expressed as

$$I = I_{ph} - I_o \left(e^{\frac{U+IR_S}{AU_T}} - 1 \right) - \frac{U + IR_S}{R_{SH}} = I_{ph} - I_D - I_{SH}, \quad (5)$$

where I_o is dark saturation current, I_D is current through diode, and I_{SH} is current through shunt resistance. Figure 3 presents the equivalent circuits that have been derived from Equations 4 and 5.

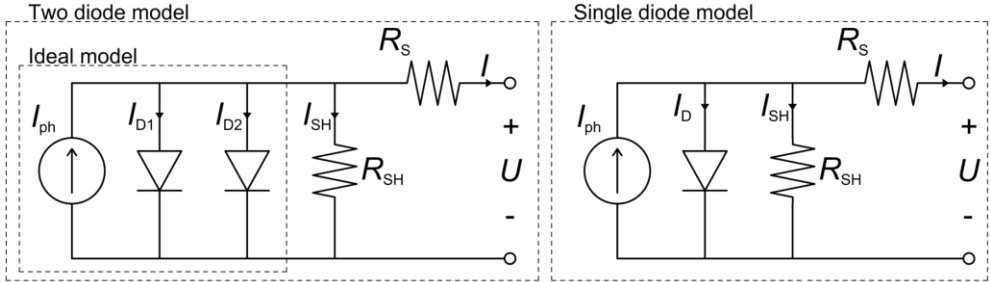


Figure 3. Two and single diode model of a PV cell.

The short circuit current I_{SC} can be written as a function of irradiance G , and semiconductor material temperature T so that

$$I_{SC} = \left(I_{SC,STC} + K_I(T - T_{STC}) \right) \frac{G}{G_{STC}}, \quad (6)$$

where $I_{SC,STC}$ is short circuit current in standard test conditions (STC), K_I is temperature coefficient for short circuit current, T_{STC} is STC temperature of 25 °C, and G_{STC} is STC irradiance of 1000 W/m² (Sera et al., 2007). Then, by assuming the diode current to be negligible, the photocurrent can then be written as

$$I_{ph} = I_{SC} \frac{R_{SH} + R_S}{R_{SH}}. \quad (7)$$

The dark saturation current can be written as a function of photocurrent, and semiconductor material temperature so that

$$I_o = \frac{I_{ph} - \frac{U_{OC,STC} + K_U(T - T_{STC})}{R_{SH}}}{\exp\left(\frac{U_{OC,STC} + K_U(T - T_{STC})}{AU_T}\right) - 1}, \quad (8)$$

where $U_{OC, STC}$ is open circuit voltage in STC, and K_U is temperature coefficient for open circuit voltage (Villalva et al., 2009).

2.2 Construction and control of PV power systems

PV power systems are very scalable. Their power can vary from some watts up to several gigawatts, and they can therefore be utilized in many applications. A simple low-power PV power system can comprise of a small PV cell and accompanying control electronics, whereas large utility scale power plants can consist of several multi-megawatt PV generator blocks that are connected to a high-voltage (HV) transmission grid through one or more interconnection points. To provide a sufficient background for how CE phenomenon affects the operation of PV power systems, this section presents how PV generators and PV power plants are typically constructed and controlled, and how varying operating conditions affect their operational characteristics.

2.2.1 PV generators

A PV cell can be considered as a basic building block of any conventional PV generator. The cells used in commercially available PV panels typically have square or near square shapes and they are approximately the size of a palm. Currently, most (95 percent) of the commercially sold PV panels are based on either monocrystalline or polycrystalline silicon cell technologies, and the market share of other technologies, such as thin-film, has been in steady decline (Jäger-Waldau, 2019).

Figure 4 illustrates poly- and monocrystalline PV cells. The crystal structure of monocrystalline PV cells is uniform, whereas polycrystalline PV cells are fragmented so that different sections have different crystal orientations. The differences in crystal structure can be observed visually; that is, polycrystalline PV cells are typically of different shades of blue, whereas monocrystalline PV cells are often monotonous dark blue. The silicon wafers used to manufacture monocrystalline PV cells are sliced from pure silicon ingots, while the polycrystalline PV cells are manufactured from multiple silicon fragments that are melted together and then sliced into wafers. The two whiteish and thick vertical lines are called busbars, and the thin horizontal lines are fingers. The fingers are for current collection and the busbars are used to connect

the PV cells together. The rounded corners on some of the monocrystalline PV cells are due to silicon ingots having cylindrical shape. By having slightly rounded edges, the silicon ingots can be utilized more efficiently; in that waste is reduced.

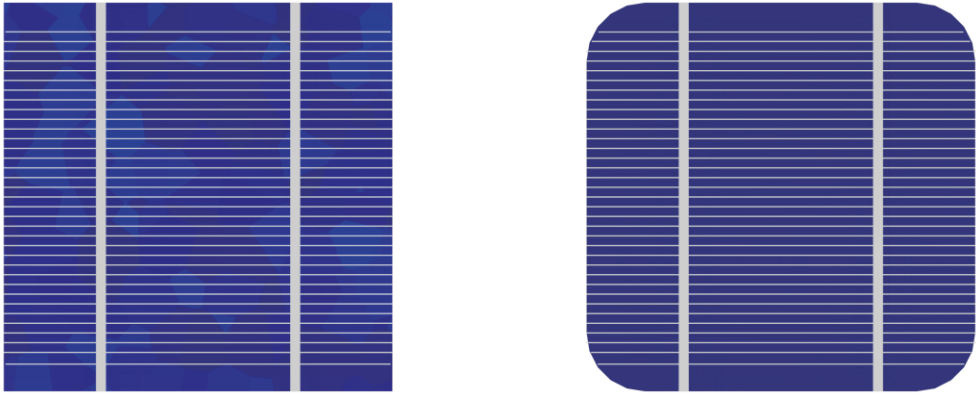


Figure 4. Illustration of polycrystalline (left) and monocrystalline (right) PV cells.

The voltage of a single c-Si PV cell is low, and there is a practical upper limit for its size (current); therefore, its power is too low for most of the applications. To increase power and voltage, PV cells are connected in series to construct PV panels. Most PV panels are constructed so that the PV cells are laid out in such a way that they form loops, as presented in Figure 5. To protect the PV cells against hot-spot heating, there is often a bypass diode in parallel with one loop.

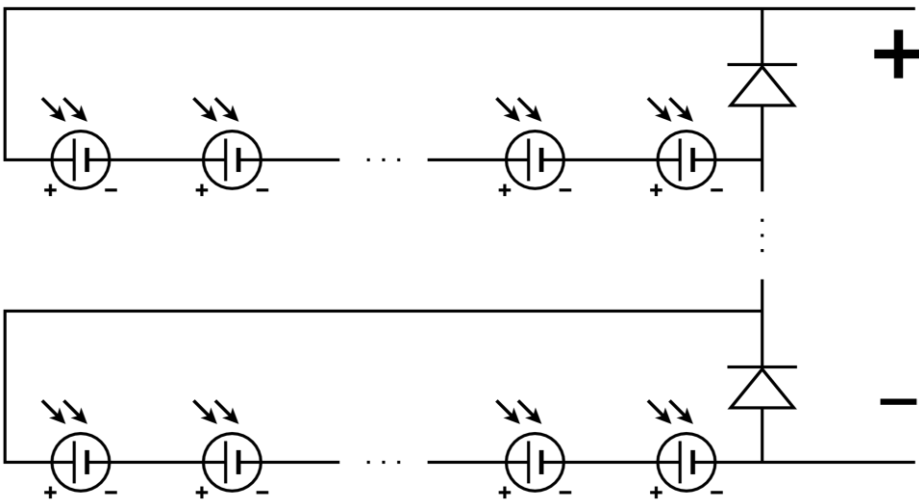


Figure 5. Electrical connections of a PV panel.

Figure 6 illustrates a typical PV panel construction. The PV panel consists of frame, front surface, encapsulant, PV cells, busbars, current collectors (fingers), bottom connections, and back plate. Glass is typically used as a front surface material, but polymer films can also be utilized. The function of the front surface is to let through light, and to protect the PV cells from the environmental loading, such as water ingress and physical impacts. A typical encapsulant material is ethylene vinyl acetate (EVA). PV cells are placed between EVA films, which function as an adhesive that bonds the PV cells to the front and back surface of the PV panel. The back plate is typically made from polyvinyl fluoride (Tedlar), and it supports the panel and provides protection from, for example, water ingress.

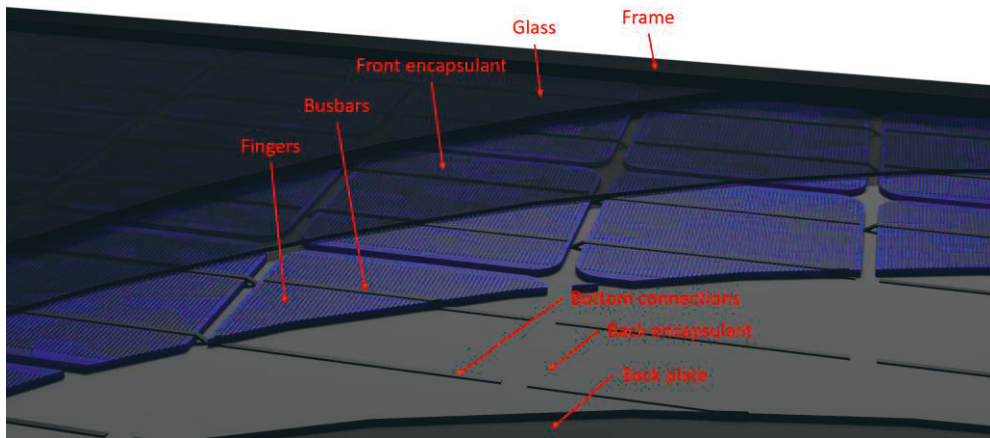


Figure 6. Construction of a PV panel.

Lately, there have been new commercialized PV panel technologies, e.g., bifacial panels and panels with half-cut cells. In bifacial panels, the back plate is also transparent, which increases the energy yield because now both sides of the PV cells are exposed to irradiance. The irradiance gain depends on, e.g., ground reflectivity, PV panel elevation and tilt angle (Guerrero-Lemus et al., 2016). PV panels that utilize half-cut cell technology have the PV cells cut in half, which are then connected in two loops that are then connected in parallel. This will slightly increase the panel efficiency because the current per loop is now smaller. Another benefit of half-cut cells is better shade tolerance, which can considerably increase the energy yield in built environment (Calcabrini et al., 2021). By cutting the cells in quarter-size can further increase the efficiency (Tang et al., 2017).

Commercially sold PV panels typically have power in the order of some hundreds of watts, voltage of tens of volts, and current of approximately ten amperes. To

increase the power, PV panels are connected in series and in parallel to construct PV generators. Figure 7 presents PV generator topologies with typical power ratings up to (a) 10 kW, (b) some hundreds of kilowatts, and (c) a few megawatts. Subfigure (a) presents a PV generator consisting of a single PV string, which is constructed by connecting PV panels in series. In practice, there is an upper limit for the voltage, so the number of panels that can be connected in series is limited. Typically, the open circuit voltage can be up to 1500 V; that is, the power of one PV string can be up to 10 kW. To further increase the power, PV strings can be used to construct PV arrays by connecting them in parallel, as presented in Subfigure (b). The PV strings can be connected directly to the inverter, or they can be connected in the array combiner boxes. The practical upper limit for parallel connected PV strings is typically some tens of strings, which means that the power of one PV array can be up to some hundreds of kilowatts. Subfigure (c) presents a typical configuration of multi-megawatt PV generator with several parallel connected PV arrays. The practical upper limit for parallel connected PV arrays depends on several factors, such as inverter rating, DC-to-AC power ratio, and DC side cabling costs. In general, the larger the land area of a PV generator, the longer the furthest array combiner boxes, and consequently, the longer (more expensive) the DC side cables.

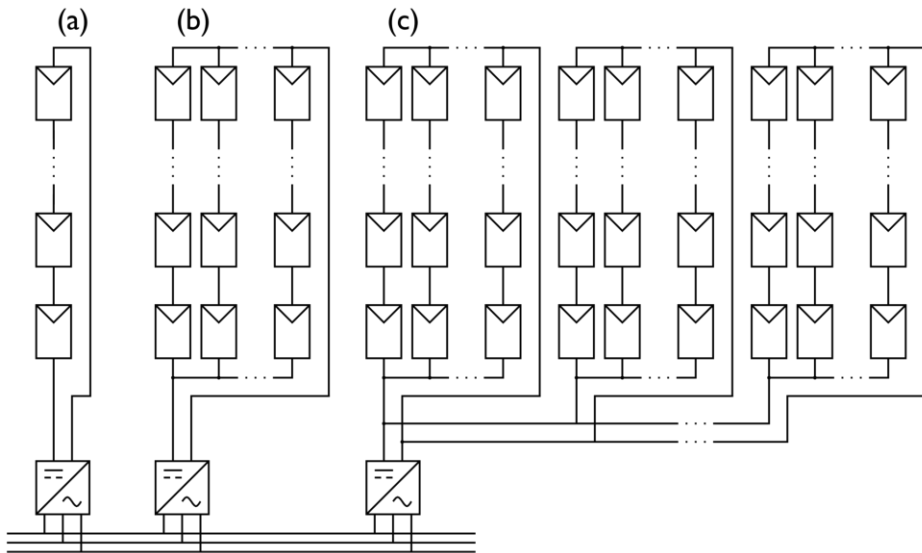


Figure 7. Typical PV generator topologies.

The construction and scale of utility scale PV power systems is further exemplified in Figure 8. Subfigure (a) presents the construction of a PV array, and

Subfigure (b) shows the construction of a PV generator on a PV power plant consisting of several multi-megawatt PV generator blocks. In utility-scale applications, PV panels are typically installed on ground mounted frames, and there are several frames side by side in several rows. The distance between panel rows depends on factors such as tilt angle, sun elevation, and cost of land. Determining optimal panel row distance is, in practice, an optimization problem between self-shading losses and cost of energy (Brelc & Topič, 2011). PV panels are connected in series to form PV strings by utilizing the junction boxes that are on the backside of the PV panel. PV strings are connected to array combiner boxes, which are equipped with, for example, connection terminals for string cables, string fuses, surge protection devices, a DC switch to disconnect the PV panels, and possibly some monitoring devices. PV arrays are connected to solar inverter by DC cables that are typically dug into ground. The inverter converts the DC current from the PV generator to an AC current that is then fed forward through a medium voltage (MV) transformer and a MV switchgear. The PV generator, inverter, transformer, and accompanying equipment form building blocks of large PV power plants. These blocks are then connected to a high-voltage (HV) substation for the final grid interconnection.

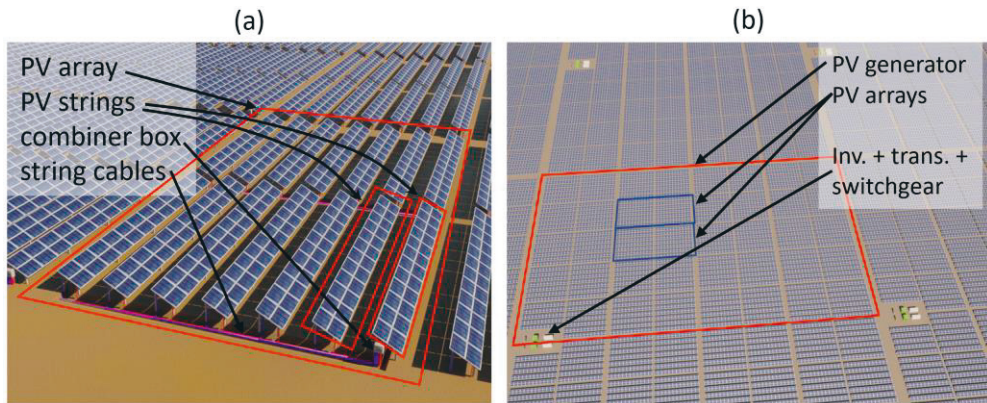


Figure 8. Construction of utility scale PV power systems.

When considering the design of PV generators from the CE phenomenon point of view, the interesting aspect is the land area (power) of the PV generator. Obviously, the larger the land area is, the larger the overirradiance area must be to fully cover the PV generator. The side length of a square-shaped PV generator can be several hundreds of meters. It should be noted that if the inverter has several maximum power point trackers or independent power sections, the PV generators

connected to each tracker are not interconnected, so the DC side should be considered to have several smaller PV generators that are operated independently.

2.2.2 Operation of PV generators

The current–voltage characteristics of a PV generator depend on PV panel type and configuration, and the irradiance and operating temperature of each of panels. If all the PV panels have similar operating conditions, and all the parallel connected PV strings are identical, the $I-U$ curve of a PV generator would be an upscaled version of the $I-U$ curve of a single PV panel. In practice, however, this is not the case. Even in clear-sky conditions when the irradiance can be considered uniform, the tilt-angles of PV panels may differ slightly, the panels degrade at different paces, and the operating temperature of the panels may differ due to the cooling effect of wind affecting different parts of the PV generator differently. This section presents how non-uniform operating conditions affect the $I-U$ characteristics of different PV generator configurations, and how varying operating conditions affect the operating temperature of the panels.

To understand how the $I-U$ curve of a PV generator is formed, Figure 9 presents a typical $I-U$ curve of a PV panel in three quadrants when the operating conditions of individual PV cells are uniform. A PV panel is typically operated in the first quadrant to generate power. If the current is higher than the short circuit current or the voltage is higher than the open circuit voltage, the operating point of the PV

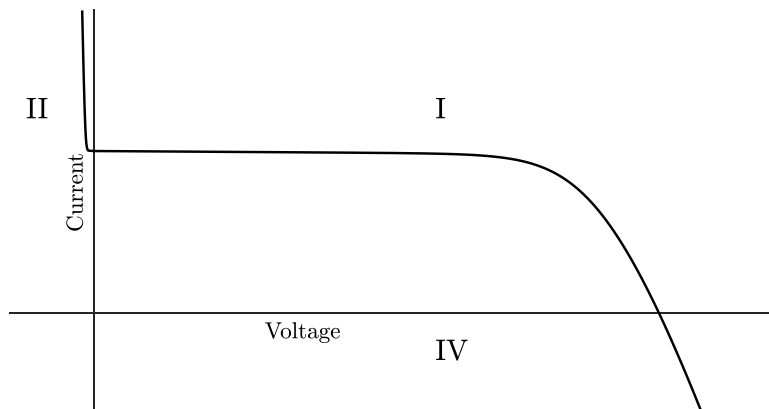


Figure 9. Current–voltage curve of a PV module in Quadrants I, II, and IV.

panel can also be in Quadrants II or IV. In Quadrant II, the PV panel is reverse-biased because the operating current is higher than the short circuit current so that most of the current flows through the bypass diodes. In this case, some power is dissipated in the bypass diodes. In fact, the $I-U$ curve shape in Quadrant II is the inverse of a typical diode $I-U$ curve. The operating point can be in Quadrant IV when the operating voltage is higher than the open circuit voltage. In this case, the current flow changes direction and the PV panel dissipates power as heat. Operating the PV panel in IV quadrant may be intentional to utilize the heating, such as in snow removal (Yan et al., 2020).

When PV panels are connected in series, the current through each PV panel is the same. When the non-uniformity of operating conditions is strong enough, bypass diodes change the shape of the $I-U$ curve in the first quadrant. This is exemplified in Figure 10, which presents the $I-U$ curve of two series connected PV panels when the panels are otherwise identical, but one is shaded and the other one is unshaded. When the operating current is lower than the short-circuit current of the shaded panel, the current flows through PV cells and the voltage is approximately double that of a single panel. When the operating current is higher than the short circuit current of the shaded panel, it begins to flow through the bypass diodes of the shaded panel, and the voltage is that of the unshaded panel minus the voltage loss on the bypass diodes in the shaded panel.

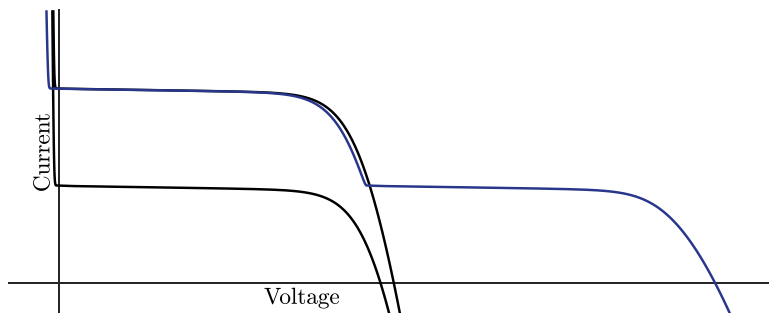


Figure 10. Current-voltage curves of shaded and non-shaded PV panels (black lines) and their series connection (blue line).

When PV panels are connected in parallel, the voltage of the panels is the same. This is exemplified in Figure 11, which presents the $I-U$ curve of two parallel connected panels when one is shaded and the other one is unshaded. Unlike the series connection, bypass diodes do not affect the shape of the $I-U$ curve in the

same way. If the parallel connected panels are not connected to an external load, in open circuit there might be current flowing from panel to panel if their operating conditions are non-uniform.

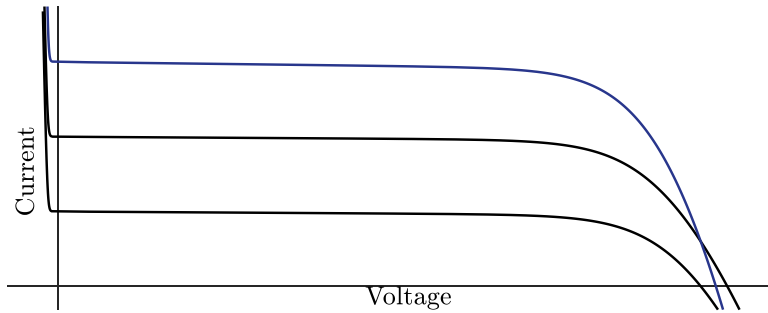


Figure 11. Current–voltage curves of shaded and nonshaded PV panels (black lines) and their parallel connection (blue line).

Figures 12 and 13 present the power–voltage ($P-U$) curves of the above presented cases of series and parallel connection. The $P-U$ curve of series connected PV panels have two distinct MPPs. The highest peak is the global MPP and the other one is a local MPP. With parallel connected panels, there is only one MPP. The number of MPPs depends on the number of irradiance levels and the number of PV panels (bypass diodes). In practice, the longer the PV strings are, the higher the number of MPPs can be, and having more PV strings in parallel reduces the number of MPPs (Lappalainen & Valkealahti, 2020).

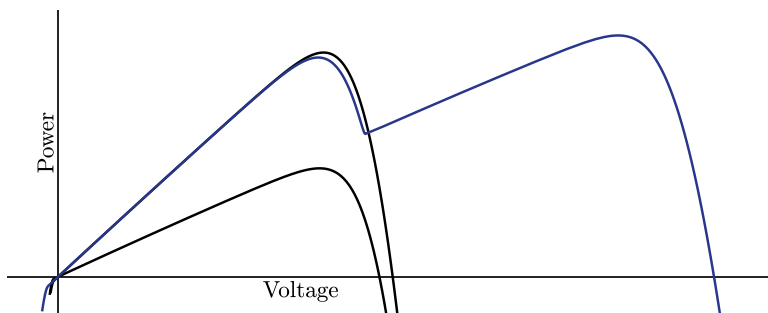


Figure 12. Power–voltage curves of shaded and nonshaded PV panels (black lines) and their series connection (blue line).

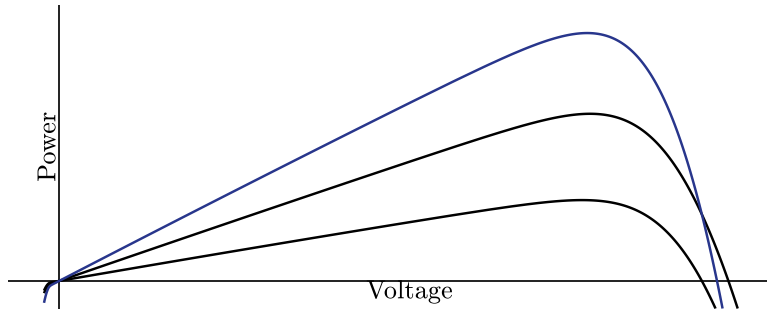


Figure 13. Power–voltage curves of shaded and nonshaded PV panels (black lines) and their parallel connection (blue line).

When considering the effect of CE phenomenon to the $I-U$ characteristics of a PV generator, interesting aspects are, obviously, irradiance and its profile over the PV panels, but also the operating temperature of the PV panels, which affects mainly the open circuit voltage. With c-Si panels, the effect of operating temperature on MPP power is approximately $0.5 \text{ \%}/^{\circ}\text{C}$, which is significant because the operating temperature can vary several tens degrees of Celsius, even when the ambient temperature is unchanged. In addition to ambient temperature, the operating temperature is affected by wind speed and direction, irradiance, mounting of PV panels, and several other factors. Various models have been developed to estimate the PV panel operating temperature (Skoplaki & Palyvos, 2009). Under high irradiance conditions, the operating temperature can be considerably higher than the ambient temperature, especially if the installation arrangement does not provide proper cooling by, for example, wind.

In steady-state conditions, the PV cell temperature is almost linearly dependent on the irradiance (Koehl et al., 2011), but on partly cloudy days the operating conditions can change quickly and the PV cell temperature can drop during shade periods preceding the overirradiance events. Due to the thermal mass of the PV panel, changes in operating conditions are not immediately seen in the PV cell temperature. On partly cloudy days, the irradiance has fast fluctuations, and due to the CE phenomenon, the irradiance affecting the PV generator can occasionally exceed the clear-sky irradiance. Therefore, when analyzing the effect of PV generators, changes in operating temperature should also be considered.

2.2.3 Solar inverters and control of PV power plants

When a PV generator is connected to the power grid, a solar inverter is needed to transform the DC current from the PV generator into AC current. Solar inverters can be categorized in many ways, such as into grid feeding (grid connected) or grid forming (stand-alone); according to number of power stages into single or multi (power) stage; according to power rating into module, string, or central; according to application into residential, commercial, and utility-scale; and according to power stage topology into two-level or multi-level (voltage) inverters (Dogga & Pathak, 2019).

Figure 14 presents the construction of a typical solar inverter that consists of a DC circuit, power stage, and AC circuit. A typical DC circuit consists of input terminals, input fuses, and disconnection devices; the power stage consists of a DC link capacitor, semiconductor switches, and filter circuit; and the AC circuit consists of AC fuses and output terminals. Auxiliary and control circuits consist of, for example, power supplies; control and communication units; current, voltage, temperature, and humidity sensors; and grid protection relays.

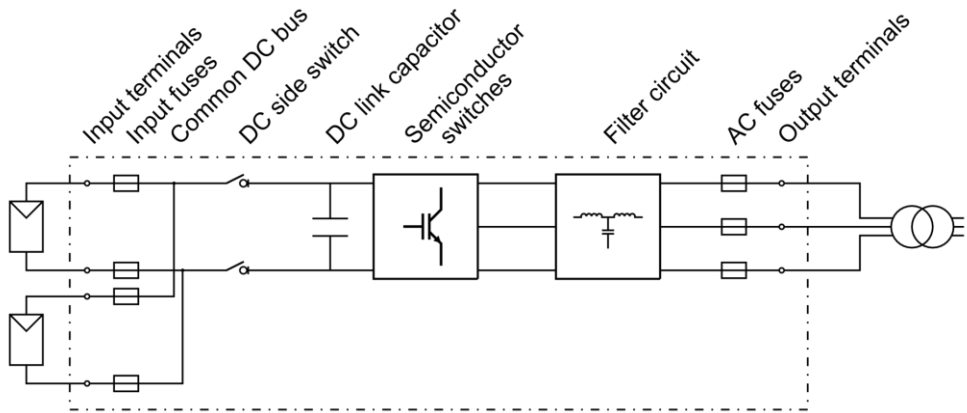


Figure 14. Typical construction of a solar inverter.

The state machine of a simple solar inverter consists of stand-by, maximum power point tracking (MPPT), and power-limiting modes. In stand-by mode, the power of the PV generator is zero; in MPPT mode, the inverter tries to operate the PV generator in its MPP; and in power-limiting mode, the power of the PV generator is limited.

Typically, the power of a PV generator is controlled by controlling its operating voltage (or current). In practice, the inverter is given a voltage (or current) reference

and the operating point of the PV generator is set accordingly. In stand-by mode, the inverter is either disconnected from the PV generator or the power reference is set to zero so that the voltage of the PV generator equals the open circuit voltage. In MPPT mode, the inverter attempts to operate the PV generator in its global MPP. Various MPPT algorithms have been developed or proposed in the literature (Motahhir et al., 2020), but in practice they are often based on perturb and observe (P&O) methods, where either the operating current or voltage is perturbed periodically, and the output power is observed. If the power is decreasing, the perturbation direction is changed. The strengths of P&O algorithms are that they are simple to implement, and they offer good performance. However, they may get stuck on local MPPs instead of finding the global MPP.

It is occasionally necessary to limit the power of the inverter. This could be to protect the inverter from overcurrent, or it may be due to grid-code related reasons, such as power ramp-rate limits. When considering the operating point of the PV generator, it must be within the safe operating area of the inverter, which is exemplified in Figure 15. For single-power-stage inverters without boost circuits, peak AC side grid voltage defines the minimum DC-side voltage. Maximum DC-side voltage is limited by rated voltage or operational characteristics of individual components, such as semiconductor switches, fuses, and switches. DC power limit depends on the AC power limit, which in practice, depends on AC side current limit. The safe operating area can be further limited by DC current limit due to some DC side components. In practice, these limits are not fixed but dynamic in nature. AC grid voltage can vary several percentages from the nominal voltage, which affects the minimum DC side voltage, and DC power limit. In general, current (power) limits

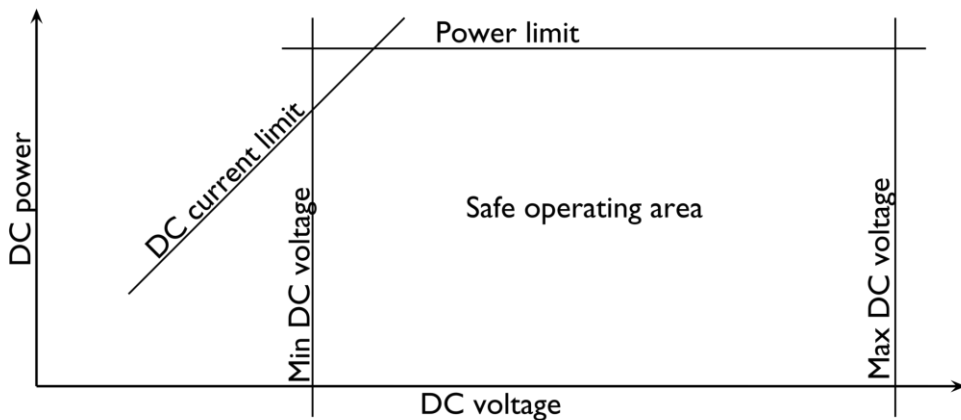


Figure 15. Safe operating area of inverter.

depend on temperature rise margin of different components, i.e., when ambient temperature is lower, the margin for temperature rise is larger, and vice versa. Therefore, many inverters have varying power limits depending on ambient temperature, power factor, operating voltage, installation altitude, etc.

When considering the effect of CE phenomenon on the operation of solar inverters, the power of the PV generator, as such, is not interesting because the inverter will enter power limiting mode. Therefore, any potential extra energy yield from increased irradiance will be lost due to power curtailment. However, power limiting will increase DC-side operating voltage, which may affect the power losses and lifetimes of certain power components. In general, conversion efficiencies of inverters without boost circuits decrease with increasing DC side operating voltage (ABB Oy, 2018; Sungrow, 2020). The decrease of efficiency increases the power losses, which increases the operating temperatures.

For example, the total losses of insulated-gate bipolar transistors (IGBTs) consist of switching and conduction losses of the transistor and the free-wheeling diode. The voltage, current and junction temperature dependency on the switching losses, E_{sw} , can be written as

$$E_{sw} = E_{sw0} \left(\frac{I}{I_0} \right)^{K_I} \left(\frac{U}{U_0} \right)^{K_U} \left(1 + K_T(T_j - T_{j0}) \right), \quad (9)$$

where E_{sw0} , I_0 , U_0 , and T_{j0} are switching losses, current, voltage, and junction temperature in reference point; and K_I , K_U , and K_T are dependency coefficients for current, voltage, and junction temperature, respectively. Semikron gives K_I a value of 1.0 and for K_U 1.2 – 1.4 (Nicolai, 2014). Therefore, if power is kept constant, increasing the voltage (decreasing current) will increase switching losses. The effect of DC voltage to the reliability of IGBTs has been studied in (Miao et al., 2018), where the switching and conduction losses of IGBTs and free-wheeling diodes were analyzed as functions of DC voltage and switching frequency. They concluded that increasing the DC voltage increases the losses and damage degree of IGBTs.

Another component that is directly affected by the DC side operating voltage is the DC link capacitor. There are many different capacitor technologies available, but often electrolytic or film capacitors are used in solar applications. Electrolytic capacitors have higher capacitance per unit volume whereas film capacitors have better voltage ratings. In general, the lifetime of a capacitor depends on its operating temperature and voltage. Operating temperature depends on ambient temperature and the temperature rise caused by ripple currents, and operating voltage depends

on the operating point of the PV generator. The ageing of capacitors is determined based on the change in capacitance and equivalent series resistance (ESR) values. In electrolytic capacitors, the increase of operating temperature causes degradation through the evaporation of electrolytes (Torki et al., 2023), and the increase of voltage increases the stress to the dielectric layer, which consumes ions in the electrolyte through self-healing (Hayek et al., 2019).

In general, the useful lifetime, L , of an electrolytic capacitor can be written as

$$L = L_0 K_T K_R K_U, \quad (10)$$

where L_0 is lifetime in nominal conditions, and K_T , K_R , and K_U are dependency coefficients for temperature, ripple current and operating voltage, respectively (Hayek et al., 2019). The dependency coefficient for temperature follows the Arrhenius law where 10 °C increase in ambient temperature, T , halves the lifetime, so that

$$K_T = 2^{\frac{T_0 - T}{10K}}, \quad (11)$$

where T_0 is nominal temperature. The dependency coefficient for ripple current can be written as

$$K_R = K_I \exp\left(\left(1 - \left(\frac{I_R}{I_{R0}}\right)^2\right) \frac{\Delta T_0}{10K}\right), \quad (12)$$

where K_I is empirical safety factor, I_R and I_{R0} are application and nominal rated ripple currents, and ΔT_0 is the temperature rise of the capacitor core in nominal conditions. The voltage dependency can be written as

$$K_V = \left(\frac{U}{U_0}\right)^{-n}, \quad (13)$$

where U is operating voltage, U_0 is nominal voltage, and n experimental exponent coefficient. For example, Jianghai capacitors recommends a moderate value of $n = 2.5$ for their electrolytic capacitors (Albertsen, 2010).

Similarly, the lifetime expectancy of film capacitors depends on capacitor core temperature and operating voltage. The lifetime expectancy curves are often

provided in the datasheets, as exemplified in Figure 16. It can be observed that the operating temperature and voltage has a huge effect on the lifetime. In this case, keeping the operating voltage at 1.0 p.u. (relative to nominal voltage) and reducing the capacitor core temperature from 85 °C to 70 °C increases the lifetime from 20,000 hours to 100,000 hours. Similarly, keeping the core temperature at 85 °C and increasing the operating voltage from 0.7 p.u. to 1.0 p.u. decreases the lifetime from 100,000 hours to 20,000 hours.

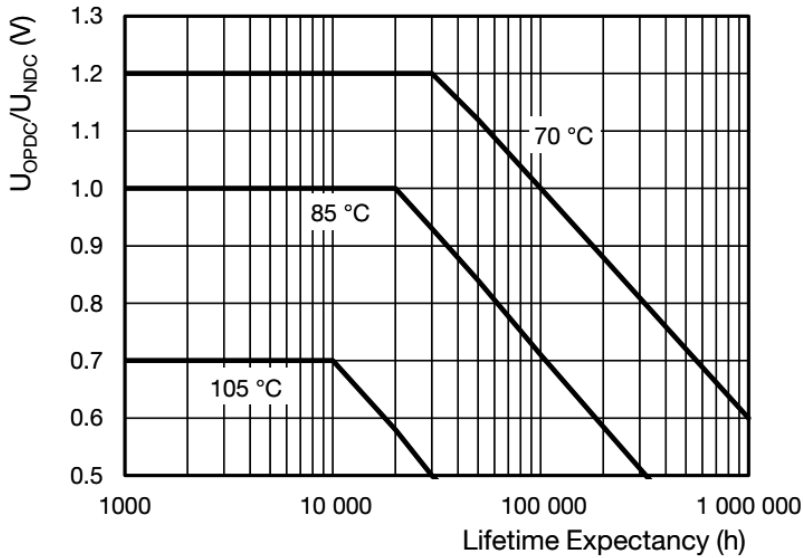


Figure 16. Lifetime expectancy curves of Vishay MKP1848C polypropylene film capacitors (Vishay, 2022).

In solar applications the operating conditions and loading points vary a lot. To determine the lifetime of the capacitor, the loading points of the inverter can be categorized into, e.g., nighttime stand-by, nighttime reactive power compensation, daytime full power (clear-sky days), and daytime partial power (overcast or partly cloudy days) and the stressing of the capacitor is calculated for each category and then summed together (Gallay, 2018). It can be seen from Figure 16 that harsh operating conditions with high operating temperature and high operating voltage are degrading the capacitor considerably faster than easier operating conditions.

2.3 Solar irradiance

The solar constant is the long-term mean value for the full spectrum intensity of solar irradiance on a perpendicular plane towards the sun above the upper atmosphere of earth. It has a recommended value of 1366 W/m^2 in ISO 14222 standard, but according to recent space radiometry results, a slightly lower value of 1361 W/m^2 has been proposed (Gueymard, 2018a). Regardless, the intensity of irradiance above atmosphere has some small variation due to changes in the activity level of the sun, some of which are cyclical in nature.

Above the atmosphere, the spectrum of solar irradiance resembles the spectrum of 5778 K blackbody object. Before reaching the surface of the Earth, irradiance must pass through the atmosphere, where it is attenuated by oxygen, ozone, water vapor, carbon dioxide, etc. so that different wavelengths are affected differently (Gueymard, 2018b). The attenuation of irradiance depends on altitude and sun elevation angle; that is, how long the optical path through the atmosphere is. Typically, optical path length is expressed with air mass (AM), which simplistically describes how many atmospheres the light must travel through. It has a value of 0.0 above the atmosphere, 1.0 at sea level with a sun elevation angle of 90° , and can be all the way up to 38 at sea level with a sun elevation angle of 0° (Kasten & Young, 1989).

The irradiance on a plane on the surface of the earth can be categorized into direct, diffuse, and reflected irradiances (Stoffel, 2013). Direct normal irradiance (DNI) is the direct irradiance from the sun on a perpendicular surface to the direct irradiance path, and the diffuse horizontal irradiance (DHI) is the indirect irradiance that is scattered from the clouds, air molecules and aerosols in the atmosphere. The DNI is measured with 2.5° half-angle around the solar disk; therefore, in practice, the direct irradiance contains some diffuse irradiance (Blanc et al., 2014). Reflected irradiances can be caused naturally by snow, water, ice, and ground albedo or by reflections from building facades in built environments. Global horizontal irradiance (GHI) is the total irradiance on a horizontal plane, and global tilted irradiance (GTI) is the total irradiance on a tilted plane; that is, the actual irradiance received by the tilted PV panel.

The nominal power of PV panels is defined under the STC irradiance of 1000 W/m^2 , PV panel temperature of 25°C , and airmass of 1.5. AM 1.5 is used because it presents typical operating conditions better than, for example, AM 1.0 (Riordan & Hulstron, 1990). During clear-sky conditions, GTI can exceed 1000 W/m^2 near the equator. On the other hand, in high latitudes where sun remains

relatively low, even during summer months, GTI can be under 1000 W/m^2 even during the peak production hours of the summer season.

3 RESEARCH DATA

This chapter presents the research data that were used in the analyses of this dissertation. The first section presents the measurement system and its components; second and third sections discuss the measurement data and data quality assurance; and the last section presents the cloud shadow speed data that were used to estimate the overirradiance area movement speeds.

3.1 Measurement system

The results and analyses presented in this dissertation are based on measurements from 23 summer months from 2014 to 2018 from the Tampere University (TAU) solar PV power station research plant (Torres Lobera et al., 2013). The TAU PV power research plant is located on the rooftop of the electrical engineering unit of the Hervanta campus of Tampere University. Tampere is an inland city in Finland that has a warm-summer humid continental climate and no major mountain ranges nearby.

The TAU PV power research plant consists of 69 PV panels and an extensive measurement system. The layout of panels and the locations of measurement devices are presented in Figure 17. The measurement system consists of Kipp & Zonen CMP22 irradiance sensor for global horizontal, and Kipp & Zonen CMP21 with a shadow ring for diffuse irradiance measurements. Wind speed and direction are measured with Vaisala WS425 S+D sensor, and ambient temperature and humidity with Vaisala HMP155 T+H sensors. In addition, 24 of the PV panels are equipped with S-P Lite 2 irradiance sensors (S1, S2, ...) and thermocouples (T1, T2, ...) for PV panel temperature measurements. PV panels are installed in rows that are distributed scarcely throughout the rooftop facing 23° east from due south. The distance between the southern and northernmost panel rows is 48 meters, and the width of the widest panel row is 45 meters. The maximum distance between the two furthestmost irradiance sensors (S16 and S4) is 56 meters. The land area of the area covered by irradiance sensors equals approximately 1300 m² and corresponds to the land area of a typical commercial 0.1 MW roof-top PV power plant.

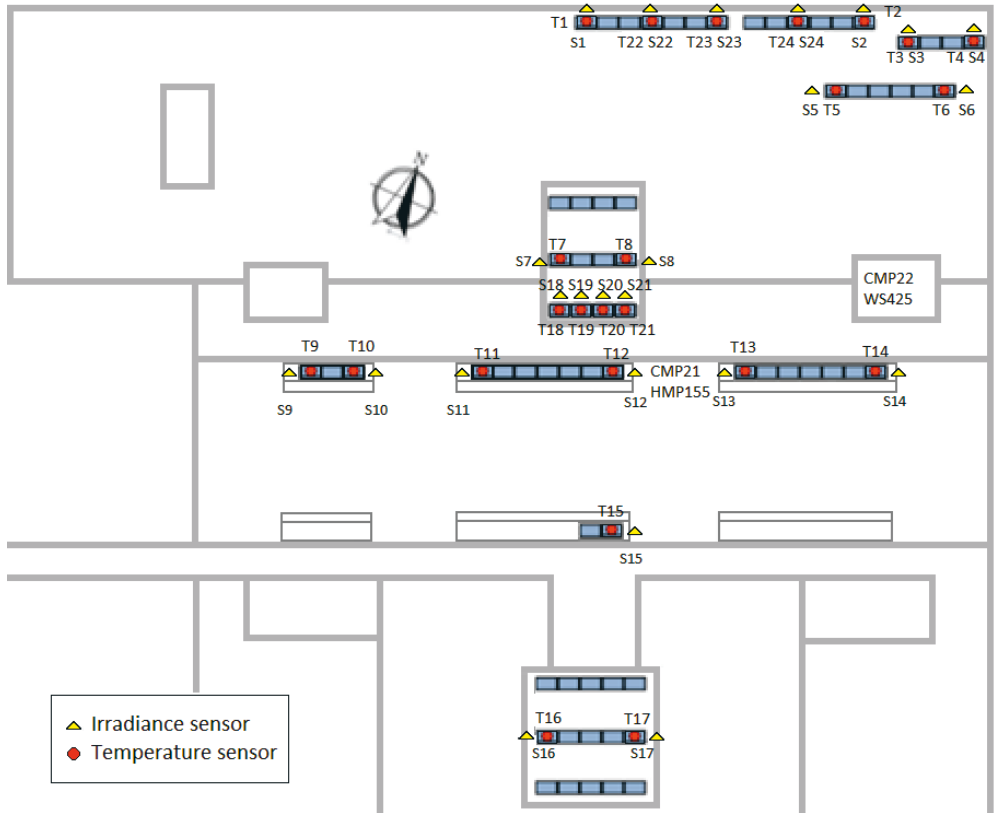


Figure 17. The layout of PV panels, and the locations of irradiance, and temperature sensors on the rooftop of Tampere University.

Figure 18 presents the installation arrangement of the PV panels and the location of one of the S-P Lite 2 irradiance sensors. PV panels are installed at a fixed 45° tilt angle, and irradiance sensors are mounted to the frames of the PV panels so that their orientation closely matches that of the corresponding PV panel. The irradiance sensors have fast response time (<500 ns to 90 percent) and wide measurement range (up to 2000 W/m^2). The temperature of the PV panel is measured with a thermocouple pressed against the backside of the PV panel. Due to the thermal mass of the PV panel, there can be a small difference between the measured PV panel temperature and the PV cell temperature, but for the analysis of overpower events, the measured PV panel temperature provides a good estimate of the actual PV cell operating temperature. The gap between the PV panel frame and the rooftop is small, which may slightly reduce the cooling of the panels on windy days. On the other hand, the panel rows are quite scarcely distributed, which means that during peak irradiance hours the front area of the panels are not shaded by shadows cast by

other panels. When compared to a tightly packed PV generator, this may increase the measured irradiance slightly due to reflections from the tar-and-gravel surface of the rooftop.



Figure 18. Mounting of the NAPS PV190Kg PV panel and the adjacent S-P Lite 2 irradiance sensor.

3.2 Measurement data

The research data that were used in this dissertation are comprised of irradiance data from 21 irradiance sensors (S1-S21), PV panel temperature data of one panel (T12), and ambient temperature data. All measurements were recorded with 10 Hz sampling frequency. The measurement data is exemplified in Figure 19. Subfigure (a) presents the irradiance profiles of a clear-sky day on 28th of May 2018 and a partly cloudy day seven days later, on the 4th of June 2018. Both irradiance measurements were made with a sensor S12 located in the middle of the research power plant. Solar noon during these days was 12:22 and 12:23, and the corresponding sun altitude was 50° and 51°, respectively. However, due to the orientation of the TAU PV power research plant, the irradiance sensor faces the sun at 11:18 and 11:19 at corresponding sun altitudes of 48° and 49°, respectively. The peak irradiance on the clear-sky day is approximately 900 W/m². The irradiance measurement data is presented together with ambient and PV panel temperature data on a clear-sky day in Subfigure 18 (b), and on a partly cloudy period in Subfigure 18 (c). The relation

between irradiance and PV panel temperature is clearly visible in Subfigure 18 (b), and the effect of the thermal mass of the PV panel in the rate of change of temperature is clearly visible in Subfigure (c). The difference between the ambient temperature and the PV panel temperature is higher on the clear-sky day than it is on the partly cloudy period even though the irradiance is occasionally higher in partly cloudy periods.

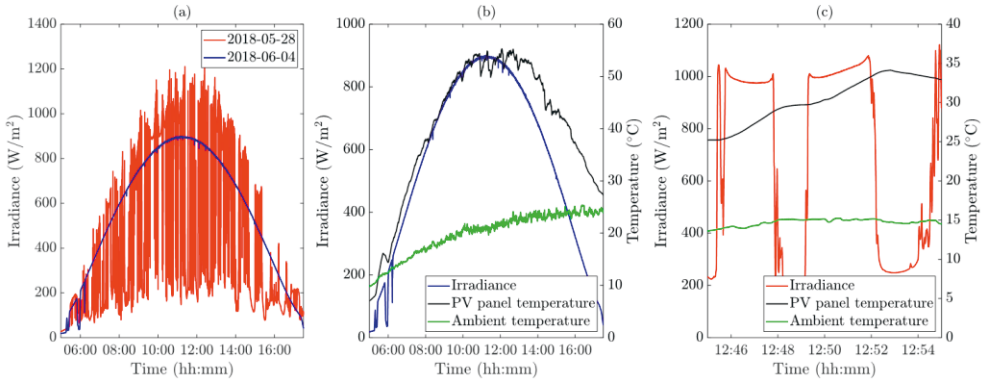


Figure 19. (a) Irradiance profiles of clear-sky and partly cloudy days, and the relation between irradiance, and ambient and PV panel temperatures (b) on a clear-sky day, and (c) on a partly cloudy period.

Because the irradiance sensors are installed in a tight mesh, it is possible to create detailed images of the irradiance profile and the movement of cloud shadows and overirradiance areas. This was done by utilizing the known coordinates of irradiance sensor and the linear interpolation method of Matlab's griddata function (Appendix B). This is exemplified in Figure 20, which presents six snapshots of the irradiance with two-second intervals of an overirradiance area covering the rooftop. The movement of the overirradiance area is clearly visible and the average irradiance on the rooftop increased from around 400 W/m² to 1200 W/m² in approximately ten seconds. It can be observed that the preceding cloud shadow had a clear and almost linear edge. Due to the tight arrangement of the irradiance sensors, especially in the middle part of the covered area, irradiance variations can be inspected accurately. This improves the accuracy and credibility of the results when simulating the operation of PV generator, for example, regarding the effect of mismatch losses that depends on the configuration of the PV generator and movement direction of the cloud shadow.

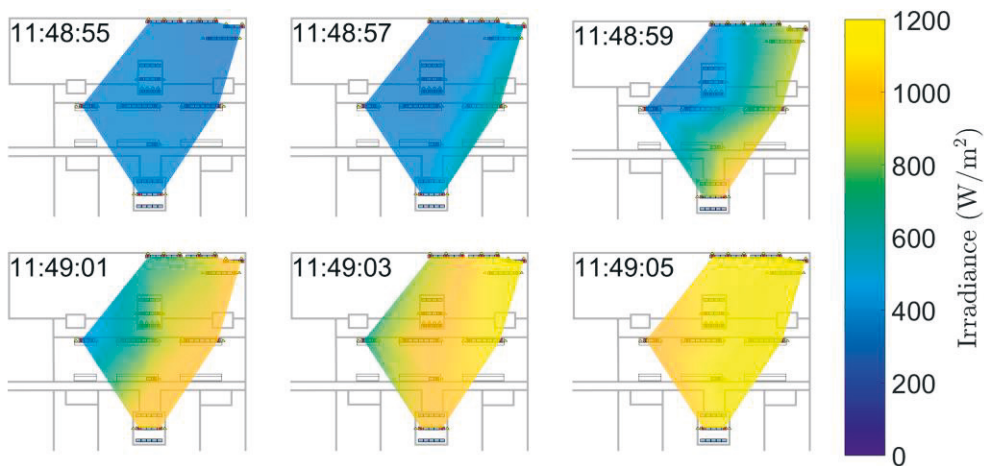


Figure 20. Irradiance profile of a leading edge of an overirradiance area moving approximately from east to west on the rooftop of Tampere University on the 11th of June 2016.

3.3 Data quality assurance

The measurement system is not perfect. Occasionally, some of the irradiance sensors are measuring abnormal irradiance values, there are gaps in the measurement data, or the measurement data is clearly corrupt. These errors in the measurement data may negatively affect the accuracy of the results. Therefore, these periods should be recognized so that the data can be reconstructed if possible, or if needed, the affected sensors, periods, or days can be excluded from the analysis.

The requirements for the data quality depend on what is analyzed. When analyzing the characteristics of overirradiance events from the operation of PV system point of view, it is enough that the midday hours do not have abnormal irradiance values, and gaps in the data in morning and evening periods can be neglected. However, when analyzing, for example, the operating voltage profiles of the PV generator, it would be beneficial to have full days of measurement data because, with a high DC-to-AC power ratio, morning and evening hours may also be relevant. To compare the results between different sections of this dissertation, it is beneficial to keep the dataset the same for all the analyses. Fortunately, due to the large dataset, the criteria for data quality can be strict.

The abnormal measurements are partially due to the non-ideal measurement environment — there are trees and building facades nearby that can cause shadings and reflections on some of the irradiance sensors. Because the panel rows are distributed scarcely so that the front section is not shaded, on some spring days snow albedo can cause irradiance enhancement that is visible on all irradiance sensors. Occasionally there are fast shading events that are caused by birds or some other flying debris. Some of these abnormalities are exemplified in Figure 21. Subfigure (a) presents the irradiance data from some of the pyranometers on the morning hours of April 16th, 2014. During morning hours, nearby trees cast shadows to the TAU PV power research plant. This especially affects the irradiance sensors on the northern side of the TAU PV power research plant (S1 and S5), but other parts of the TAU PV power research plant are also somewhat affected (S12). Sensor S16 on the southern edge of the research plant is largely unshaded. The shading from trees was not found to unduly affect the results, so these anomalies were largely ignored. The input data for the PV generator simulations were taken from the mid-south parts of the rooftop that are less affected by shadings. Subfigure (b) presents irradiance enhancement on some of the pyranometers on the north-east side of the TAU PV power research plant due to reflections from nearby building facades. There is a tall residential apartment building on the east side and a multi-story campus building on the south side of the TAU PV power research plant. Individual sensors are only affected for short durations at a time and the combined effect on the average irradiance is small. The irradiance sensor S12 that was used to estimate the irradiance profiles of overirradiance areas for some of the analyses of this dissertation was found not to be affected by these reflections.

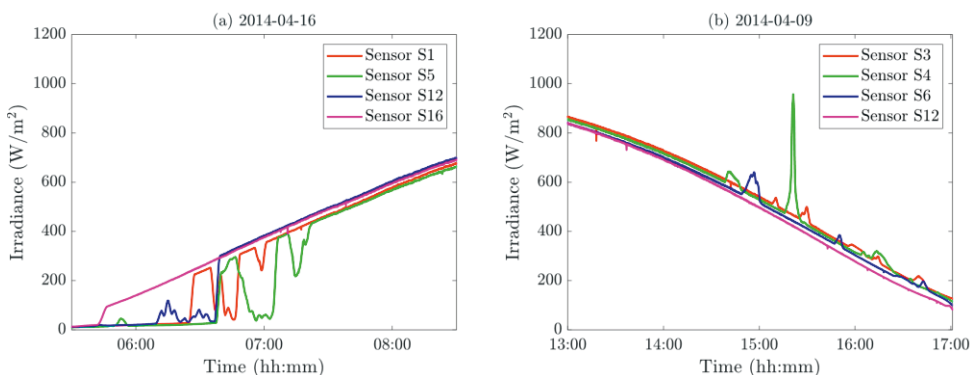


Figure 21. Irradiance as a function of time measured with selected irradiance sensors when some of the sensors are shaded in the morning (a) and some experience an irradiance boost in the afternoon (b).

In addition to the non-idealities of the measurement environment, the data acquisition system itself had occasionally problems that affected the measurement data. For example, there were gaps in data with durations varying from some hundreds of milliseconds up to several days. The gaps in the data were allowed if they occurred in the morning or evening hours when the expected irradiance was less than 100 W/m^2 ; that is, they do not have a noticeable effect on the results. If gaps lasting more than a minute occurred near midday, the days were removed from the analysis. The gaps lasting less than one minute were inspected visually, and if feasible, the missing datapoints were reconstructed by linear interpolation. Figure 22 exemplifies the gaps in the measurement data. Subfigure (a) presents a seven-second gap in the measurement data. In this case, it is possible to reconstruct the irradiance and temperature data by linear interpolation. Subfigure (b) presents a gap in the data with a duration of some tens of minutes. In this case, it is not possible to reconstruct the missing irradiance data, so such days were excluded from the analysis. In addition to measurement gaps, it was possible that the measurement system was storing the data, but there were periods without any variation in the measurements. These periods were systematically recognized, and the data was reconstructed when feasible; and when it was not feasible, it was removed from the analysis.

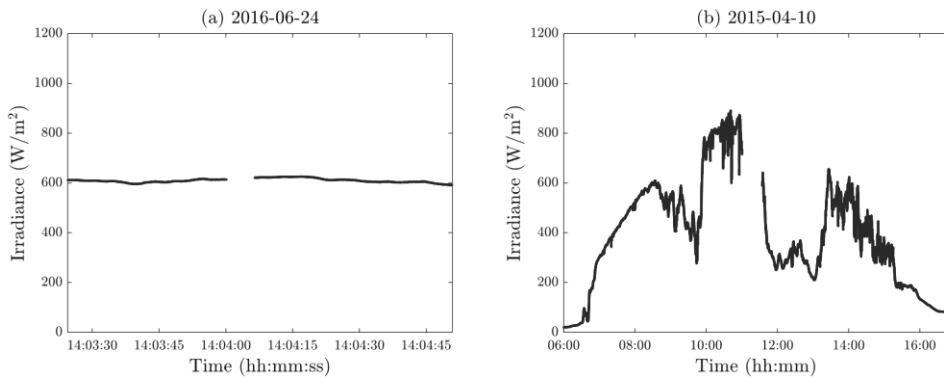


Figure 22. An example of (a) short and (b) long gap in the measurement data.

On some occasions, the irradiance was found to be enhanced due to snow albedo. This phenomenon was observed on some early spring days and confirmed by comparing the irradiance data against historical snow depth data. Its effect on irradiance can be very noticeable, so the overirradiance events on these days clearly stood out from the prevailing trend. Therefore, spring days with possible snow coverage were inspected and affected days were excluded from the analysis. Snow albedo itself is a valid phenomenon that will affect the operation of PV generators,

but considering only the effects of the CE phenomenon, excluding these from the dataset was justified. In addition to snow albedo, the measurements are affected, to some extent, by ground albedo during the summer months. The rooftop has tar-and-gravel surface and the area in front of the pyranometers is mostly open. The 45° tilt angle is close to the typical 35° tilt angle used in Central Europe, and because the point of view of this dissertation is PV power generation, the effect of ground albedo is ignored.

The observation period consisted of 824 days on 23 summer months. After data quality inspection, 27 full days were found to miss measurement data, and 52 days had such gaps and abnormal measurement values that were not possible to reconstruct, so they had to be removed from the analysis. The final dataset consisted of 745 days.

3.4 Cloud shadow speed data

This dissertation utilized cloud shadow speed data, which were obtained by methods and algorithms previously developed and verified in the research group (Lappalainen & Valkealahti, 2016a). In brief, the shading periods are recognized by analyzing irradiance transitions so that the cloud shadow speeds and directions are deduced from the time difference of the transitions between three different sensors. The shading periods were required to have an irradiance fall (the leading edge of a cloud shadow), a steady shading period, and an irradiance rise (the trailing edge of a cloud shadow). The attenuation of irradiance due to shading with respect to unshaded irradiance on the leading and trailing edges of the identified cloud shadows was required to be at least 30 percent. The speeds and directions of the cloud shadows were calculated by the linear cloud edge method. It was assumed that the velocity of the cloud shadow is constant, its edge is linear, and it covers all sensors. Irradiance transitions were parametrized to fit the modified sigmoid function. The cloud shadow speeds and directions can be calculated because the exact locations of the pyranometers are known.

The cloud shadow data were obtained by measurements from sensors S2, S5, and S6 in the northeast corner of the TAU PV power research plant (Figure 17). If a different group of sensor had been used, individual speeds and movement directions would have been slightly different, but the average of the speeds would have been almost the same (Lappalainen & Valkealahti, 2015). During the observation period, 17,598 cloud shadows were recognized on 512 different days. Figure 23 (a) presents

the bar chart of number of days as a function of recognized cloud shadows per day, and Figure 23 (b) presents the bar chart of number of recognized cloud shadows as a function of cloud shadow speed. The mean and median numbers of recognized cloud shadows per day (out of the 512 days, not full dataset) were 37.1 and 22.0, respectively, and the mean and median speeds of the recognized cloud shadows were 13.5 m/s and 10.7 m/s, respectively. Utilization and data quality assurance of the cloud shadow speed data are explained in more detail in Chapter 4.

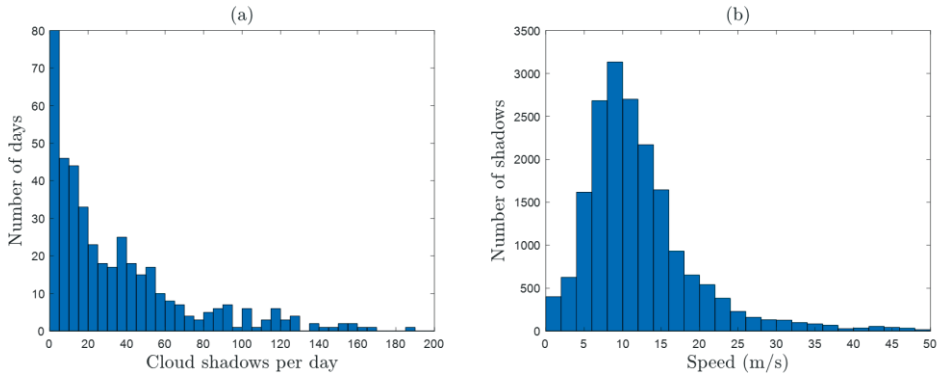


Figure 23. (a) The number of days as a function of recognized cloud shading events per day and (b) the number of recognized cloud shadows as a function of cloud shadow speed during the observation period.

4 RESEARCH METHODS

This chapter presents the methods that were used to analyze the characteristics of overirradiance events and their effect on the operation of the PV generators and PV power plants. The first section presents how the irradiance profiles of overirradiance areas were determined by utilizing the irradiance measurement and cloud shadow speed data. The second section presents the simulation model, and methods that were used to analyze the characteristics of the overpower events caused by the overirradiance events, and how these events affect the operation of PV generators and PV power plants. The last section discusses how the CE and overpower events were defined and how the results are affected by the analysis, methods, and definitions.

4.1 Determining overirradiance event characteristics

This section presents how the characteristics of overirradiance events can be determined based on the irradiance and cloud shadow speed data presented in Chapter 3.

4.1.1 Overirradiance area speeds

Put simply, overirradiance events are caused by redistribution of the photon flux by scattering from the water droplets inside clouds. Cloud geometries can be complex, and clouds can be in multiple layers. Due to wind shear, clouds on different layers can have different speeds and movement directions, so the speeds and movement directions of cloud shadows may not be consistent. However, because overirradiance events are ultimately tied to clouds, their characteristics can be studied by analyzing the movement of cloud shadows. If cloud shadow movement is consistent enough, the speeds of overirradiance areas can be estimated to be the same as the speed of the cloud shadows so that it is possible to estimate the irradiance profile on large

land area based on single point irradiance measurement data. For this, cloud shadow speed data must meet certain criteria.

If the method that was used to estimate the cloud shadow speeds had recognized all irradiance transitions, it would have been possible to analyze each overirradiance event separately by estimating its diameter based on the speed of the leading and trailing edge of the overirradiance area. Unfortunately, such data were not available. However, this shortcoming can be tackled by creating an estimate of the cloud shadow speeds and by comparing the deviation between the estimate and the detected cloud shadow speeds. If the recognized cloud shadow speeds deviate from the estimate only a little, it can be assumed that cloud shadows are moving consistently, and the clouds are predominantly in one layer. In such a case, the overirradiance area movement is also consistent so that the cloud shadow speed estimate gives a reliable prediction of the movement of the overirradiance areas.

A simple and relatively good method to estimate the cloud shadow speeds is to use the daily average speed (Järvelä et al., 2018). However, on days with clearly changing trend in cloud shadow speeds, a higher order polynomial curve fitting provides better results (Järvelä et al., 2020). This is exemplified in Figure 24, which presents the polynomial curve fitting of different degrees on two days with a clearly changing trend in cloud shadow speeds. Based on visual inspection, the daily average cloud shadow speed does not present the data well in either of these two cases. The first-degree estimate follows the trend in Subfigure (a), but in Subfigure (b) the deviation from the datapoint clusters is clearly visible. The third-degree estimate follows the changing trend in both examples. Obviously, using an even higher degree in polynomial curve fitting would provide an even better fit, but the estimate can

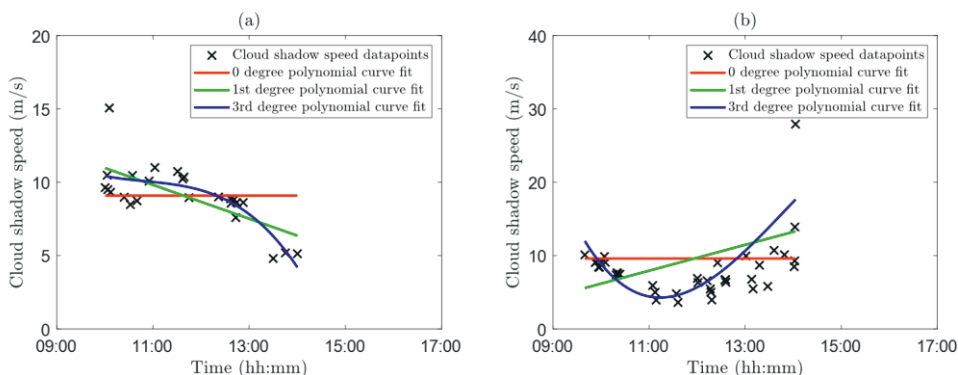


Figure 24. Zero-, first-, and third-degree polynomial curve fitting to the cloud shadow speed data on two days.

become unnatural, for example if the datapoints are in separate clusters. The third-degree polynomial proved to be a good compromise.

The accuracy of the estimate can be evaluated by calculating its relative root mean square error (RRMSE) over the cloud shadow speed values. By using relative values instead of absolute values – that is, the cloud shadow speeds are normalized to the estimate – the cloud shadows with low and high speeds are given the same relative weight. Because the method used to estimate the cloud shadow speeds was based on assumptions that the cloud shadow edge is linear, the velocity is constant, and the sensors are covered by the shadow of the same cloud, it occasionally produces distinctly odd results to the prevailing trend. Before evaluating the estimate, these clearly deviant datapoints were removed from the data set so that the RRMSE of the polynomial curve fit over the remaining datapoints was minimized. Because some of the deviant datapoints are valid (for example, gusts of wind, or clouds in multiple layers), the number of excluded datapoints was chosen to be less than 10 percent of the total number of datapoints. This was done to ensure that the remaining datapoints present the cloud shadow speeds well.

Figure 25 presents the cloud shadow speed estimates on six different days so that the RRMSE increases from 0.0895 in Subfigure (a) to 0.557 in Subfigure (f). The cloud shadow speed estimate follows the cloud shadows speeds well in Subfigures (a) to (d), and the third-degree polynomial curve fit seems to follow well the changing trend of cloud shadow speeds. There is only small deviation between the cloud shadow speed estimate and the datapoints, so the clouds that cause the cloud shadows are likely in one layer and the cloud shadow movement is consistent. Therefore, it is justified to assume that the cloud shadow speed estimate can be used to estimate the speed of the overirradiance areas. In Subfigure (e), the estimate also follows the changing trend in cloud shadows speeds, but there is a cluster of datapoints away from the estimate that causes the RRMSE to have relative high value of 0.2394, even after the removal of 10 percent of deviant datapoints. Based on visual inspection, the cloud shadow speed estimate follows the datapoints reasonably well, but the cluster of datapoints clearly away from the estimate may indicate that considerable number of cloud shadows were cast by clouds in another cloud layer. Subfigure (f) is a good example of a day with a lot of variation in the cloud shadow speeds. The estimate has a high RRMSE value of 0.557, and visually it does not represent the dataset. The datapoints are clearly in two separate clusters during the afternoon hours, so the cloud shadow speed estimate obtained by the algorithm does not present the actual datapoints. This again indicates that cloud shadows were cast by clouds in different cloud layers.

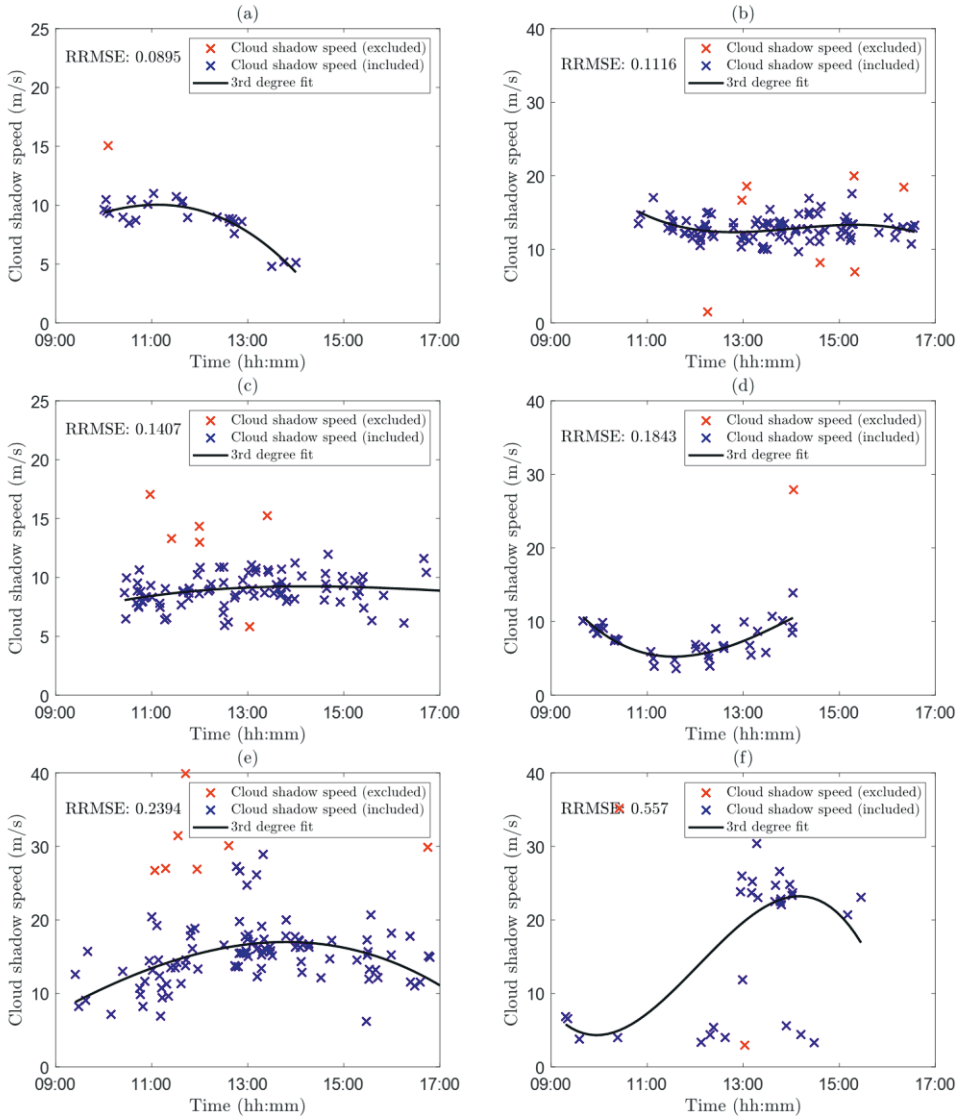


Figure 25. Polynomial curve fitting to the cloud shadow speed data of six different days with varying degree of variation in cloud shadow speeds.

The criteria for including the days into the analysis is strict because 10 percent of the deviant data points, some of which are valid measurements, were removed from the analysis. The RRMSE gives a good estimate of how closely the cloud shadow speeds follow the estimated average speed. To ensure that analysis is limited to days where cloud movement is consistent and clouds are predominantly in one layer, it was chosen that the days must have at least 25 detected cloud shadows and the RRMSE must be under 0.18. Out of the 512 days with recognized cloud shadows,

226 days had 25 or more detected cloud shadows and 86 of those fulfilled the RRMSE criteria. These days with consistent cloud shadow movement contain several thousand overirradiance events, ensuring the statistical relevance of the results.

In addition to analyzing RRMSE values, the validity of the method was assessed by comparing the cloud shadow speed data and the speed estimate together with the cloud shadow movement direction data, and by verifying that the time differences of the irradiance transitions match the estimated cloud shadow speed estimate. Figure 26 (a) presents the recognized cloud shadows speeds and, the speed estimate, and (b) the movement directions of the cloud shadows on the 1st of August 2017. During this day, a total of 145 cloud shadows were recognized throughout the day. At noon, cloud shadows were moving with a speed of 10–16 m/s and the speed estimate was approximately 14 m/s. The RRMSE was 0.138 denoting that the speed estimate presents the datapoints well. The predominant movement direction was from west to east. The deviant datapoints that were removed from the analysis were mainly occurring on midday and they were considerably faster or slower than the estimate. In addition, the movement directions of some of the cloud shadows deviated from the predominant movement direction. The results are affected if some of these removed datapoints are valid and cause overirradiance events, but their impact on statistical analyzes is small because their number is small compared to the number of remaining datapoints.

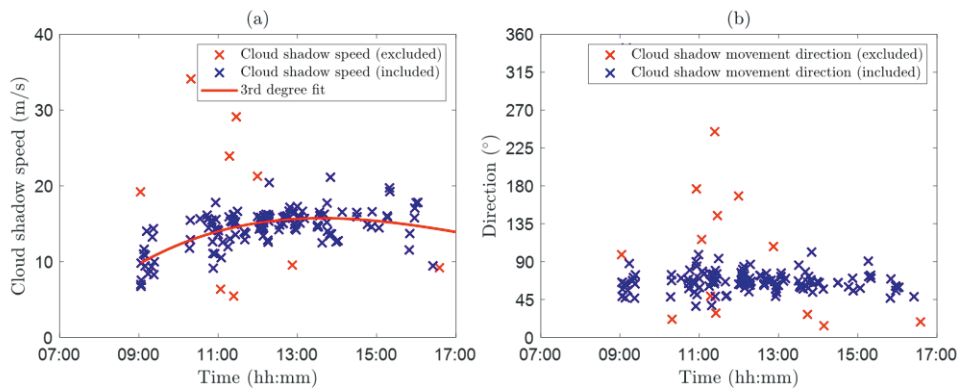


Figure 26. The speed and movement direction of the detected cloud shadows on the 1st of August 2017.

The method was validated also by analyzing synchronized irradiance measurement data from several irradiance sensors to verify that the overirradiance areas are moving according to their estimated speeds, and finally by plotting and

animating the irradiance profile on the TAU PV power research plant. This is exemplified in Figure 27, which presents synchronized irradiance measurements of sensors S1, S9, and S14. The dips in the irradiance are due to cloud shadows, and when they were included in the cloud shadow speed data, their speed is also given. Due to the movement direction of the cloud shadows, sensors S1 and S9 measure almost identical irradiance profiles and the sensor S14 measures similar irradiance profile, but with 2 second delay. This is in line with the 30 m distance between the sensors and approximately 15 m/s movement speed of the overirradiance area. With this speed, the diameter of the overirradiance area marked in the Figure is approximately 2700 meters. The intensity of the irradiance is not very high but is clearly above the expected clear-sky irradiance of 900 W/m^2 .

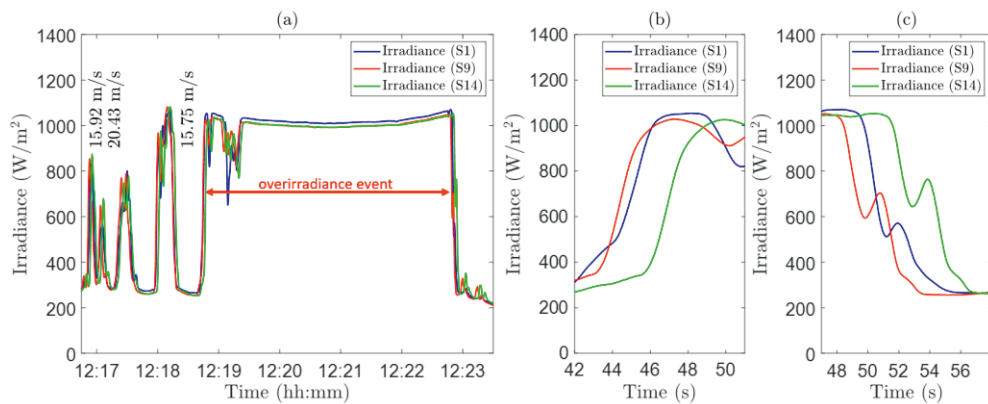


Figure 27. (a) Irradiance data from sensors S1, S9, and S14 (top left, far left and middle right sensors in Figure 17) and the detected cloud shadow speeds on the 1st of August 2017, (b) zoom-in on leading and (c) tailing transition regions of the overirradiance event.

The overirradiance event presented in Figure 27 is illustrated in more detail in Figure 28, which presents the movement of the leading edge (top row) and tailing edge (bottom row) of the overirradiance area. That is, the figure presents the tailing edge of the passing cloud shadow, and the leading edge of the next coming cloud shadow. In this case, the leading and tailing edges of the overirradiance area are relatively smooth and linear. The predominant movement direction of the cloud shadows on that day is approximately from west to east, which can be seen in the movement of the overirradiance area edges on the rooftop. Evidently, the overirradiance area edges are tied to clouds and the speeds and movement directions of the overirradiance areas can be deduced by analyzing the speeds and movement directions of the cloud shadows. Similar visual inspections were performed on several overirradiance events.

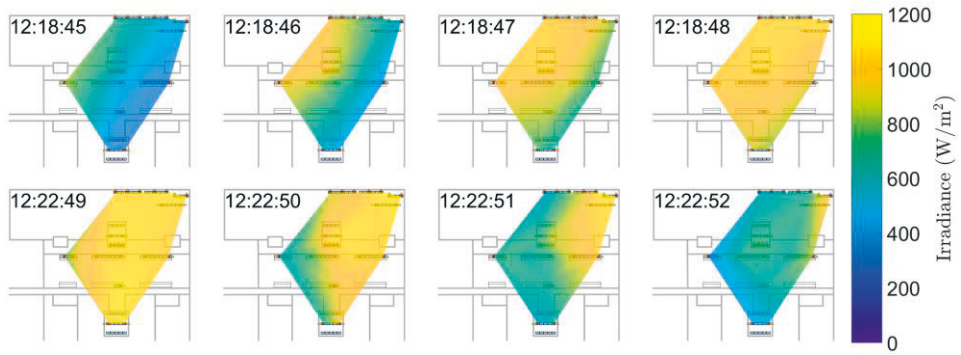


Figure 28. Irradiance profile snapshots of the leading and trailing edges of a cloud shadow passing the rooftop from west to east.

4.1.2 Determining average irradiance over a certain land area

This section presents how the characteristics of overirradiance events were determined by calculating the average irradiance over certain land areas. The average irradiance is used to analyze the occurrence, duration, and intensity of the overirradiance events over land areas corresponding to different PV generator sizes.

To measure the irradiance profile and shape of overirradiance areas accurately and reliably, measurements over a large land area with relatively tight grid of irradiance sensors would be needed. The TAU PV power research plant has a relatively tight array of irradiance sensors, but the diameter of the plant is only of the order of some tens of meters, whereas the diameter of large megawatt scale PV generators is in the order of some hundreds of meters. As such, TAU data can be used to estimate the characteristics of the overirradiance events affecting residential and small commercial PV power plants, but other methods are needed to analyze the characteristics of the overirradiance events on considerably larger land areas.

In this dissertation, the irradiance profile over certain land areas are derived from single point irradiance measurement data by utilizing the overirradiance area speed estimate. For this, five assumptions are made: (i) Taylor's hypothesis of frozen turbulence is applied (Taylor, 1938); (ii) PV generator has a square shape; (iii) the movement direction of overirradiance area is perpendicular to the edge of the PV generator; (iv) irradiance is uniform along the side of the overirradiance area; and (v) the overirradiance area edge is linear. By applying Taylor's hypothesis, the irradiance profile on a certain land area can be assumed to be relatively stable and unchanged. This assumption can be justified because the dataset is selected so that the cloud

shadow movement is consistent. In addition, when calculating the average irradiance over the selected land areas, the observed time-frame is relatively short. This is because the average speed of the overirradiance area is relatively high (10 m/s) in comparison to the studied land areas that have the diameter of the order of some hundreds of meters. Assumption (ii) improves the applicability of the results. For example, spatial smoothing is related to the shortest dimension of the PV generator land area (J. Marcos et al., 2014). In addition, considering complex PV generator geometries would unduly complicate the analysis. Assumptions (iii)–(v) simplify the analysis from two dimensions into one dimension. This can be justified because the average diameter of the cloud shadows is about 800 m and the median diameter is about 300 m (Lappalainen and Valkealahti, 2016).

The simulation model was built so that the input parameters were single-point irradiance measurement data, overirradiance area speed estimates, and the side length of the PV generator. The average irradiance was determined by calculating the non-weighted time average of the single point irradiance. The time average was calculated for each simulation time step based on the PV generator diameter and the cloud shadow speed estimate. The side-lengths of the studied PV generators were chosen so that the study covers residential, commercial roof-top, and medium and large-size utility power plants. Small residential PV systems are typically constructed using small string inverters, and their power rating is in the order of some tens of kilowatts. Commercial roof-top PV systems are typically constructed using multi-string inverters, and the power rating of the PV generators is in the order of 0.1 MW. Utility-scale PV systems are typically constructed using central inverters and their power rating can be several megawatts. Table 1 lists the side-lengths of the selected PV generator types together with their land areas, powers, and power densities. The side lengths were derived from typical land area requirements of the selected PV generator sizes (Ong et al., 2013). The smaller the power rating, the higher is the power density. This is a realistic approach because the smaller the power (size) of

Table 1. Power ratings, land areas, side lengths, and power densities of the studied PV generators.

Type	Side length (m)	Land area (m ²)	Power (MW)	Power density (W/m ²)
Residential	15	225	0.02	100
Commercial roof-top	35	1225	0.1	82
Medium-size utility	125	15,625	1.0	64
Large utility	300	90,000	5.0	55

the PV generator is, the less there is need for space between panels and panel rows so that the power density is higher. The 0.1 MW PV generator with a side length of 35 m closely matches the land area of the TAU PV power research plant, which serves as a reference to validate the results.

The method is exemplified in Figure 29, which presents the estimated average irradiance values of the studied PV generator sizes on a three-minute partly cloudy period. During this period, two distinct overirradiance events occurred; the first had a duration of approximately 33 s and the second had a duration of 13 s. The movement speed of the overirradiance areas was 16.5 m/s and, consequently, the diameters of the overirradiance areas were approximately 545 m and 215 m, respectively. The first overirradiance area is large enough to fully cover all the studied PV generator sizes; therefore, for a moment, the average irradiance of all the studied PV generator sizes was the same. However, the diameter of the second overirradiance area was only 215 m, so the peak average irradiance of the 5 MW (300 m) PV generator was considerably lower than that of the smaller PV generators. The duration of the overirradiance events can also be observed to depend on the PV generator side length. However, if the overirradiance area is considerably larger than the PV generator, the difference in duration is negligible. In addition, due to spatial smoothing, the longer the side length of the PV generator, the slower the changes in the estimated average irradiance. This can be seen as the lower ramp-rates of larger PV generators and smoothing out of short and sudden irradiance fluctuations that

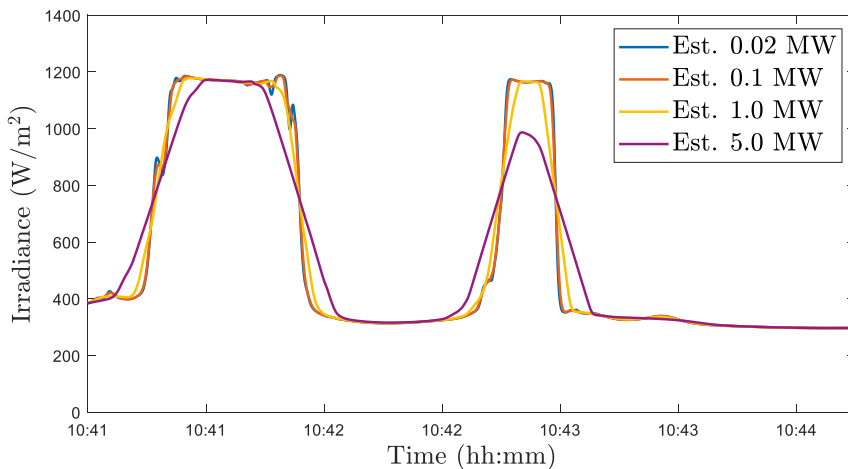


Figure 29. Estimated average irradiances over the studied PV generator sizes on the 27th of July 2015

are still visible in the average irradiance of 0.02 MW (15 m) and 0.1 MW (35 m) PV generators.

To validate the method, Figure 30 compares the actual measured average irradiance on the TAU rooftop and the estimated average irradiance of a 0.1 MW (35 m) PV generator with corresponding areas. The rate of change of irradiance is almost the same on both cases, indicating that the method performs well when the movement speed of the cloud shadows is known. In addition, the timing of irradiance transitions is almost the same because the sensor S12 is in the middle of the TAU rooftop. The small offset in the irradiance values is due to small differences in the orientations of the irradiance sensors. The offset varies depending on the time of day and time of year.

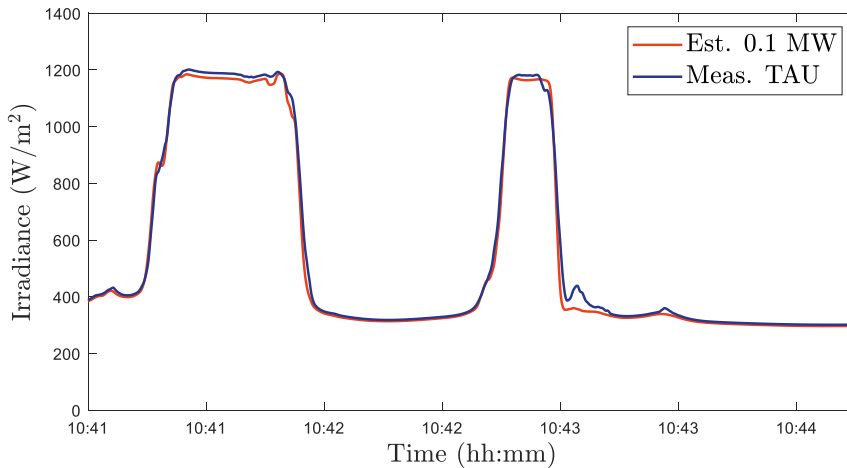


Figure 30. Comparison between estimated and measured irradiances on a 0.1 MW PV generator on the 27th of July 2015.

Compared to the method used in this dissertation, a cloud velocity vector method presented in (Weigl et al., 2012) would provide slightly more reliable estimate of the irradiance profile in two dimensions. Unfortunately, due to the relatively small size of TAU PV power research plant, such method would not considerably increase the reliability of the estimate. The cloud vector velocity method is also insufficient to accurately determine the irradiance profile of overirradiance areas with a diameter of several kilometers. However, when estimating the average irradiance over land areas of typical PV generator sizes, our method provides reliable results due to relatively short side length of even the largest PV generator sizes in comparison to the speed

of overirradiance areas. Naturally, the smaller the studied land area, the better the estimate.

4.2 Determining the effect of overirradiance events on PV generators and PV power plants

When studying the effect of the overirradiance events on the operation of PV power plants, the analysis must take a step towards a case study. This is because the operational characteristics of PV generator depend on the configuration of the PV panels and the control method. Due to limitations set by the research data, simulating the operation of large utility-scale power plants is not feasible; therefore, the size of the studied PV generator was selected to be in the range of typical commercial rooftop PV power plants. The first part of this section presents the simulation model of the studied PV generator, and the second part presents how the simulated PV power plant was controlled.

4.2.1 PV generator model and simulation parameters

The analysis is based on simulation model of NAPS NP190GKg PV panel that was implemented in a Matlab's Simulink environment based on the well-known single diode model (Appendix A). The PV panel was modelled as 54 series connected PV cells with one bypass diode. Simulation model parameters are presented in Table 2. These were obtained based on datasheet values of the PV panel and the methods presented in (Villalva et al., 2009).

Table 2. Simulation parameters of NP190GKg PV panel.

Parameter	Value
Series resistance, R_S	0.3 Ohm
Shunt resistance, R_{SH}	177 Ohm
Diode ideality factor, A	1.3
Temperature coefficient for OC voltage, K_U	-0.124 V/K
Temperature coefficient for SC current, K_I	0.0047 A/K
Number of cells in series, N_S	54

The electrical characteristics of NP190GKg PV panel are presented in Table 3. The nominal power is low by modern standards, but otherwise the panel characteristics are similar to other c-Si PV panels that are widely used in energy production applications. Changing the panel type to half-cell or other more modern panel technology should provide similar results.

Table 3. Electrical characteristics of NP190GKg PV panel.

Parameter	Value
Short-circuit current in STC, $I_{SC,STC}$	8.02 A
MPP current in STC, $I_{MPP,STC}$	7.33 A
Open-circuit voltage in STC, $U_{OC,STC}$	33.1 V
MPP voltage in STC, $U_{MPP,STC}$	25.9 V
Nominal power in STC, $P_{MPP,STC}$	190 W

The land area covered by irradiance sensors on the TAU PV power research power plant corresponds approximately to the land area of a 0.1 MW PV generator. The covered area is not square, but rather an irregular polygon. It would not be out of the question to investigate a PV generator of this shape, but a square shape is more in line with typical PV generators and therefore better in terms of practicality and significance of results. This is because the shortest dimension of the PV generator defines the maximum ramp-rates of power fluctuations (de la Parra et al., 2015). In addition, when considering the irradiance characteristics of the overirradiance events, the intensity and the duration of the overirradiance events have been found to depend on the side-length of the PV generator (Järvelä et al., 2020).

The studied PV generator size was chosen to be in the power range of a typical commercial rooftop PV power plant constructed with a multi-string inverter. The PV generator consists of seven parallel connected strings, each having 24 series connected NP190GKg PV panels. For the sake of simplicity, the shape of the PV generator is set as an equilateral square with a side length of 20 m. The locations of the PV panels and their configuration on the rooftop of Tampere University are presented on top of an irradiance profile example in Figure 31. The PV panels are evenly distributed over the land area and the PV strings form east–west loops so that there are 12 panels per row and two rows per string; that is, the design is practical and realistic considering cabling and panel dimensions. With this design, the nominal open circuit voltage of the PV generator is 794 V, the short circuit current 56.1 A,

and the MPP power 31.92 kW. These values are used for reference when presenting the results. The power density of this PV generator design is approximately 80 W/m², which is typical for this power scale (Ong et al., 2013).

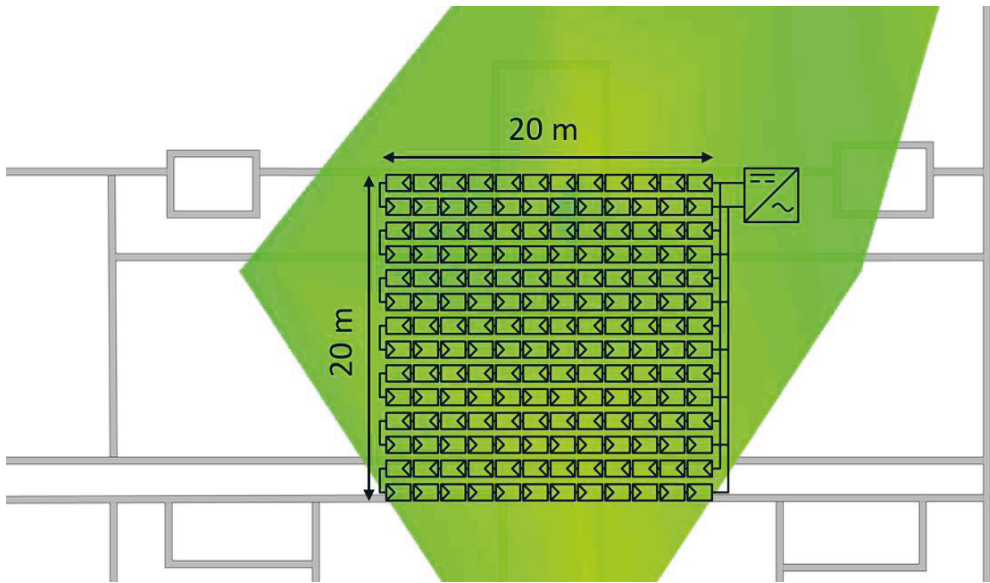


Figure 31. The dimensions and configuration of the 32 kW PV generator, and its location on the rooftop.

The simulation parameters are irradiance and PV panel temperature. Irradiance was determined based on the irradiance at the center of each PV panel, and it was assumed to be uniform over PV panel. Sub-module or cell level simulations would have provided slightly better accuracy, but most of the mismatch losses caused by cloud shadows are found to be occurring due to mismatches between PV panels (Lappalainen & Valkealahti, 2018). The selected simulation resolution is a good compromise between accuracy and simulation time. The operating temperature was determined based on measurement data from sensor T12 in the middle of the research power plant, and it was assumed to be the same for all PV panels. This is a valid assumption because, due to the small size of the PV generator, all PV panels are exposed to almost the same irradiance conditions. In practice, the PV panels near the edges of the PV generator might have slightly lower operating temperatures than the panels in the central region due to stronger cooling effect of wind. It would have been possible to calculate the operating temperature of each PV panel by utilizing actual wind speed, ambient temperature, and irradiance data, but the PV panel temperature data were used instead because they were already available.

The simulation model was built in Matlab environment. To improve the calculation speed, the simulations were carried out by utilizing table lookup method. PV panel specific $I-U$ curves were pre-calculated for each irradiance and PV panel temperature combinations. The resolution for $I-U$ curves was 1000 points, for irradiance 0.25 W/m^2 , and for PV panel temperature $0.25 \text{ }^\circ\text{C}$. This provides a good compromise between accuracy and simulation time (Lappalainen & Valkealahti, 2017b).

4.2.2 Power limiting and inverter model

When studying the effect of the overpower events on the operational characteristics of the PV power system, the simulation model needs to be expanded to also cover the operation of the solar inverter. The inverter is needed to transform the DC current from the PV generator into AC current to be fed into the power grid. The inverter controls the power of the PV generator by controlling its operating voltage. When the inverter is operating in maximum power point tracking (MPPT) mode, it tries to maximize the energy yield by maximizing the power of the PV generator. MPPT algorithms are needed because the $I-U$ characteristics of the PV generator are changing with the operating conditions.

In this dissertation, the MPPT algorithm was assumed to be ideal; that is, the operating point of the PV generator is always on the global MPP, or when the MPP power was more than the maximum power of the inverter, the operating point was on the high voltage side of the global MPP on the first possible occasion where the PV generator power equals the maximum power of the inverter. Even though the MPPT algorithms are relatively slow to follow the MPP, the control loops that limit the operating power (current) are fast to react to overpower events; therefore, assuming an ideal control algorithm for MPPT and power limiting should not unduly affect the results. One consequence of using the ideal MPPT algorithm is that the operating point may shift quickly between two or more voltage levels during partial shading conditions when there is more than one MPP.

The conversion efficiency of the inverter is assumed to be 100%. This assumption will not unduly affect the results because conversion efficiencies of commercial inverters are typically 98-99% when operating at full power. The inverter is also assumed to have constant power limit, which is not changing as a function of ambient temperature or operating point. This is also a valid assumption if the inverter is located indoors in controlled conditions, which may be the case in

commercial roof-top applications. The inverter model did not have limits for minimum or maximum DC voltage. By setting a limit for the minimum DC voltage, the fast jumping of operating voltage caused by the ideal MPPT algorithm could have been reduced slightly, but this would not have noticeable effect on the results.

The effect of power-limiting and different DC-to-AC power ratios to the operating voltage of the PV generator was studied by keeping the PV generator configuration and power the same and varying the inverter power limit so that the DC-to-AC power ratio was varying between 1.0 and 2.0. In typical installations, DC-to-AC power ratio is over 1.0, and a power ratio of 2.0 is already an extreme case.

The above-described inverter model was implemented in Matlab environment. The simulations were performed by loading the $I-U$ curve of the PV generator for each time-step and then by setting the current, power, and voltage to match the global MPP, or if the power was higher than the power-limit, it was set on the high-voltage side of the global MPP on first possible point.

4.3 Analysis of the overirradiance and overpower events

When considering overirradiance events caused by CE phenomenon, it is first necessary to find out what the event is. The literature has provided various definitions depending on the context. Typically, overirradiance events have been detected by comparing the irradiance to, for example, STC irradiance of 1000 W/m^2 , expected clear-sky irradiance, expected clear-sky peak irradiance or some other static or varying irradiance limit. The STC irradiance of 1000 W/m^2 is a natural limit from the PV power generation point of view, but on many locations, especially near the equator, the GTI can exceed 1000 W/m^2 during clear-sky conditions. Clear-sky irradiance varies by the time of the day and year due to changes in the sun path. It also depends on upper atmospheric conditions, such as aerosol and particle content in the air. These can increase due to forest fires, for example, and then decrease due to rainfall, meaning that the clear-sky irradiance can vary considerably, even on consecutive days. There are various methods for including the effect of atmospheric particle content in forecast models (Ruiz-Arias, 2021), but typically a 5 percent margin is used to reduce the number of false detections due to the variable nature of the clear-sky conditions (Starke et al., 2018).

The suitability of the different methods to detect the overirradiance events depends on the use-case. For example, in PV applications the requirement for the

definition differs depending on whether the effects of the overirradiance events are considered on the point of view of yield forecasting or operation of the inverter. When considering yield forecasting, especially in the short term, the overirradiance events occurring in the morning or evening hours matter, whereas when only the operation of the inverter is considered, high-intensity events are more relevant. In addition, just detecting the overirradiance events is not enough because their diameter, duration, and intensity varies. Therefore, overirradiance events need to be categorized in a simple and easily understandable way.

Because the short circuit current of the PV generator depends almost linearly on the irradiance, a good approach is to categorize the overirradiance events based on irradiance; such as, systematically detecting the overirradiance events where the irradiance exceeds a certain value. Now, the beginning and end of an overirradiance event can be defined precisely and the events can be further characterized based on their duration. This method can be used when analyzing overirradiance areas, or overirradiance events over larger land areas. It is also suitable for characterizing the overpower events of PV generators.

This simple method is used in this dissertation. It is exemplified in Figure 32, which presents the single point irradiance measurement and the corresponding estimated average irradiance on PV generators with side lengths of 35 m (0.1 MW) and 300 m (5.0 MW). The average irradiance over the 0.1 MW PV generator follows

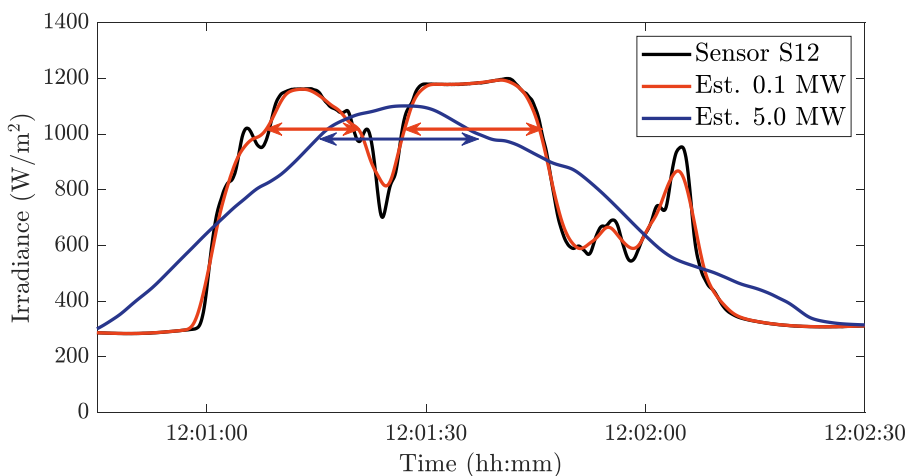


Figure 32. Irradiance measured by sensor S12 and corresponding estimated average irradiance over land areas corresponding to 0.1 and 5 MW PV generators on 18th of July 2017.

the single point irradiance quite closely; consequently, there are two overirradiance events (red arrows) with durations of 15 s and 19 s. However, under the same irradiance conditions, there is only one overirradiance event (blue arrow) on a 5 MW PV generator with a duration of 29 s. The average irradiance over the 5 MW PV generator remains over the 1000 W/m² limit, even though there is a brief dip in the measured single point irradiance. In addition, the peak average irradiance of the 0.1 MW PV generator reaches 1200 W/m² but is only 1100 W/m² for the 5 MW PV generator. It should be noted that, by using this method, the average irradiance can occasionally drastically exceed the set irradiance limit.

To further exemplify the effects of this method, Figure 33 presents single-point irradiance data from sensor S12 on a 10-minute period on the 7th of June 2018. During this period, two overirradiance events occurred that lasted approximately 65 s and 127 s. Even though the irradiance of both overirradiance events was close to 1200 W/m², they were distinctly different in nature. During the first overirradiance event, the irradiance fluctuated fast, whereas during the second overirradiance event it remained on an almost constant level. If the irradiance limit is set to 1000 W/m² and only single-point irradiance data is analyzed (no spatial smoothing), the first event consists of three consecutive overirradiance events, but the second event would still be counted as one. In case the irradiance limit is 1200 W/m², the first overirradiance event would consist of seven events, but the second event does not exceed the limit at all. Time averaging the irradiance data would remove the fast fluctuations, but then overirradiance events with sharp focus points would be unduly removed from the analysis or their irradiance would be estimated to be lower than the actual one.

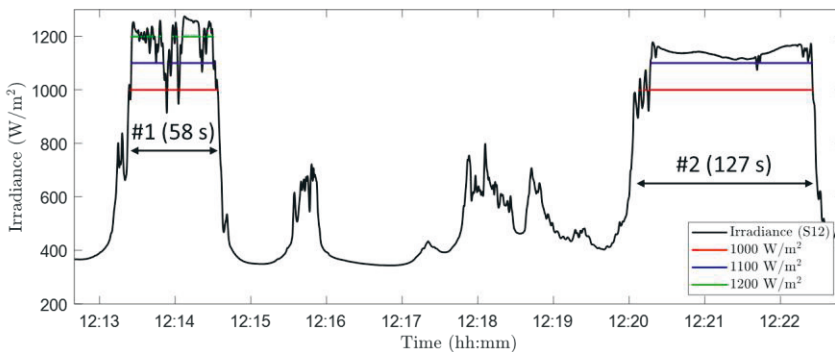


Figure 33. Measured irradiance with sensor S12 and detected overirradiance events with three different irradiance limit values during a short period on the 7th of June 2018.

In this dissertation, CE and overpower events were counted similarly so that the events were defined to start when the irradiance or power exceeded the reference value, and end when it dropped below it, as presented in Figure 33. Thus, this dissertation answers the question on how long time the irradiance or power exceeds a certain value, but it does not directly consider the peak value. Therefore, the average irradiance and power can occasionally drastically exceed the set limit value and, counter-intuitively, the number of events can even increase if the reference value is increased slightly, as exemplified in Figures 32 and 33.

When analyzing overirradiance event characteristics, the results can be used to estimate the theoretical maximum photocurrent that can be achieved with optimal PV generator configuration. In practice, this overestimates the results somewhat because there are always some mismatch losses. When analyzing the overpower events, the mismatch losses are baked in into the simulation model. Various methods presented to optimize the PV panel layout against partial shading conditions were not considered mainly because they are not used in practice, and secondly, because they would unduly complicate the analysis. (Paasch et al., 2014), showed that the mismatch losses depend on the movement direction of cloud shadows. Therefore, the simulations were performed with different string orientations but there were no noticeable changes in overall results. Regardless, many of the parameters causing non-homogenous conditions for the PV generator have finally been revealed to cause only marginal energy losses. For example, different panel configurations have been shown to have only a small practical effect on mismatch losses (Lappalainen & Valkealahti, 2017a), and having multiple maximum power point trackers on spatially long PV string does not affect the net energy gain in the long term (Paasch et al., 2015).

5 CHARACTERISTICS OF OVERIRRADIANCE EVENTS

This chapter discusses the characteristics of overirradiance areas and overirradiance events. The first section discusses overirradiance areas; that is, how the occurrence and diameters of the land areas of enhanced irradiance change with changing irradiance. The second section discusses overirradiance events from a PV power generation point of view; that is, how the occurrence and duration of overirradiance events over land areas of PV generators of different sizes change with changing irradiance. The analyses are based on determining the irradiance profiles of the overirradiance areas by utilizing irradiance measurement, and cloud shadow movement data presented in Chapter 3, and methods presented in Chapter 4. To obtain consistent results, the analyses are limited to days with consistent cloud shadow movement.

5.1 Occurrence and diameters of overirradiance areas

This section discusses the occurrence and diameters of overirradiance areas. Due to the requirements set by the research method, the diameters of overirradiance areas can be determined only on days with consistent cloud shadow movement. However, the occurrence and duration of the events are also presented for the full dataset.

5.1.1 Occurrence of overirradiance areas

Figure 34 presents the cumulative number of overirradiance events detected by one single point irradiance sensor as a function of irradiance. The blue line presents the number of overirradiance events during the full 745-day dataset, and the red line presents the number of overirradiance events during the 86 consistent days. The number of overirradiance events decreases quickly with increasing irradiance. Altogether, the irradiance exceeded the STC irradiance of 1000 W/m^2 over 16,000 times during the full observation period and over 4500 times during consistent days;

that is, over 20 and 50 times per day, respectively. The number of detected overirradiance events per day is approximately 2.5 times higher on consistent days than on the full dataset days. It should be noted that all the consistent days had long partly cloudy periods with at least a minimum of 25 recognized cloud shadows, whereas the full dataset also consists of fully overcast and clear-sky days. The occurrence of events (and areas) decreases similarly, with increasing irradiance during consistent days and the days of the full dataset.

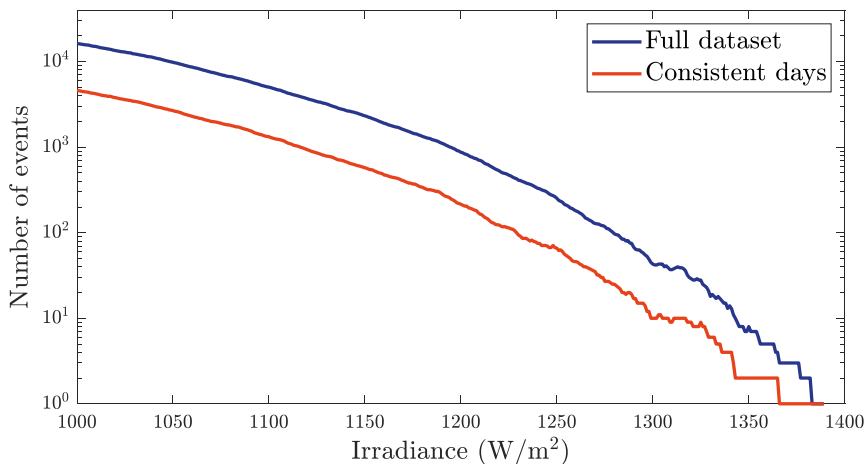


Figure 34. Cumulative number of the overirradiance events as a function of irradiance on days with consistent cloud shadow movement and on days of the full dataset.

5.1.2 Diameter of overirradiance areas

The diameters of overirradiance areas were deduced from the time it took for overirradiance areas to pass over an irradiance sensor (that is, the duration of the overirradiance event) and the known speeds of overirradiance areas. For this, Figure 35 presents the maximum, mean, and median durations of overirradiance events as a function of irradiance on the full data set (blue lines) and on consistent days (red lines). The durations of overirradiance events decrease with increasing irradiance. The duration of the longest overirradiance event with irradiance exceeding the STC irradiance of 1000 W/m² was over 20 minutes, and the duration of events with an irradiance exceeding 1200 W/m² can be a few minutes. The mean duration of the overirradiance events is some tens of seconds and median duration is some seconds, decreasing slightly with increasing irradiance. The maximum

durations of the overirradiance events were considerably longer on the full dataset compared to days with consistent cloud shadow speeds, but the mean and median durations of the overirradiance events is almost the same between the full dataset and the consistent days. The full dataset includes the consistent day dataset, which mainly explains the differences between the maximum durations. In general, these results are in line with other papers, where the overirradiance events have been reported to exceed the STC irradiance for several minutes (de Andrade & Tiba, 2016; Yordanov, Midtgård, et al., 2013).

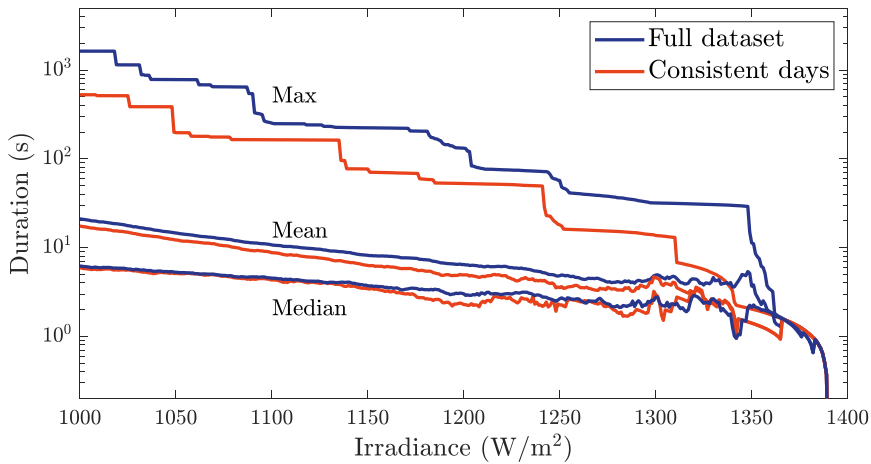


Figure 35. Maximum, mean, and median durations of overirradiance events on the full dataset and on the days with consistent cloud shadow movement.

Figure 36 presents the maximum, mean, and median diameters of overirradiance areas on consistent days. These diameters were deduced from the durations of the events by utilizing the cloud shadow speed estimate; therefore, the analysis must be limited to consistent days. The maximum diameter of overirradiance areas can be several kilometers, decreasing quickly with increasing irradiance. The mean diameter is some hundreds of meters, decreasing slightly with increasing irradiance, and the median diameter of the overirradiance areas is some tens of meters throughout the irradiance range. The step-like behavior of the maximum overirradiance area diameter curve is due to single overirradiance areas defining the curve in a certain irradiance range. In fact, the maximum overirradiance area diameter curve is determined by only 12 overirradiance events on nine different days. In general, these results are in line with the results published in (Lappalainen & Kleissl, 2020), where the methods presented in (Järvelä et al., 2018) were used to determine the

overirradiance area diameters. They also concluded that diameters can be up to several kilometers strongly decreasing with increasing irradiance, and that the median diameter is of the order of some tens of meters slightly decreasing with increasing irradiance.

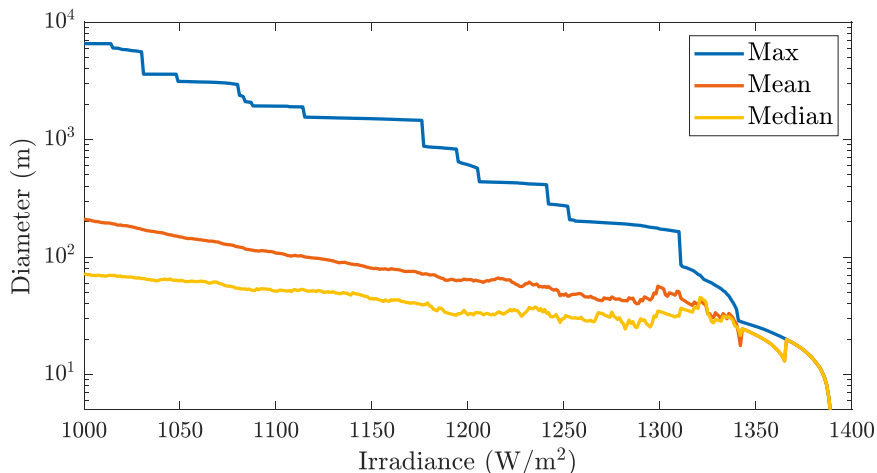


Figure 36. The maximum, mean, and median diameter of the overirradiance areas as a function of irradiance on the days with consistent cloud shadow movement.

To provide a better picture of the overirradiance area diameters, Figure 37 presents the diameter distributions for irradiance values exceeding 1000, 1100, and 1200 W/m². Approximately 10 percent of the overirradiance events on all irradiance values have a diameter of less than 10 meters. These short-diameter events are partially due to the used method to detect the overirradiance events, and they are caused by the irradiance peaking at a certain value or by the small ripple in the irradiance. The typical diameter of overirradiance areas is some tens of meters and increases with decreasing irradiance up to few hundreds of meters for irradiances close to the STC value having only 10–20 percent irradiance enhancement. The longest observed overirradiance area diameters are in the order of several kilometers. In practice, this means that the overirradiance event lasted for several minutes at the measurement point. The diameter of overirradiance areas above 1200 W/m² is typically from tens of meters to few 100 meters.

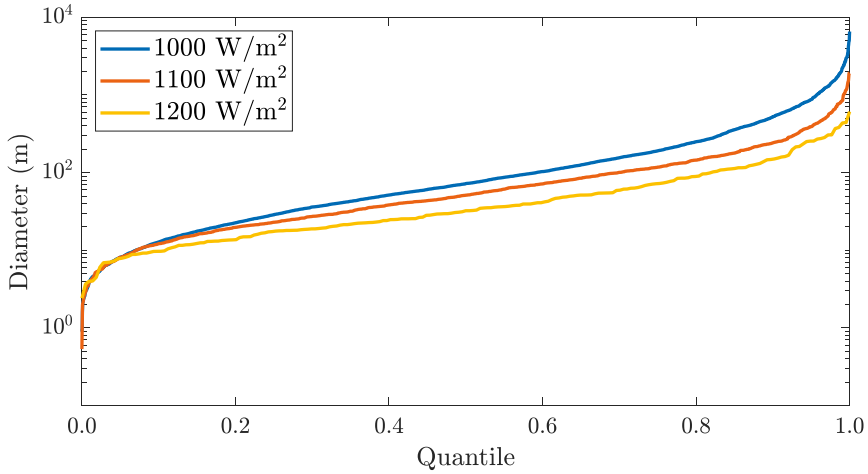


Figure 37. Distributions of overirradiance area diameters exceeding different irradiance limits.

5.2 Occurrence and durations of overirradiance events over land areas of PV generators of different sizes

This section discusses the occurrence and duration of overirradiance events from the PV power generation point of view. The diameter distributions of overirradiance areas can be used to analyze the effect of CE phenomenon on PV generators. That is, it is possible to determine whether an overirradiance area can fully cover PV generators of different sizes. As presented in Section 5.1, the median diameter of the overirradiance areas is some tens of meters. Therefore, residential, and small commercial rooftop installations are affected by almost all overirradiance events. The maximum diameter of the overirradiance areas can be several kilometers, so even the largest megawatt scale PV generators are affected by overirradiance events. When considering the duration of the overirradiance events, the speed of the overirradiance area must be taken into consideration. In addition, due to spatial smoothing, small local dips in irradiance may be filtered out. This section presents the results on the characteristics of the overirradiance events over land areas of PV generators of different sizes. The analysis was made using the methods presented in Section 4.1.

5.2.1 Occurrence of overirradiance events

The cumulative numbers of overirradiance events as a function of irradiance on the studied generators sizes are presented in Figure 38. The number of overirradiance events decrease with increasing irradiance and with increasing size of the PV generator. In addition, the maximum irradiance decreases with increasing PV generator size. These findings are in line with the durations overirradiance events and diameters of the overirradiance areas presented in Figures 35 and 36, respectively.

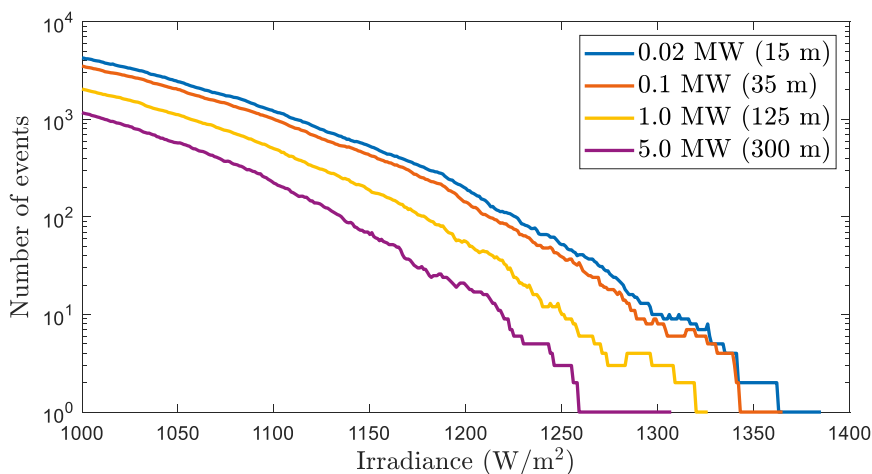


Figure 38. The number of overirradiance events in the studied PV generators as a function of irradiance.

The number of events presented in Figure 38 cannot be directly used to analyze the overall occurrence of overirradiance events. This is because the dataset consisted of partly cloudy days with at least 25 identified shading events per day. However, the results can be used to compare the occurrence of the events between PV generators of different sizes. During the 86-day observation period, the irradiance measured with a single pyranometer exceeded the STC irradiance of 1000 W/m² approximately 6000 times, and the average irradiance of the 0.1 and 1 MW PV generators exceeded it by more than 3000 and 2000 times, respectively. The relative difference between the numbers of overirradiance events on 0.1 MW and 1 MW PV generators increases with increasing irradiance limit. This is plausible due to the increase of spatial smoothing of irradiance with increasing generator area. Anyhow, the ratio of overirradiance events exceeding 1000 W/m² observed on land areas corresponding

to 0.02 MW (15 m) and 5.0 MW (300 m) PV generators is approximately 3 to 1. This is in line with the results presented in (Lappalainen & Kleissl, 2020), where the ratio of overirradiance events exceeding 1000 W/m^2 between 0.05 MW (25 m) and 4 MW (250 m) PV generators is similarly close to 3 to 1. Like in this dissertation, they used the method presented in (Järvelä et al., 2020) to count the number of overirradiance events.

5.2.2 Durations of overirradiance events

Figure 39 presents the maximum durations of the overirradiance events as a function of irradiance for the studied PV generator sizes. The maximum duration decreases quickly with increasing irradiance. Regardless of the PV generator size, the average irradiance over the generator can exceed STC irradiance for several minutes. For irradiance of 1100 W/m^2 the maximum durations were approximately two minutes, for 1200 W/m^2 several tens of seconds, and for 1300 W/m^2 approximately ten seconds. For all the studied PV generator sizes, the maximum durations of the overirradiance events were approximately the same, up to the irradiance value of 1300 W/m^2 . This is because the maximum diameters of overirradiance areas are typically considerably longer than the diameters of the PV generators. The PV generator size had a noticeable effect on the maximum duration only when the

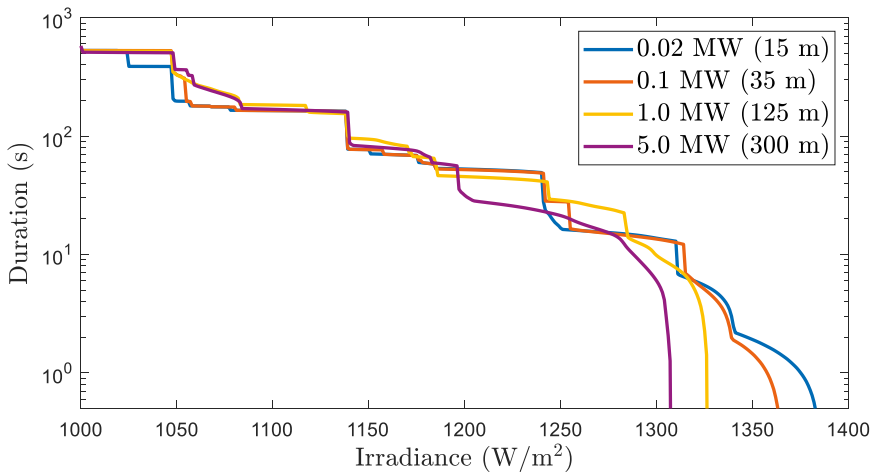


Figure 39. Maximum durations of overirradiance events in the studied PV generators as a function of irradiance.

irradiance of the overirradiance event exceeds 1300 W/m^2 . Peak irradiance for the 0.02 MW PV generator with a side length of 15 m was close to 1400 W/m^2 , and for the 5 MW PV generator with a side length of 300 m it barely exceeded 1300 W/m^2 . This is obvious because the diameters of the strongest overirradiance areas are only some tens of meters. The steps in the maximum duration curves are due to single events defining the maximum durations in certain irradiance ranges.

Figure 40 presents the mean and Figure 41 presents the median durations of the overirradiance events for the studied PV generator sizes. The mean duration of overirradiance events exceeding the STC irradiance varied from 20 seconds up to 50 seconds, and the median duration of overirradiance events exceeding the STC irradiance varied from eight seconds up to twenty seconds, both increasing with increasing PV generator size. The mean and median durations of the overirradiance events both had a decreasing trend with increasing irradiance. The maximum, mean, and median durations have similar distributions as the overirradiance area diameters presented in Figure 37. That is, overirradiance events with long duration seldom occur and most events have a short duration. The increase of mean and median duration of overirradiance events with increasing PV generator size is somewhat counter-intuitive but can be explained by looking at the overirradiance area diameter distributions and considering the spatial smoothing of irradiance. The small dips in irradiance are visible in smaller PV generators but they are smoothed out in larger PV generators, which increases the average duration of overirradiance events detected by large PV power plants.

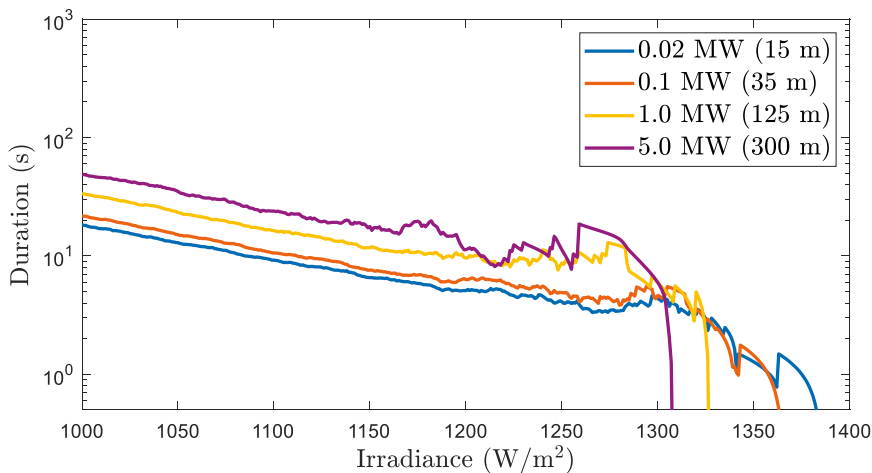


Figure 40. Mean durations of overirradiance events in the studied PV generators as a function of irradiance.

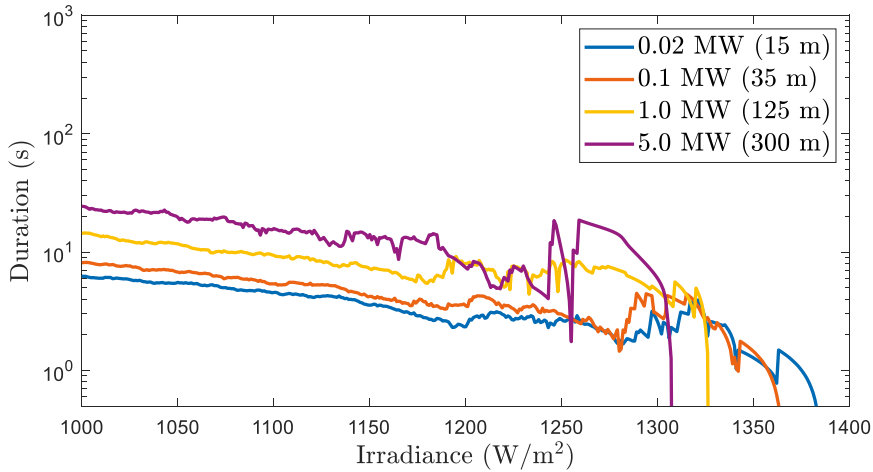


Figure 41. Median durations of overirradiance events in the studied PV generators as a function of irradiance.

5.3 Possible effects on the operation of PV generators

Section 5.1 showed that overirradiance areas can fully cover even the largest utility-scale PV generators, and Section 5.2 showed that the overirradiance events on PV generators have a typical duration of some tens of seconds, regardless of the PV generator size. The short circuit current of a PV panel is almost directly proportional to the irradiance; therefore, during overirradiance events, the current of a PV generator or its subsections can be considerably higher than the nominal current. If the inverter rating is higher than the PV generator nominal power, it is possible that the operating current is not limited, in which case the actual operating current of the DC side fuses and cables can be considerably higher than expected. The DC side components may also receive full short-circuit current if, instead of disconnecting the PV generator, it has been shut down by short-circuiting it (Spataru et al., 2013).

In practice, (slow) fuses are resistors that are designed so that when the operating current is less than the rated current, they can dissipate the heat generated in the weak links of fuse elements inside the fuse body, and in case the operating current is more than the rated current, heat dissipation is not sufficient so that fuse elements gradually heat up and the fuse eventually operates. In PV applications, string and array fuses are typically of gPV type, which are full-range fuses with time–current characteristics designed to fit solar applications (IEC, 2010). As a general rule of

thumb, the fuse rating should be more than 1.56 times the short circuit current of the string or array (Eaton, 2021). DC-side cabling should also be designed so that, under expected operating conditions, the DC-side fuses protect the cables. The irradiance during the strongest overirradiance events observed on TAU PV power research plant was approximately 1.4 the nominal STC irradiance of 1000 W/m², and the durations of the strongest events were in the order of some seconds. Based on the typical sizing rules and time–current characteristics of gPV type fuses, the overirradiance events observed on TAU PV power research plant do not cause nuisance fuse operations. Several studies have reported that the irradiance during the strongest measured overirradiance events around the world exceeds 1800 W/m². With 200 percent of the rated current, the pre-arcing time of gPV type fuses is of the order of 100 seconds, and with 150 percent of the order of 1000 seconds (Eaton, 2021). Therefore, if the fuse rating has been selected to be over 1.56 times the nominal short circuit current, the durations of the strongest overirradiance events ever recorded must be of the order of 1000 seconds to make the fuse operate. Therefore, it can be concluded that overirradiance events cannot cause nuisance fuse operations if typical design rules have been followed. Ageing of fuses (Kuhnel et al., 2017; Zhang et al., 2020) or partial shading conditions may contribute to the nuisance fuse operations, but this is not related to CE phenomenon, per se.

In certain conditions, overirradiance events have been reported to cause nuisance fuse operations. For example, (do Nascimento et al., 2019) reported that a certain PV panel manufacturer required a fuse with a certain rating so that the warranty would not be voided. In this case, the fuse rating was well above the rated short-circuit current, but due to temperature derating, the actual rating of the fuse was close to the PV panel short-circuit current, so that an overirradiance event with an irradiance of 1500 W/m² and duration of five minutes caused the fuse to operate. However, (do Nascimento et al., 2019) also stated that, when following typical design rules and sizing factors, overirradiance events should not cause nuisance fuse operations.

6 OVERPOWER EVENTS CAUSED BY THE CLOUD ENHANCEMENT PHENOMENON

This chapter discusses overpower events caused by the CE phenomenon. The first section discusses the characteristics of the overpower events; the second section discusses the operation of PV power plants during the overpower events; and the third section discusses the effects of overpower events on the operation of solar inverters. The analyses were performed by simulating the operation of a large residential-size PV generator. The $I-U$ and $P-U$ curves of the PV generator were studied to analyze the occurrence, duration, and power of the overpower events. They were also used to deduce how the operating voltage of the PV generator behaves during overpower events, and how power limiting affects the operating voltage as a function of DC-to-AC power ratio.

6.1 Characteristics of the overpower events

This section discusses the characteristics of the overpower events. Irradiance characteristics presented in Chapter 5 can be used to estimate the short circuit current, but the $P-U$ curve and MPP power also depends on the configuration and the operating temperature of the PV panels. Overpower events are analyzed based on the simulation model of a 32 kW PV generator presented in Chapter 4 and the irradiance and temperature data presented in Chapter 3. Because the irradiance data can be used as such, the full dataset is utilized. However, to compare the characteristics of overpower events to the results of overirradiance events presented in Chapter 5, the results on days with consistent cloud shadow movement are also presented in parallel.

6.1.1 Occurrence of overpower events

Figure 42 presents the probability density distributions of the MPP power of the studied PV generator on full dataset and on the consistent days. Only the operating

points with MPP power over 5 percent of the STC power of the PV generator are included. The probability density plots have two distinct peaks: the first in the low power region due to early morning, late evening, and shade periods; and another at 0.75 p.u. due to the clear-sky periods near the peak production hours. The probability densities have some differences between the full dataset and the consistent days, which is because consistent days are mostly partly cloudy days with more than 25 recognized cloud shadows, whereas the full dataset also contains fully overcast and clear-sky days. The MPP power exceeds the nominal STC power only 0.49 percent of the time for the full dataset and 0.90 percent of the time for consistent days. With a DC-to-AC power ratio of 1.0, the system is operating in power-limiting mode only when the PV generator power exceeds the STC power. Power limiting occurs more frequently as the DC-AC power ratio is increased.

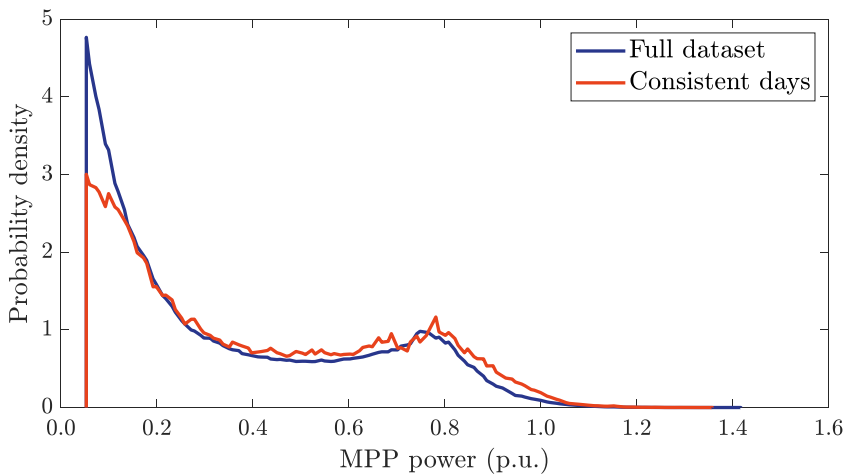


Figure 42. Probability density distribution of MPP power (relative to MPP power in STC) of the simulated 32 kW PV generator.

Figure 43 presents the number of overpower events observed in the simulated 32 kW PV generator as a function of MPP power on the full dataset of 745 days. The number of overpower events is also presented on consistent days to make it possible to directly compare the number of overpower events to the number of overirradiance events (Figure 38). During the full 745-day observation period, the MPP power exceeded the STC power 7750 times. The number of overpower events decreases quickly with increasing power limit; that is, MPP power exceeded 1.1 p.u. approximately 1000 times, 1.2 p.u. 100 times, 1.3 p.u. less than 10 times, and 1.4 p.u. only two times. Because the overpower events were counted by comparing the instantaneous power to a certain power limit, the MPP power can be considerably

higher during an overpower event than the power limit. Therefore, increasing the power limit slightly may increase the number of observed overpower events, because an overpower event that was previously counted as one can now be counted as two or more separate overpower events. This phenomenon is visible at MPP powers higher than 1.3 p.u. in Figure 43.

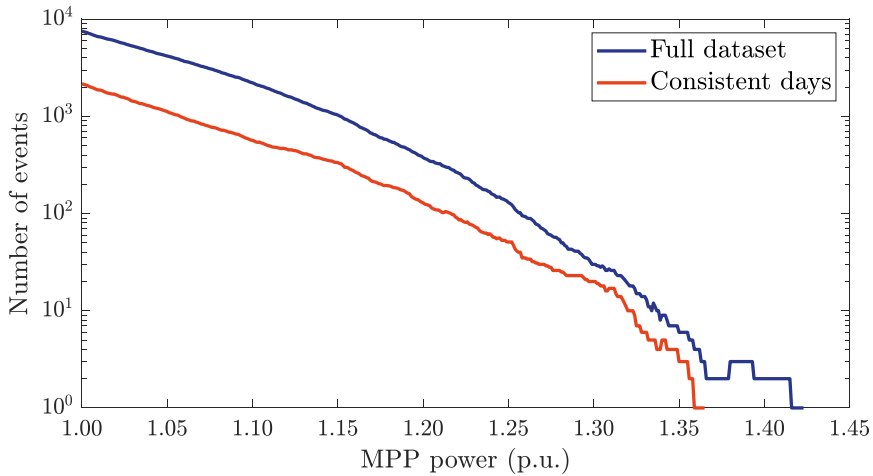


Figure 43. Number of overpower events in the simulated 32 kW PV generator as a function of MPP power.

6.1.2 Duration of overpower events

Figure 44 presents the maximum, mean, and median durations of overpower events on days with consistent cloud shadow movement and on the full dataset of 745 days. The maximum duration of the overpower events decreases quickly with increasing MPP power, whereas the mean and median duration of the overpower events decreases only slightly with increasing MPP power of the overpower event. The MPP power can occasionally exceed the nominal STC power for several minutes, but the average duration is from ten to twenty seconds slightly decreasing with increasing MPP power. The step-like behavior of the maximum duration curve is due to single events that define the maximum duration for a certain power range. The maximum overirradiance event duration curve had a similar shape due to same reasons (Section 5.2, Figure 35). Similar statistical analyses on the durations of overpower events have not been published before, but these results are in line with previously published

durations of overirradiance events (Järvelä et al., 2020; Lappalainen & Kleissl, 2020; Yordanov, Midtgård, et al., 2013).

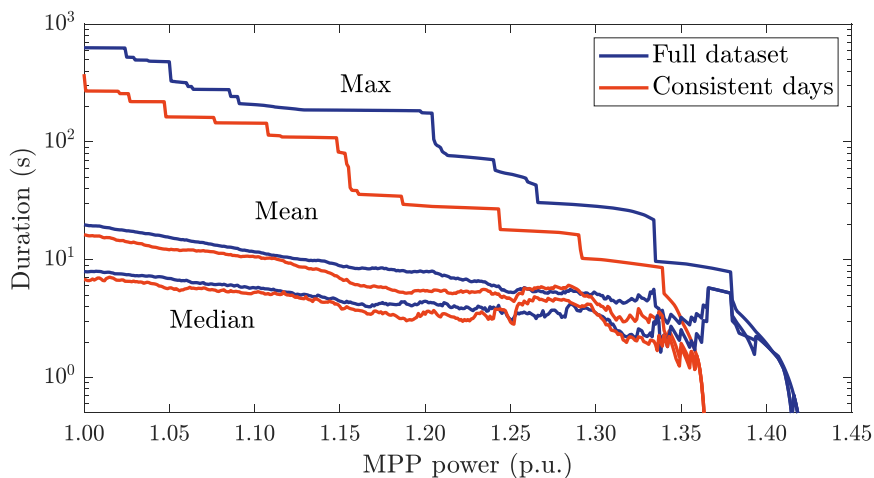


Figure 44. Maximum, mean, and median durations of overpower events exceeding the power value in the simulated 32 kW PV generator as a function of MPP power.

The maximum MPP power in the full dataset was 1.42 p.u. (and for comparison on consistent days 1.36 p.u.). Figure 45 presents the $I-U$ and $P-U$ curves of the studied PV generator when the MPP power was 1.42 p.u. During this moment the

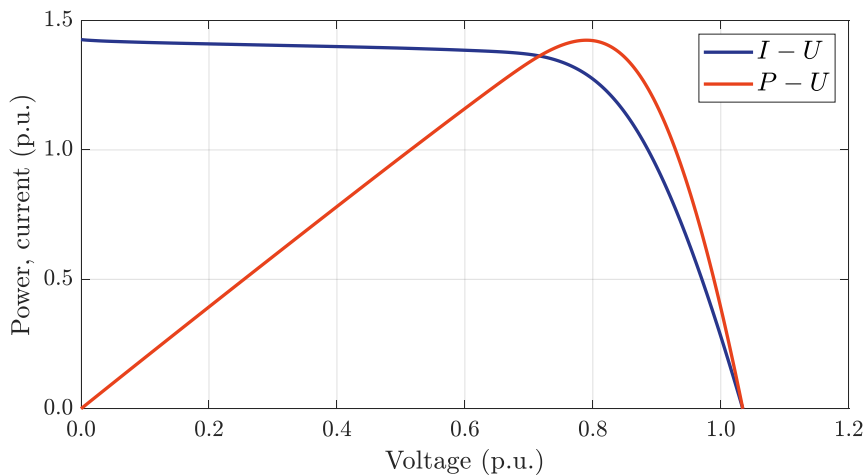


Figure 45. $I-U$ and $P-U$ curves (relative to short circuit current, open circuit voltage, and MPP power in STC) of the PV generator during the peak MPP power moment on the 9th of June 2016 at 11:45.

ambient temperature was 7.5 °C, the PV panel temperature was 21 °C so that the temperature rise of the PV panel was 13.5 °C. The average irradiance was approximately 1410 W/m², and it was reasonably uniform over the PV generator land area, which can also be seen from the clean shape of the $I-U$ curve. The open circuit voltage was 1.03 p.u., which is clearly over the nominal open circuit voltage in STC. However, when considering possible power limiting, the operating voltage can be observed to remain below 1.0 p.u. even with a DC-to-AC power ratio of 2.

6.1.3 Operating conditions during overpower events

To give a better understanding on operating conditions that cause extreme overpower events, Figure 46 presents the operation conditions of the PV modules during the full observation period of 745 days. Subfigure (a) presents the occurrence of irradiance versus the PV panel operating temperature and Subfigure (b) presents the occurrence of irradiance versus the difference between the PV panel operating temperature and the ambient temperature; that is, the temperature rise of the PV panel. The resolution for measured irradiance is 0.25 W/m² per pixel and for temperature 0.25 °C per pixel. The actual PV panel operating temperature frequently exceeds the STC temperature of 25 °C, even though the measurement site is in a moderately cool environment. The maximum PV panel operating temperature was 67.25 °C, and the maximum temperature rise was 47 °C. Typically, the PV panel operating temperature during clear-sky conditions and peak irradiance hours was 40–60 °C. During the peak production hours and clear-sky conditions, the operating temperature of the PV panel is typically 25–35 °C higher than the ambient temperature. In Subfigure (b), there is a clear correlation visible between the increase of the PV panel temperature with respect to irradiance. PV panel temperature increases, on average, by 1 °C as the irradiance increases by 30 W/m². However, high irradiance values can be observed when the PV panel temperature is low, and vice versa. This is due to the thermal mass of the PV panel, which is why the PV panel temperature does not immediately follow fast fluctuations in irradiance. Under typical stable diffuse irradiance of 200 W/m², the PV panel temperature is only 5–10 °C above the ambient temperature. Therefore, if an overirradiance event is preceded by a long shade period, the PV panel temperature may have dropped close to the ambient temperature and the sudden increase in irradiance does not immediately affect the PV panel temperature. This kind of occurrence will further increase the PV panel MPP power up to 10 percent on top of the effect of

overirradiance since the panel efficiency (voltage) increases with decreasing operating temperature. This will also occasionally increase the operating voltage of the solar inverter.

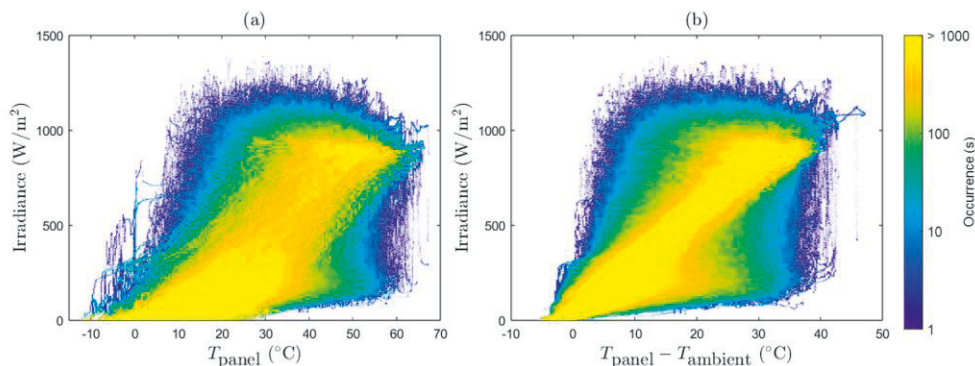


Figure 46. Occurrence of (a) irradiance and PV panel temperature T_{panel} , and (b) irradiance and the difference between T_{panel} and the ambient temperature T_{ambient} during the observation period of 745 days in one PV panel.

The operating conditions during overpower events are further analyzed in Figure 47, which presents the maximum, minimum, and 10 percent, 50 percent and 90 percent percentiles of the ambient air temperature, the PV panel operating temperature, and the temperature rise of the PV panel as a function of MPP power. The maximum ambient and PV panel temperatures, and especially their difference, have a decreasing trend with increasing MPP power, as is also the case for the 10 percent and 50 percent percentiles. The reason for this is that the PV panel efficiency increases with decreasing temperature of the PV panel caused by lower ambient temperature and less heating of the panel during shade periods before overirradiance events. In fact, the highest MPP powers occur when both the ambient temperature and the PV panel temperature rise are low; that is, after the shade periods on relatively cool partly cloudy days. This is because the cloud enhancement events have a practical upper limit for irradiance, but the PV panel temperature can vary over a wide range. Therefore, to reach high MPP power, it is essential that the PV panel operating temperature is close to its practical lower limit during shade periods.

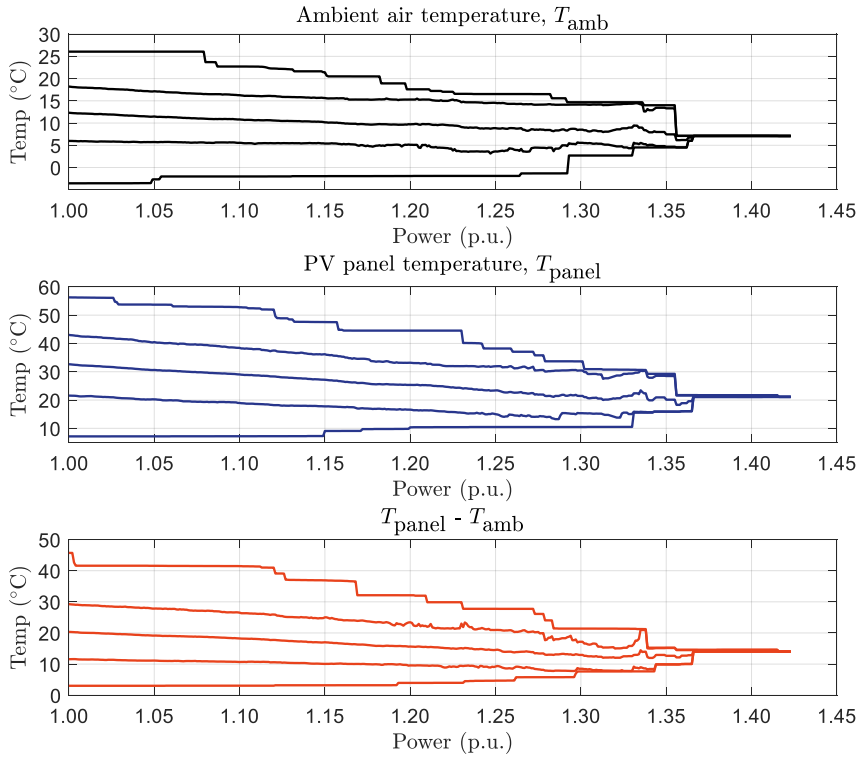


Figure 47. Maximum, minimum, and 10 percent, 50 percent and 90 percent percentiles of the ambient air temperature, PV panel temperature and the temperature difference between the PV panel and the ambient air during the overpower events as a function of PV generator power.

The dependence of the PV panel temperature on irradiance is exemplified in Figure 48, which presents the PV panel operating and ambient temperature, and irradiance during a 20-minute partly cloudy period on the 4th of June 2018. The ambient temperature varies only some degrees Celsius, but the PV panel operating temperature fluctuates due to changes in the irradiance. The PV panel temperature increases during the three distinct high irradiance periods and decreases during the shade periods. During high irradiance periods starting at 11:39 and 11:46, the PV panel temperature increases approximately 2 °C per minute, and during the shade periods starting at 11:43 and 11:48, the PV panel temperature decreases approximately 1 °C per minute. The 4 °C increase in PV panel temperature during the first overirradiance event translates to a decrease in efficiency (power) of about 2 percent.

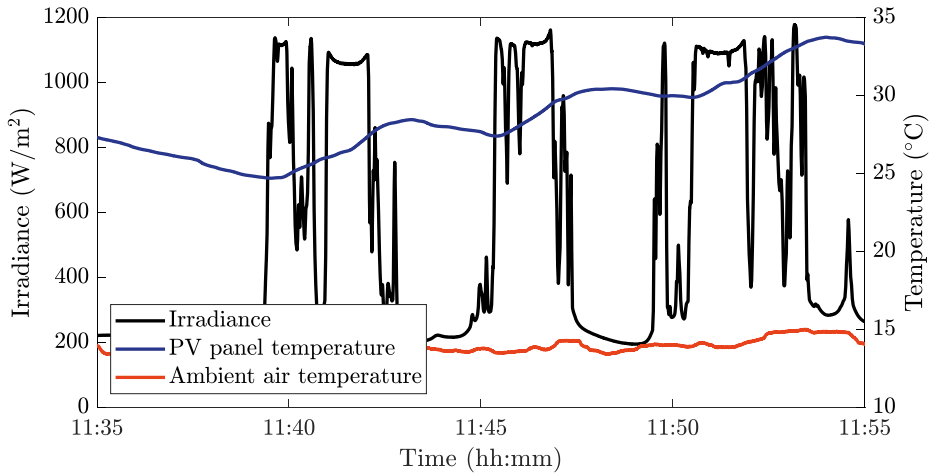


Figure 48. Ambient and PV panel temperature and irradiance on a partly cloudy period on the 4th of June 2018.

As discussed in Chapter 5, the number of overirradiance events depends on the size of the PV generator. Whereas the irradiance and duration of the events provides a relatively good understanding of the extent of the effects, the actual $P-U$ characteristics of a PV generator are affected by its configuration, and especially by the operating temperature of the PV panels. The irradiance can be used to estimate the short circuit current of the PV generator, but to accurately analyze the MPP power, the operating temperature of the PV panels should also be considered. The PV panel temperature fluctuates strongly as a function of irradiance, and the difference between shaded and non-shaded operating temperatures can be up to 30 °C, which translates to approximately 15% difference in the efficiency (power) of the PV panel.

6.2 Operation of the PV power plant during overpower events

Due to the trend of oversizing the PV generator, the solar inverter frequently operates against its power limit. The lost energy yield during overpower events is not that interesting, but power limiting can affect the operating voltage. This changes the loading profile and, consequently, the operational characteristics of the inverter. MPP and open circuit voltages are independent from the DC-to-AC power ratio, but the power limiting increases actual operating voltages of the PV generator. This section discusses the effects of the DC-to-AC power ratio on the operational

characteristics of the PV generator and PV power plants during the overpower events. The analysis is based on the same simulations as the previous section.

6.2.1 Typical MPP and open circuit voltages

Power limiting itself does not greatly affect the $I-U$ characteristics of a PV generator. There may be a small effect on operating temperature because the produced electric power is smaller (Torres-Lobera & Valkealahti, 2014). That is, if the configuration of the PV generator is fixed and only the power-limit is varied, the $I-U$ curve of the PV generator is pretty much the same than without power limitation, and in practice the open circuit voltage sets the upper limit for the operating voltage. To maximize the yield and efficiency of PV power plants, it may be beneficial to use different panel configurations for different DC-to-AC power ratios. However, for the sake of simplicity, such optimizations are not considered in this dissertation.

Figure 49 presents the probability densities of the open circuit and MPP voltages on the full 745-day observation period, and for the consistent days as reference. The voltage was normalized to the nominal open circuit STC voltage, and the analysis was limited to periods where the MPP power of the PV generator was more than 5 percent of the nominal STC power. For the full observation period, the mean MPP voltage was 0.741 p.u. and mean open circuit voltage was 0.918 p.u. (respectively 0.736 p.u. and 0.916 p.u. for consistent days). On average, MPP and open circuit

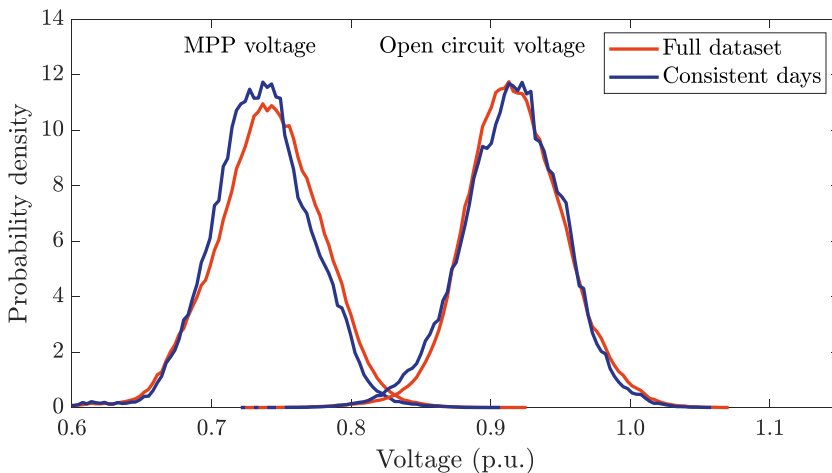


Figure 49. Probability density distributions of the MPP and open circuit voltages of the 32 kW PV generator during the observation periods.

voltages are less than the nominal MPP voltage of 0.782 p.u. and open circuit voltage of 1.0 p.u.. However, the maximum MPP voltage of 0.936 p.u. (0.916 p.u. for consistent days) and maximum open circuit voltage of 1.071 p.u. (1.058 p.u. for consistent days) were considerably higher than the nominal values. The mean and maximum MPP and open circuit voltages were approximately the same for the full dataset and the consistent days.

6.2.2 Power limiting and operating voltage

During the 745-day observation period, the MPP voltage never exceeded the nominal STC open circuit voltage. However, during overpower events, and especially with high DC-to-AC power ratios, the system rarely operates in the MPP so that the actual operating voltage is somewhere between the MPP and open circuit voltage. It can be observed from Figure 49 that the probability density distributions of the MPP and open circuit voltage have long tails on the right-hand side, which means that operating conditions causing high operating voltages occur, but only seldom. This requires both high irradiance and low PV panel temperature.

To exemplify how DC-to-AC power ratio affects the operating voltages of a residential size PV power system, Figure 50 presents the cumulative distributions of the operating voltage for different DC-to-AC power ratios when the MPP power was more than 5 percent of the nominal STC power. Due to power limiting, the

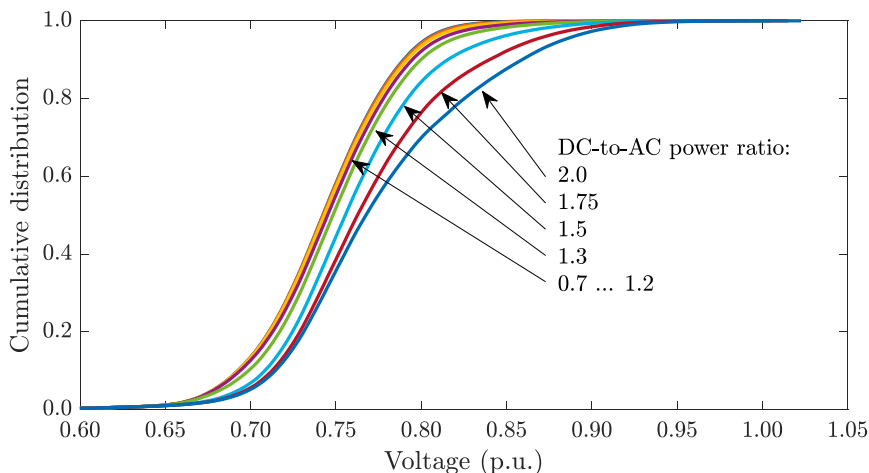


Figure 50. Cumulative distributions of the operating voltage of the 32 kW PV generator for DC-to-AC power ratios between 0.7 and 2.0 during the full observation period of 745 days.

operating voltage shifts to higher voltages with increasing DC-to-AC power ratio. Initially, increasing the DC-to-AC power ratio has only a small effect on operating voltage so that with DC-to-AC power ratios up to 1.3, there is a barely noticeable change. However, increasing the DC-to-AC power ratio further has a noticeable effect on the operating voltage, because power-limiting starts to occur also during normal operating hours; that is, when the irradiance is not enhanced, and the PV panel operating temperature is typical.

Figure 51 presents the high-end operating voltage percentiles of the 32 kW PV generator as a function of DC-to-AC power ratio during the full observation period. As observed in Figure 50, a small increase in the DC-to-AC power ratio has only a small effect on the average operating voltages, as can also be observed from the beginning of the 75% percentile curve. However, the maximum operating voltages increase faster in the beginning as the DC-to-AC power ratio increases. However, increasing the DC-to-AC power ratio further increases the maximum operating voltages only slightly. This can be observed for example from the 99.9% percentile curve. With a DC-to-AC power ratio of 1.0 the 99.9% percentile voltage is 0.87 p.u., and with 1.5 power ratio it is 0.94 p.u. Further increasing the power ratio to 2 increases the 99.9% percentile voltage to only 0.96 p.u. This is due to the $P-U$ curve shape — when operating near the open circuit voltage, a small increase in the operating voltage can drastically decrease the power.

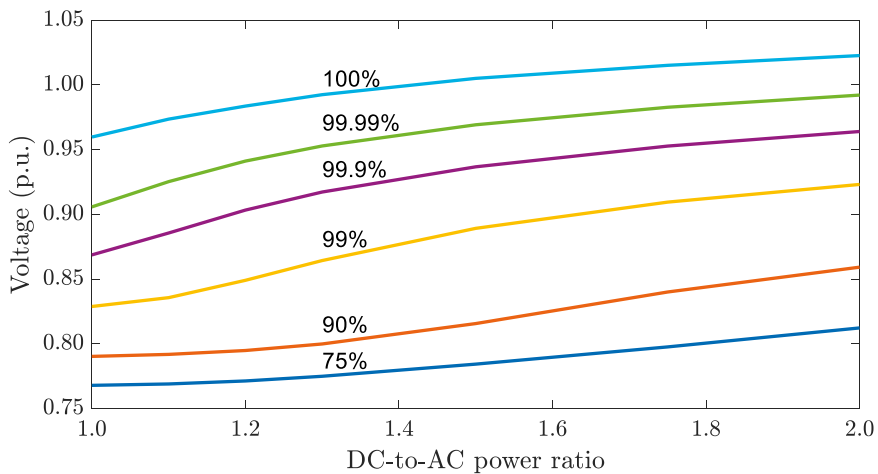


Figure 51. Operating voltage percentiles as a function of DC-to-AC power ratio of the 32 kW PV generator during the full observation period of 745 days.

Similar results on the operating voltage of a PV power plant have not been published before. The increase of operating voltage during overpower events has been exemplified, for example, in (Giesler et al., 2011) and (Macêdo & Zilles, 2007), but they did not present proper statistical analyses, so comparison of results is not possible. (Lappalainen & Kleissl, 2020) simulated the operation of 18 kW, 91 kW and 192 kW PV generators and they used the same PV panel model as in this dissertation. However, they assumed the PV panel temperature to be constant and limited the analyses only to overirradiance events. The assumption of a constant operating temperature is incorrect, distorting the results, and limiting the analyses only to overirradiance events neglects the effect of power limitation during clear-sky days when the DC-to-AC power ratio is high. Anyhow, from their results it can be observed that increasing the DC-to-AC power ratio first has a big effect on the operating voltage, but after a certain limit the effect on the upper end of operating voltages is only minimal, which is in line with the results presented in this dissertation.

6.2.3 Overvoltage events

Overpower events have relatively short duration, but with increasing DC-to-AC power ratio, the system is operating more frequently and for longer periods in power-limiting mode. To estimate the effect of overpower events on the loading of system components, the MPP power of the overpower events, per se, cannot be used. Instead, analyzing the operating voltage during overpower events would help to understand their effect on, for example, the operation of solar inverters and their components.

Figure 52 exemplifies the operation of the studied 32 kW PV power system during a series of overpower events by presenting operating voltage and power, and MPP power and voltage when the DC-to-AC power ratio is 1.3. Corresponding irradiance, and ambient and PV panel temperature data are presented in Figure 48. The powers and voltages are normalized to the nominal MPP power and open circuit voltage in STC. In this case, the MPP power clearly exceeds the maximum power of the inverter, and consequently, there is a clear increase in operating voltage. In general, the transition to power limiting mode has an immediate and noticeable effect on the operating voltage, because the $P-U$ curve is flat around the MPP; that is, a relatively large change in the operating voltage is required to change the operating power.

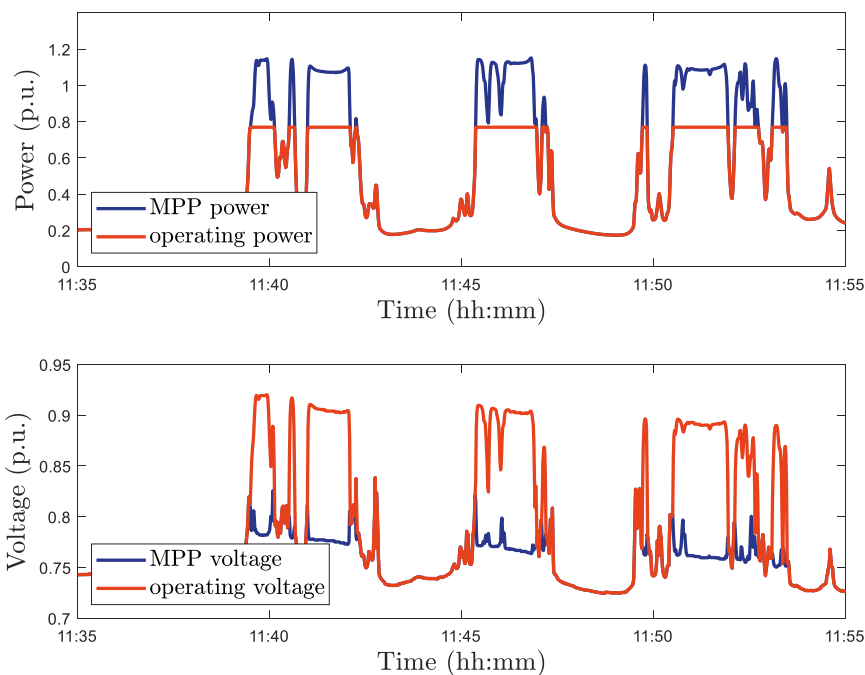


Figure 52. The power and voltage of the MPP and operating points of the 32 kW PV power plant with a DC-to-AC power ratio of 1.3 during a partly cloudy period on the 4th of June 2018.

The overvoltage events could be counted and categorized similarly as the overirradiance and overpower events, but considering the loading of system components, their analysis should be linked to overpower events. When comparing the MPP power and operating voltage at 11:46 in Figure 52, short dips in the power are also visible in the voltage. However, despite the short dips, the system is operating continuously in power limiting mode, so it would be misleading to count these as two or more separate events. Therefore, when analyzing overvoltage events, it is justified to categorize them by their average operating voltage. Obviously, with high DC-to-AC power ratios, the system can operate several hours in power limiting mode, but as presented in Figure 46, in the case of the highest operating voltages, PV panels must first have cooled down due to a long shade period.

Figure 53 presents the maximum, median, and mean duration of overpower events in the studied 32 kW PV generator as a function of average operating voltage of the event when the DC-to-AC power ratio is 1.0. With a low DC-to-AC power ratio, the PV generator power exceeds the inverter power only for short durations during the overpower events. Therefore, the maximum duration of overpower

events is 10 minutes with the average operating voltage varying between 0.72 and 0.87 p.u. The mean duration of overpower events is approximately 20 seconds and the median duration is approximately 10 seconds with the average operating voltage varying between 0.67 and 0.94 p.u. This is in line with the typical durations of overpower events presented in Figure 44 in Section 6.1.2.

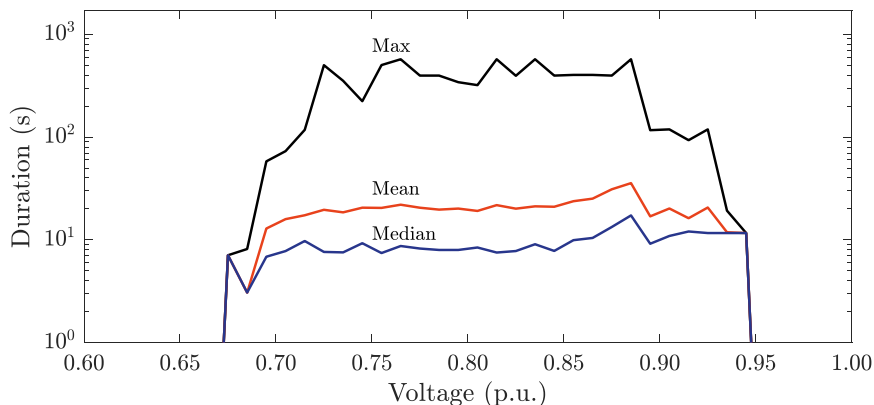


Figure 53. Maximum, mean, and median duration of overpower events in the 32 kW PV generator as a function of the average operating voltage during the event when the DC-to-AC power ratio of 1.0.

Increasing the DC-to-AC power ratio has a drastic effect on the maximum duration of overpower events because the system can now enter power-limiting mode during the peak production hours on clear-sky days, and therefore, the durations of overpower events can be several hours. This is exemplified in Figures 54 and 55, which present the maximum, mean, and median durations of overpower events as a function of average operating voltage during the event with DC-to-AC power ratios of 1.3 and 1.5, respectively. With the DC-to-AC power ratio of 1.3, the system was observed to operate continuously against its power limit up to four hours with the average operating voltage varying between 0.65 and 0.92 p.u., and with the DC-to-AC power ratio of 1.5 up to five hours with the average operating voltage varying between 0.65 and 0.93 p.u. For the same voltage range, mean and median durations of overpower events were considerably less — for a DC-to-AC power ratio of 1.3, the mean duration was approximately two minutes and median duration was 10 seconds, and for DC-to-AC power ratio of 1.5, the mean duration was approximately two minutes, and the median duration was approximately 15 seconds. With the DC-to-AC power ratio of 1.3, the duration of overpower events can be one minute when the average operating voltage is 0.96 p.u., and similarly with the

DC-to-AC power ratio of 1.5 the average operating voltage can be 0.98 p.u.; that is, close to the open circuit voltage in STC.

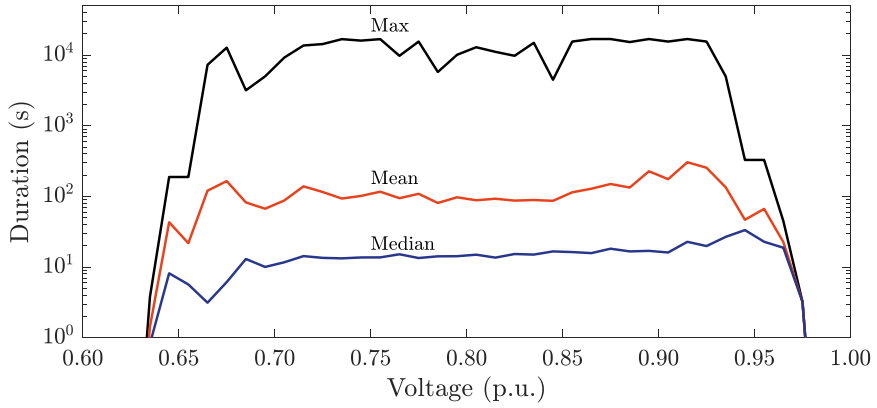


Figure 54. Maximum, mean, and median duration of overpower events in the 32 kW PV generator as a function of the average operating voltage during the event when the DC-to-AC power ratio is 1.3.

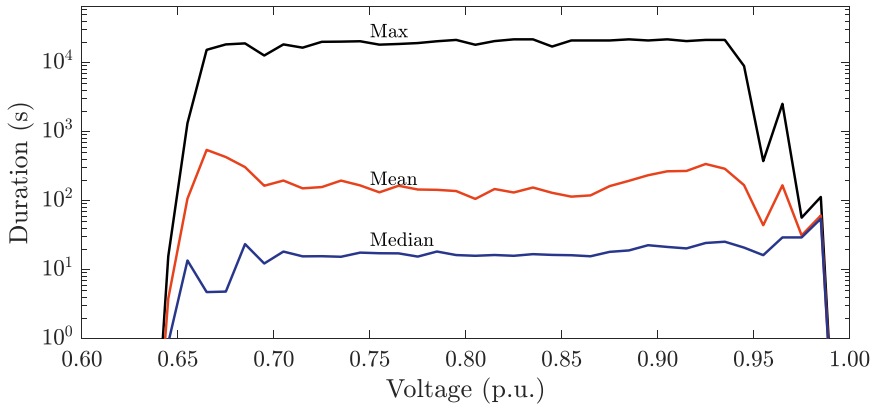


Figure 55. Maximum, mean, and median duration of overpower events in the 32 kW PV generator as a function of the average operating voltage during the event when the DC-to-AC power ratio of 1.5.

Figure 56 presents the number of overpower events as a function of the average operating voltage during the event for DC-to-AC power ratios of 1.0, 1.3, and 1.5. The total number of overpower events increases as the DC-to-AC power ratio increases. When comparing to durations of the overpower events presented in Figures 53, 54, and 55, it can be observed that the number of overpower events at high average operating voltages is low, but the number of these events increases with

increasing DC-to-AC power ratio. However, the peak of overpower events shifts to higher average operating voltages of more than 0.8 p.u. as the DC-to-AC power ratio increases, compared to about 0.75 p.u. under normal clear-sky irradiance conditions (Figure 42).

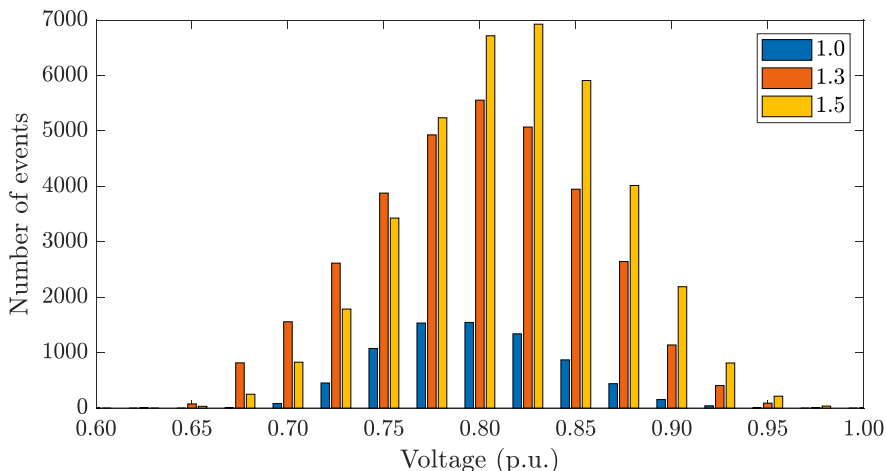


Figure 56. Number of overpower events in the 32 kW PV generator as a function of the average operating voltage during the event for DC-to-AC power ratios of 1.0, 1.3, and 1.5.

6.3 Possible effects on the operation of solar inverters

In Section 6.1, the maximum MPP power of the PV generator was found to exceed the nominal STC power frequently, and occasionally the MPP power can be 1.4 times the nominal STC power. However, when considering the operation of the solar inverter, MPP power during overpower events is not particularly relevant. The excess power of overpower events cannot be utilized because the inverter is operating in power-limiting mode; therefore, energy-loss analysis is hypothetical and irrelevant in practice. On the other hand, an increase in the operating voltage profile can affect the operation and expected lifetimes of certain power components, such as DC link capacitors and IGBTs.

Limits for the safe operating area of the inverter are typically determined based on temperature rise margins of different components and sections. Even though solar inverters are rated for some minimum and maximum ambient temperature; maximum DC-side current; and maximum DC-side voltage, it is not reasonable to

estimate their lifetimes by assuming that the inverter is constantly operating in its worst operating point. In practice, the maximum operating temperatures of different components are determined so that their design lifetimes can be achieved under expected operating conditions and loading profiles. The loading profile depends on expected irradiance conditions, ambient temperature, PV generator configuration, DC-to-AC power ratio, installation altitude, etc. When considering the extra loading caused by overpower events, interesting aspects are the duration and operating voltage during the most extreme overpower events.

Section 6.2 discusses the operation of PV generator during overpower events, and how the DC-to-AC power ratio affects the operating voltage profiles. MPP voltage was never observed to exceed the nominal STC open circuit voltage. However, when the MPP power exceeds the inverter power limit, actual operating voltage increases. In fact, when the DC-to-AC power ratio was 1.5 the operating voltage was observed to briefly exceed the nominal open circuit voltage in STC. Such high DC-to-AC power ratio PV power systems are economically feasible (Väisänen et al., 2019). Therefore, to avoid any unintended inverter shutdowns, the power plant should be designed so that the inverter can operate at full power when the operating voltage is close to the STC open circuit voltage. It is not enough to estimate the maximum operating voltage based on ambient temperature, clear-sky irradiance and expected temperature rise of the PV panels because the irradiance may increase due to the CE phenomenon and the temperature rise of the panels may be less than expected, further increasing the operating voltage.

In Section 6.2.3, the average operating voltages during overpower events were analyzed in more detail, and it was shown that with a typical DC-to-AC ratio of 1.3, the system can operate against its power limit for four hours when the average operating voltage is up to 0.92 p.u. (relative to open circuit voltage in STC). The duration of overpower events can be some minutes when the average operating voltage is 0.95 p.u., and 10 seconds when the average operating voltage is 0.97 p.u. Similarly, with a DC-to-AC power ratio of 1.5, the maximum duration of overpower events can be five hours when the average operating voltage is 0.93 p.u., some minutes when the operating voltage is 0.96 p.u., and 10 seconds when operating voltage is 0.98 p.u.. Due to oversizing of the PV generator, the inverters are operating against their power limits for several hours with reasonably high operating voltages. The operating voltage can be higher during extreme events, but the duration of these events is only a few minutes.

In Section 6.1.3, it was shown that the overpower events are often preceded by shade periods cooling the PV panel operating temperature close to the ambient

temperature. Due to the thermal mass, PV panels do not immediately heat up when the cloud shadow passes and overirradiance area covers it. Similarly, system components such as DC link capacitors and IGBTs have a thermal mass as well. When considering PV power systems with reasonable DC-to-AC power ratios, the inverter operates at partial power during the shade periods preceding the overpower events, and the operating temperatures of system components can cool down, thus withstanding better the additional stress that may be caused by extreme overpower events.

IGBTs have a small thermal mass so that they can heat up reasonably quickly. Typically, thermal time constants of IGBTs and their heat sinks in air-cooled systems range from around ten seconds to several hundreds of seconds (Infineon Technologies AG, 2015). Because the durations of the extreme overpower events with highest operating voltages can be some minutes, it can be assumed that IGBT temperatures can get close to their steady state values in corresponding operating points. However, when considering that the operating voltages during the extreme events were observed to be only slightly higher than they can be during clear-sky steady state conditions (0.95 p.u. vs. 0.92 p.u. with a DC-to-AC power ratio of 1.3), the switching losses (temperature rise) of the IGBTs can be estimated to be approximately 1% higher. Considering that these extreme events occur only rarely and for short moments, their overall effect and extra loading to the IGBTs can be estimated to be negligible.

Thermal time constant of DC link capacitors are considerably higher compared to IGBTs. Their operating temperature can cool down during the shade periods preceding the overirradiance events, and therefore, it is not unreasonable to assume that their operating temperature (temperature rise) does not reach the steady state temperature during the most extreme overpower events. The capacitor must be designed to withstand the long-term loading caused by the cold clear-sky days when the operating voltage is for several hours reasonably high. Therefore, the extra loading caused by the most extreme overpower events can be assumed to be negligible.

It must be noted that the operating temperature of IGBTs and capacitors depends on the ambient temperature and the temperature rise due to power losses. A relatively cool ambient temperature was found to be one prerequisite for the strongest overpower events. In commercial rooftop applications it is possible that the inverter is located indoors in a controlled climate so that the ambient air temperature can be estimated to be constant. In this case, there is no direct link between the ambient conditions of the PV generator and the inverter so that the

above analysis is valid. However, the situation changes slightly if the inverter is located outdoors next to the PV generator, as it often is. Then, the cooler ambient temperature increases the temperature rise margins of different system components, which can mitigate the effect of overpower events by increasing the power limit and, consequently, decreasing the operating voltage. However, the power rating of the inverter can vary as a function of ambient temperature so that the power limit is increased at lower ambient temperatures (ABB Oy, 2018). By increasing the power limit, the operating temperatures of different system components also increase so that they are operating closer to their maximum design values, which increases the overall loading of system components as they are operating closer to their design limits.

The results presented in section 6.2 are based on measurements in Nordic conditions. The irradiance can reach considerably higher values closer to the equator, which is seen as higher MPP power. This is especially the case if the power plant is at a high altitude where ambient temperature is typically lower. Because the characteristics of overirradiance events have been reported to be similar in other geographical locations (Lappalainen & Kleissl, 2020), the characteristics of overpower events can be estimated to be similar as well. Naturally, the loading of system components is higher in more favorable irradiance conditions, but this must anyhow be taken into consideration when assessing component lifetimes. Therefore, the extra loading due to the most extreme overpower events is only slightly increasing the overall loading of system components.

If the inverter and its components are designed properly, the overall effect of CE phenomenon seems to be negligible. However, it should be noted that these events occur, and lifetime analyses should be performed on a case-by-case basis. Loading profiles presented in Section 6.2.3 can be used to assess the lifetimes of critical system components in extreme conditions. Excess loading due to occasionally elevated operating voltage can negatively affect the lifetime of the inverter if operating conditions are already harsh due to, for example, high humidity and temperature; high concentration of salt or other corrosive substances in the air; or system components are reaching the end of their lifetimes, which can be seen, for example, as reduced capacitance and increased ESR losses of the capacitors.

7 CONCLUSION

This dissertation discusses CE phenomenon from the PV power generation point of view. It was known that overirradiance events can affect the operation of large utility-scale PV power plants, but the characteristics of the overirradiance and overpower events have not been thoroughly analyzed. The goal of this dissertation was to address this shortcoming by analyzing the occurrence of overirradiance events and their magnitude, spatial extent, and temporal duration, as well as how the overpower events affect the operation of PV power plants. The first part of this dissertation studied the relations between the diameter and irradiance of overirradiance areas; and analyzes the effect of the PV generator size on the occurrence, duration, and irradiance of the overirradiance events they experience. The second part of this dissertation studied the effects of overirradiance events on the operation of PV power plants by analyzing the occurrence, duration and MPP power of the overpower events and their effect on the operating voltage and system components when using different DC-to-AC power ratios.

The analyzes are based on high-resolution irradiance and PV panel temperature data from 23 late spring, summer, and early autumn months from the TAU PV power research power plant in Tampere Finland. The irradiance data was collected with a tight mesh of photodiode-based irradiance sensors, and the PV panel temperature data was measured with a thermocouple pressed tightly against the backside of the PV panel. The measurement data was used to create an estimate of the overirradiance area speeds by first determining the cloud shadow speeds and then finding days where the cloud shadow movement was consistent. This speed estimate was then used to deduce the irradiance profile of the overirradiance areas. The measured irradiance and PV panel temperature data was also used to simulate the operation of a large residential size PV generator. The simulation model of the PV generator was based on a typical polycrystalline PV panel. To ensure the general applicability of the results, the control algorithm of the inverter was assumed to be ideal.

This dissertation provided statistical analyses on the spatial extent of overirradiance events. The mean diameter of overirradiance areas was found to be some hundreds of meters, decreasing slightly with increasing irradiance. The

maximum diameter was some kilometers decreasing quickly with increasing irradiance. The strongest overirradiance areas were observed to have a diameter of the order of some tens of meters. The highest observed irradiance was 1400 W/m^2 , which is approximately 1.5 times the expected clear-sky irradiance on the measurement site.

This dissertation studied the relation between the PV generator size and the occurrence, duration, and irradiance of overirradiance events. It was observed that increasing the PV generator size reduces the occurrence of overirradiance events affecting them. Up to some tens of meters, the side length of the PV generator has only a small effect on the occurrence, but when it reaches some hundreds of meters, the occurrence clearly decreases. Because the diameter of the largest overirradiance areas can be considerably longer than the side length of any realistic PV generator, the size of the PV generator does not have a noticeable effect on the maximum duration of overirradiance events. Counter-intuitively, the mean and median durations of the overirradiance events are the longer the larger the PV generator is. This is due to the spatial smoothing of irradiance and the fact that most overirradiance areas have a diameter of some tens of meters, so their effect on large PV power plants is not noticeable.

During typical operating hours, the power of a large residential PV generator was found to exceed its nominal STC power 0.46 percent of the time. The occurrence of the overpower events decreased quickly with increasing MPP power. The maximum duration of overpower events was some minutes for events exceeding 1.0 p.u. (relative to nominal MPP power in STC), and some tens of seconds for events exceeding 1.3 p.u. The mean duration of overpower events was approximately 10 seconds, and the median duration was a few seconds, decreasing slightly with increasing MPP power. The maximum power was 1.42 p.u. when irradiance was about 1400 W/m^2 , and the PV panel temperature was low. Extreme overpower events occurred when the temperature rise of the PV panel was relatively small. During peak irradiance hours and clear-sky conditions, the temperature rise of PV panels was typically 25 to 35 °C, but during the strongest overpower events it was only about 15 °C. This is because the cooling of PV panels during shaded periods increased their voltage and efficiency. That is, this dissertation showed that the shade periods preceding the overirradiance events were found to be a prerequisite for the strongest overpower events.

This dissertation analyzed the loading profile of PV power systems during overpower events, and it was shown that the operating voltage increases during the overpower events. The maximum MPP voltage was found to be 0.92 p.u. (relative

to nominal open circuit voltage in STC), but the actual operating voltage can be higher due to power limiting, which is typically done by increasing the operating voltage of the PV generator. Therefore, the operating voltage increases with increasing DC-to-AC power ratio. With low DC-to-AC power ratios, the maximum operating voltage increases significantly as the power ratio increases, but further increase of the ratio has a less effect on it. This is because the $P-U$ curve is quite flat around the MPP voltage, but much steeper closer to the open circuit voltage, where a small change in voltage has a large effect on power. The operating voltages of the most extreme overpower events were noticed to be only slightly higher than the operating voltages of the cold clear-sky days. With a DC-to-AC power ratio of 1.3, the operating voltage can be up to 0.92 p.u. for four hours when the inverter is operating continuously in power-limiting mode, and during the most extreme overpower events, the operating voltage was 0.96 p.u., which is not that much higher considering that the maximum duration of these events is only a few minutes. Increasing the DC-to-AC power ratio increases the operating voltage of the most extreme overpower events, but it also increases the operating voltage during the cold clear-sky days.

This dissertation studied the effect of CE phenomenon on various system components by analyzing how the extreme overpower events affect their operation and loading profile. The loading profile was then compared to normal but otherwise extreme operating conditions without irradiance enhancement. Assuming that the system components are selected according to proper design guidelines, the overall effect of CE phenomenon on them was found to be almost negligible. During normal operation, the overirradiance events cannot increase the PV generator current to the levels that would cause nuisance fuse operations. When following the design guidelines, the durations of the strongest recorded overirradiance events must be of the order of 1000 seconds for them to operate, which was found not to be the case. When considering the effect on the power components of the inverter, the operating voltage during the most extreme overpower events was found to be only slightly higher than during the normal operating hours of worst-case clear-sky days. Because of the elevated operating voltage, the switching losses of IGBTs can be estimated to be only slightly higher than during normal operating hours. In addition, the most extreme overpower events are preceded by shade periods, so the operating temperatures of the system components can cool down because the inverter is operating at partial power. Therefore, the operating temperature of DC link capacitors cannot reach their steady-state operating temperatures during the most extreme overpower events, because the thermal time constant is relatively high.

Because the most extreme overpower events are rare and their duration is only a few minutes, their effect on IGBTs and DC link capacitors can be estimated to be negligible. In brief, this dissertation showed that the speculations that overirradiance events would negatively affect the lifetimes and operation of system components were mostly found to be unfounded.

Regarding future research topics:

- The results presented in this dissertation were based on measurements performed in Nordic conditions. It would be interesting to replicate the research in different geographical locations.
- The results presented in this dissertation were based on irradiance sensors in fixed 45° tilt angle facing 23° east from due south. It would be interesting to perform a similar study with a 1- or 2-axis sun path tracking device.
- The irradiance data that were used in this dissertation came from a relatively small land area. It would be interesting to verify the results with irradiance data from an array of irradiance sensors spread on a considerably larger land area, corresponding to land areas of more than 5 MW PV generators.

BIBLIOGRAPHY

- ABB Oy. (2018). *PVS800-57B Central Inverters Hardware Manual*.
https://www.fimer.com/sites/default/files/EN_PVS800-57B_HW_C_A4.pdf
- Albertsen, A. (2010). *Electrolytic Capacitor Lifetime Estimation* (pp. 1–16). Jianghai Europe Electronic Components GmbH. www.jianghai-europe.com
- Becquerel, A.-E. (1839). Mémoire sur les effets électriques produits sous l'influence des rayons solaires. *Comptes Rendus*, *9*, 561–567.
- Blanc, P., Espinar, B., Geuder, N., Gueymard, C., Meyer, R., Pitz-Paal, R., Reinhardt, B., Renné, D., Sengupta, M., Wald, L., & Wilbert, S. (2014). Direct normal irradiance related definitions and applications: The circumsolar issue. *Solar Energy*, *110*, 561–577.
<https://doi.org/10.1016/j.solener.2014.10.001>
- Brecl, K., & Topič, M. (2011). Self-shading losses of fixed free-standing PV arrays. *Renewable Energy*, *36*(11), 3211–3216.
<https://doi.org/10.1016/j.renene.2011.03.011>
- Calcabrini, A., Weegink, R., Manganiello, P., Zeman, M., & Isabella, O. (2021). Simulation study of the electrical yield of various PV module topologies in partially shaded urban scenarios. *Solar Energy*, *225*(August), 726–733.
<https://doi.org/10.1016/j.solener.2021.07.061>
- Chen, S., Li, P., Brady, D., & Lehman, B. (2013). Determining the optimum grid-connected photovoltaic inverter size. *Solar Energy*, *87*(1), 96–116.
<https://doi.org/10.1016/j.solener.2012.09.012>
- de Andrade, R. C., & Tiba, C. (2016). Extreme global solar irradiance due to cloud enhancement in northeastern Brazil. *Renewable Energy*, *86*, 1433–1441.
<https://doi.org/10.1016/j.renene.2015.09.012>
- de la Parra, I., Marcos, J., García, M., & Marroyo, L. (2015). Control strategies to use the minimum energy storage requirement for PV power ramp-rate control. *Solar Energy*, *111*, 332–343.
<https://doi.org/10.1016/j.solener.2014.10.038>
- do Nascimento, L. R., de Souza Viana, T., Campos, R. A., & Rüther, R. (2019). Extreme solar overirradiance events: Occurrence and impacts on utility-scale photovoltaic power plants in Brazil. *Solar Energy*, *186*(April), 370–381.
<https://doi.org/10.1016/j.solener.2019.05.008>

- Dogga, R., & Pathak, M. K. (2019). Recent trends in solar PV inverter topologies. *Solar Energy*, 183(February), 57–73. <https://doi.org/10.1016/j.solener.2019.02.065>
- Eaton. (2021). Complete and reliable solar circuit protection. In *Eaton Product Catalogue*. <https://www.eaton.com/content/dam/eaton/products/electrical-circuit-protection/bussmann-iec-high-speed-semi-conductors-fuses/bussmann-iec-photovoltaic-high-speed-fuses/eaton-bussmann-series-photovoltaic-fuses-catalogue-ca135004en.pdf>
- Einstein, A. (1905). Über einen die Erzeugung und Verwandlung des Lichtes betreffenden heuristischen Gesichtspunkt. *Annalen Der Physik*, 322(6), 132–148. <https://doi.org/10.1002/andp.19053220607>
- Emck, P., & Richter, M. (2008). An Upper Threshold of Enhanced Global Shortwave Irradiance in the Troposphere Derived from Field Measurements in Tropical Mountains. *Journal of Applied Meteorology and Climatology*, 47(11), 2828–2845. <https://doi.org/10.1175/2008JAMC1861.1>
- Espinosa-Gavira, M. J., Agüera-Pérez, A., de la Rosa, J. J. G., Palomares-Salas, J. C., & Sierra-Fernández, J. M. (2018). An on-line low-cost irradiance monitoring network with sub-second sampling adapted to small-scale PV systems. *Sensors*, 18(10), 1–12. <https://doi.org/10.3390/s18103405>
- Gandhi, O., Kumar, D. S., Rodríguez-Gallegos, C. D., & Srinivasan, D. (2020). Review of power system impacts at high PV penetration Part I: Factors limiting PV penetration. *Solar Energy*, 210(June), 181–201. <https://doi.org/10.1016/j.solener.2020.06.097>
- Giesler, B., Czakalla, M., Zehner, M., Wirth, G., Wizemann, I., Maletz, K., Bothner, M., Becker, G., Betts, T. R., Gottschalg, R., Vollweiter, T., Bäuml, T., & Kumerle, G. (2011). Operating Data Analysis of Various Subsystems at the 20 MW PV Power Plant Rothenburg. *26th European Photovoltaic Solar Energy Conference and Exhibition*, 1, 4245–4250. <https://doi.org/10.4229/26thEUPVSEC2011-5BV.2.14>
- Gimon, B. Y. E., Myers, A., Special, W., From, A., Gosnell, C., Cooperative, A. T. C., & Paliwal, U. (2021). *Coal Cost Crossover 2. 0*.
- Gray, J. L. (2011). The Physics of the Solar Cell. In *Handbook of Photovoltaic Science and Engineering*. <https://doi.org/10.1002/9780470974704.ch3>
- Green, M. A., Dunlop, E. D., Hohl-Ebinger, J., Yoshita, M., Kopidakis, N., & Hao, X. (2022). Solar cell efficiency tables (version 59). *Progress in*

Photovoltaics: Research and Applications, 30(1), 3–12.
<https://doi.org/10.1002/pip.3506>

- Guerrero-Lemus, R., Vega, R., Kim, T., Kimm, A., & Shephard, L. E. (2016). Bifacial solar photovoltaics – A technology review. *Renewable and Sustainable Energy Reviews*, 60, 1533–1549. <https://doi.org/10.1016/j.rser.2016.03.041>
- Gueymard, C. A. (2017a). Cloud and albedo enhancement impacts on solar irradiance using high-frequency measurements from thermopile and photodiode radiometers. Part 1: Impacts on global horizontal irradiance. *Solar Energy*, 153, 755–765. <https://doi.org/10.1016/j.solener.2017.05.004>
- Gueymard, C. A. (2017b). Cloud and albedo enhancement impacts on solar irradiance using high-frequency measurements from thermopile and photodiode radiometers. Part 2: Performance of separation and transposition models for global tilted irradiance. *Solar Energy*, 153, 766–779. <https://doi.org/10.1016/j.solener.2017.04.068>
- Gueymard, C. A. (2018a). A reevaluation of the solar constant based on a 42-year total solar irradiance time series and a reconciliation of spaceborne observations. *Solar Energy*, 168(March), 2–9. <https://doi.org/10.1016/j.solener.2018.04.001>
- Gueymard, C. A. (2018b). Revised composite extraterrestrial spectrum based on recent solar irradiance observations. *Solar Energy*, 169(March), 434–440. <https://doi.org/10.1016/j.solener.2018.04.067>
- Hayek, A. El, Venet, P., Mitova, R., Wang, M., & Sari, A. (2019). Aging laws of electrolytic capacitors. *Evolution of Functional Performance and Expected Lifetime of Electrical Equipments (ELTEE)*, March 2019, 16–17.
- IEC. (2010). *ISO 60269-6 Low-voltage fuses – Part 6: Supplementary requirements for fuse-links for the protection of solar photovoltaic energy systems*.
- Infineon Technologies AG. (2015). Transient Thermal Measurements and thermal equivalent circuit models. In *AN 2015-10* (pp. 1–13). Infineon.
- Inman, R. H., Chu, Y., & Coimbra, C. F. M. (2016). Cloud enhancement of global horizontal irradiance in California and Hawaii. *Solar Energy*, 130, 128–138. <https://doi.org/10.1016/j.solener.2016.02.011>
- International Energy Agency. (2020). *World Energy Outlook 2020*. https://www.oecd-ilibrary.org/energy/world-energy-outlook-2020_557a761b-en
- Jäger-Waldau, A. (2019). *PV Status Report 2019*. <https://doi.org/10.2760/326629>

- Järvelä, M., Lappalainen, K., & Valkealahti, S. (2020). Characteristics of the cloud enhancement phenomenon and PV power plants. *Solar Energy*, *196*, 137–145. <https://doi.org/10.1016/j.solener.2019.11.090>
- Järvelä, M., Lappalainen, K., & Valkealahti, S. (2018). Cloud Enhancement Phenomenon and Its Effect on PV Generators. *35th European Photovoltaic Solar Energy Conference and Exhibition, September 2018*, 1964–1968. <https://doi.org/10.4229/35thEUPVSEC20182018-6CV.2.30>
- Järvelä, M., & Valkealahti, S. (2020). Operation of a PV power plant during overpower events caused by the cloud enhancement phenomenon. *Energies*, *13*(9). <https://doi.org/10.3390/en13092185>
- Järvelä, M., & Valkealahti, S. (2019). Power Curtailment and PV Panel Operating Voltage. *36th European Photovoltaic Solar Energy Conference and Exhibition*, 1549–1553. <https://doi.org/10.4229/EUPVSEC20192019-5CV.4.1>
- Kasten, F., & Young, A. T. (1989). Revised optical air mass tables and approximation formula. *Applied Optics*, *28*(22), 4735. <https://doi.org/10.1364/AO.28.004735>
- Koehl, M., Heck, M., Wiesmeier, S., & Wirth, J. (2011). Modeling of the nominal operating cell temperature based on outdoor weathering. *Solar Energy Materials and Solar Cells*, *95*(7), 1638–1646. <https://doi.org/10.1016/j.solmat.2011.01.020>
- Kuhnel, C., Schlegel, S., & Grossmann, S. (2017). Investigations on the long-term behavior and switching function of fuse-elements for NH-fuse-links (gG) at higher thermal stress. *2017 6th International Youth Conference on Energy (IYCE)*, 1–8. <https://doi.org/10.1109/IYCE.2017.8003691>
- Lappalainen, K., & Kleissl, J. (2020). Analysis of the cloud enhancement phenomenon and its effects on photovoltaic generators based on cloud speed sensor measurements. *Journal of Renewable and Sustainable Energy*, *12*(4). <https://doi.org/10.1063/5.0007550>
- Lappalainen, K., & Valkealahti, S. (2016a). Analysis of shading periods caused by moving clouds. *Solar Energy*, *135*, 188–196. <https://doi.org/10.1016/j.solener.2016.05.050>
- Lappalainen, K., & Valkealahti, S. (2016b). Apparent velocity of shadow edges caused by moving clouds. *Solar Energy*, *138*, 47–52. <https://doi.org/10.1016/j.solener.2016.09.008>
- Lappalainen, K., & Valkealahti, S. (2017a). Effects of PV array layout, electrical configuration and geographic orientation on mismatch losses caused by

- moving clouds. *Solar Energy*, 144, 548–555.
<https://doi.org/10.1016/j.solener.2017.01.066>
- Lappalainen, K., & Valkealahti, S. (2020). Number of maximum power points in photovoltaic arrays during partial shading events by clouds. *Renewable Energy*, 152, 812–822. <https://doi.org/10.1016/j.renene.2020.01.119>
- Lappalainen, K., & Valkealahti, S. (2015). Recognition of Shading Events Caused by Moving Clouds and Determination of Shadow Velocity from Solar Radiation Measurements. *31st European Photovoltaic Solar Energy Conference and Exhibition*, 1568–1573. <https://doi.org/10.4229/EUPVSEC20152015-5AO.7.5>
- Lappalainen, K., & Valkealahti, S. (2017b). Simulation Resolution of PV System Partial Shading Studies. *33rd European Photovoltaic Solar Energy Conference and Exhibition, February 2018*. <https://doi.org/10.4229/EUPVSEC20172017-6CO.13.6>
- Lappalainen, K., & Valkealahti, S. (2018). Size of a Basic Simulation Unit in Pv System Partial Shading Studies. *35th European Photovoltaic Solar Energy Conference and Exhibition, November*, 1647–1651. <https://doi.org/10.4229/35thEUPVSEC20182018-6CO.4.2>
- Luoma, J., Kleissl, J., & Murray, K. (2012). Optimal inverter sizing considering cloud enhancement. *Solar Energy*, 86(1), 421–429. <https://doi.org/10.1016/j.solener.2011.10.012>
- Macêdo, W. N., & Zilles, R. (2007). Operational results of grid-connected photovoltaic system with different inverter's sizing factors (ISF). *Progress in Photovoltaics: Research and Applications*, 15(4), 337–352. <https://doi.org/10.1002/pip.740>
- Marcos, J., Storkel, O., Marroyo, L., Garcia, M., & Lorenzo, E. (2014). Storage requirements for PV power ramp-rate control. *Solar Energy*, 99, 28–35. <https://doi.org/10.1016/j.solener.2013.10.037>
- Marcos, Javier, Marroyo, L., Lorenzo, E., Alvira, D., & Izco, E. (2011). Power output fluctuations in large scale pv plants: One year observations with one second resolution and a derived analytic model. *Progress in Photovoltaics: Research and Applications*, 19(2), 218–227. <https://doi.org/10.1002/pip.1016>
- Miao, Y., Lei, W., Li, S., Lv, X., Li, B., Wang, P., Xu, J., & Li, H. (2018). Influence of inverter DC voltage on the reliability of IGBT. *AIP Conference Proceedings*, 1967(May), 020023. <https://doi.org/10.1063/1.5038995>
- Motahhir, S., El Hammoumi, A., & El Ghzizal, A. (2020). The most used MPPT

- algorithms: Review and the suitable low-cost embedded board for each algorithm. *Journal of Cleaner Production*, 246, 118983. <https://doi.org/10.1016/j.jclepro.2019.118983>
- Nicolai, U. (2014). Determining Switching Losses of SEMIKRON IGBT Modules. In *Application Note AN1403* (pp. 1–15).
- Norris, D. J. (1968). Correlation of solar radiation with clouds. *Solar Energy*, 12, 107–112. [https://doi.org/10.1016/0038-092X\(68\)90029-7](https://doi.org/10.1016/0038-092X(68)90029-7)
- Ong, S., Campbell, C., Denholm, P., Margolis, R., & Heath, G. (2013). *Land-Use Requirements for Solar Power Plants in the United States* (Issue June). <https://doi.org/10.2172/1086349>
- Paasch, K. M., Nymand, M., & Kjaer, S. B. (2014). Simulation of the impact of moving clouds on large scale PV-plants. *2014 IEEE 40th Photovoltaic Specialist Conference, PVSC 2014*, 791–796. <https://doi.org/10.1109/PVSC.2014.6925036>
- Paasch, K. M., Nymand, M., & Kjar, S. B. (2015). Long term energy yield measurements of a string- vs. central inverter concept tested on a large scale PV-plant. *2015 17th European Conference on Power Electronics and Applications, EPE-ECCE Europe 2015*. <https://doi.org/10.1109/EPE.2015.7311679>
- Pecenak, Z. K., Mejia, F. A., Kurtz, B., Evan, A., & Kleissl, J. (2016). Simulating irradiance enhancement dependence on cloud optical depth and solar zenith angle. *Solar Energy*, 136, 675–681. <https://doi.org/10.1016/j.solener.2016.07.045>
- REN21. (2021). *Renewables 2021 Global Status Report*. Secretariat, REN21. <https://www.ren21.net/>
- Riordan, C., & Hulstron, R. (1990). What is an air mass 1.5 spectrum? (solar cell performance calculations). *IEEE Conference on Photovoltaic Specialists*, 1085–1088. <https://doi.org/10.1109/PVSC.1990.111784>
- Ruiz-Arias, J. A. (2021). Aerosol transmittance for clear-sky solar irradiance models: Review and validation of an accurate universal parameterization. *Renewable and Sustainable Energy Reviews*, 145(February), 111061. <https://doi.org/10.1016/j.rser.2021.111061>
- Sampath Kumar, D., Gandhi, O., Rodríguez-Gallegos, C. D., & Srinivasan, D. (2020). Review of power system impacts at high PV penetration Part II: Potential solutions and the way forward. *Solar Energy*, 210(February), 202–221. <https://doi.org/10.1016/j.solener.2020.08.047>

- Sera, D., Teodorescu, R., & Rodriguez, P. (2007). PV panel model based on datasheet values. *2007 IEEE International Symposium on Industrial Electronics*, 4, 2392–2396. <https://doi.org/10.1109/ISIE.2007.4374981>
- Shockley, W. (1949). The Theory of p-n Junctions in Semiconductors and p-n Junction Transistors. *Bell System Technical Journal*, 28(3), 435–489. <https://doi.org/10.1002/j.1538-7305.1949.tb03645.x>
- Skoplaki, E., & Palyvos, J. A. (2009). Operating temperature of photovoltaic modules: A survey of pertinent correlations. *Renewable Energy*, 34(1), 23–29. <https://doi.org/10.1016/j.renene.2008.04.009>
- Spataru, S., Sera, D., Blaabjerg, F., Mathe, L., & Kerekes, T. (2013). Firefighter safety for PV systems: Overview of future requirements and protection systems. *2013 IEEE Energy Conversion Congress and Exposition, ECCE 2013*, 4468–4475. <https://doi.org/10.1109/ECCE.2013.6647298>
- Starke, A. R., Lemos, L. F. L., Boland, J., Cardemil, J. M., & Colle, S. (2018). Resolution of the cloud enhancement problem for one-minute diffuse radiation prediction. *Renewable Energy*, 125, 472–484. <https://doi.org/10.1016/j.renene.2018.02.107>
- Stoffel, T. (2013). Terms and Definitions. In *Solar Energy Forecasting and Resource Assessment* (pp. 1–19). Elsevier. <https://doi.org/10.1016/B978-0-12-397177-7.00001-2>
- Sungrow. (2020). *SG5000UD/SG5000UD-20 datasheet*. Sungrow. https://en.sungrowpower.com/upload/documentFile/DS_SG5000UD_SG5000UD-20_Datasheet_V1.2.2_EN.pdf.pdf
- Tang, T., Gan, C., Hu, Z., Niu, H., Si, J., & Luo, X. (2017). A Quantitative Comparison Between Double Glass Photovoltaic Modules Using Half-Size Cells and Quarter-Size Cells. *IEEE Journal of Photovoltaics*, 7(5), 1298–1303. <https://doi.org/10.1109/JPHOTOV.2017.2730358>
- Tapakis, R., & Charalambides, A. G. (2014). Enhanced values of global irradiance due to the presence of clouds in Eastern Mediterranean. *Renewable Energy*, 62, 459–467. <https://doi.org/10.1016/j.renene.2013.08.001>
- Taylor, G. I. (1938). The Spectrum of Turbulence. *Proceedings of the Royal Society of London. Series A - Mathematical and Physical Sciences*, 164(919), 476–490. <https://doi.org/10.1098/rspa.1938.0032>
- Toreti Scarabelot, L., Arns Rampinelli, G., & Rambo, C. R. (2021). Overirradiance effect on the electrical performance of photovoltaic systems of different inverter sizing factors. *Solar Energy*, 225(April), 561–568.

<https://doi.org/10.1016/j.solener.2021.07.055>

- Torki, J., Joubert, C., & Sari, A. (2023). Electrolytic capacitor: Properties and operation. *Journal of Energy Storage*, 58(July 2022), 106330. <https://doi.org/10.1016/j.est.2022.106330>
- Torres-Lobera, D., & Valkealahti, S. (2014). Inclusive dynamic thermal and electric simulation model of solar PV systems under varying atmospheric conditions. *Solar Energy*, 105, 632–647. <https://doi.org/10.1016/j.solener.2014.04.018>
- Torres Lobera, D., Mäki, A., Huusari, J., Lappalainen, K., Suntio, T., & Valkealahti, S. (2013). Operation of TUT Solar PV Power Station Research Plant under Partial Shading Caused by Snow and Buildings. *International Journal of Photoenergy*, 2013, 1–13. <https://doi.org/10.1155/2013/837310>
- Väisänen, J., Kosonen, A., Ahola, J., Sallinen, T., & Hannula, T. (2019). Optimal sizing ratio of a solar PV inverter for minimizing the levelized cost of electricity in Finnish irradiation conditions. *Solar Energy*, 185(January), 350–362. <https://doi.org/10.1016/j.solener.2019.04.064>
- Villalva, M. G., Gazoli, J. R., & Filho, E. R. (2009). Comprehensive Approach to Modeling and Simulation of Photovoltaic Arrays. *IEEE Transactions on Power Electronics*, 24(5), 1198–1208. <https://doi.org/10.1109/TPEL.2009.2013862>
- Vishay. (2022). *MKP1848 DC-Link Roederstein Metallized Polypropylene Film Capacitors datasheet*. <https://www.vishay.com/docs/26015/mkp1848cdclink.pdf>
- Weigl, T., Nagl, L., Weizenbeck, J., Zehner, M., Augel, M., Öchsner, P., Giesler, B., Becker, G., Mayer, O., Betts, T., & Gottschalg, R. (2012). Modelling and Validation of Spatial Irradiance Characteristics for Localised Irradiance Fluctuations and Enhancements. *27th European Photovoltaic Solar Energy Conference and Exhibition*, 3801–3804. <https://doi.org/10.4229/27thEUPVSEC2012-5CO.7.6>
- Yan, C., Qu, M., Chen, Y., & Feng, M. (2020). Snow removal method for self-heating of photovoltaic panels and its feasibility study. *Solar Energy*, 206(April 2019), 374–380. <https://doi.org/10.1016/j.solener.2020.04.064>
- Yordanov, G. H. (2015). A study of extreme overirradiance events for solar energy applications using NASA's I3RC Monte Carlo radiative transfer model. *Solar Energy*, 122, 954–965. <https://doi.org/10.1016/j.solener.2015.10.014>

- Yordanov, G. H., Midtgård, O.-M., Saetre, T. O., Nielsen, H. K., & Norum, L. E. (2013). Overirradiance (Cloud Enhancement) Events at High Latitudes. *IEEE Journal of Photovoltaics*, 3(1), 271–277. <https://doi.org/10.1109/JPHOTOV.2012.2213581>
- Yordanov, G. H., Saetre, T. O., & Midtgård, O.-M. (2013). 100-millisecond Resolution for Accurate Overirradiance Measurements. *IEEE Journal of Photovoltaics*, 3(4), 1354–1360. <https://doi.org/10.1109/JPHOTOV.2013.2264621>
- Yordanov, G. H., Saetre, T. O., & Midtgård, O. M. (2015). Extreme overirradiance events in Norway: 1.6 suns measured close to 60°N. *Solar Energy*, 115(June 2013), 68–73. <https://doi.org/10.1016/j.solener.2015.02.020>
- Zehner, M., Weigl, T., Thaler, S., Schrank, O., Czakalla, M., Mayer, B., Betts, T. R., Gottschalg, R., Behrens, K., Langlo, G. K., Giesler, B., Becker, G., & Mayer, O. (2011). Energy Loss Due to Irradiance Enhancement. *26th European Photovoltaic Solar Energy Conference and Exhibition, 1*, 3935–3938. <https://doi.org/10.4229/26thEUPVSEC2011-5AO.6.3>
- Zhang, Y., Su, J., Zheng, L., Li, R., Yu, B., & Shang, W. (2020). Analysis of high-voltage DC fuse's ageing characteristics under the overload pulse current carrying mode and the caused short-circuit failure in series-resonant converter power source. *International Journal of Electrical Power and Energy Systems*, 117(May 2019), 105604. <https://doi.org/10.1016/j.ijepes.2019.105604>

APPENDIX A. PV PANEL SIMULINK MODEL

This appendix presents Matlab Simulink models used in this thesis.

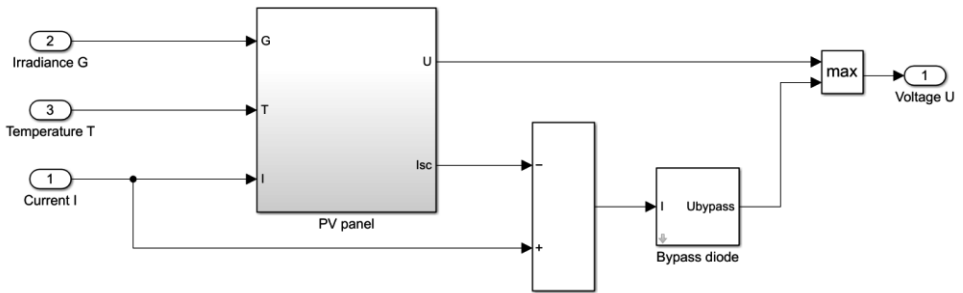


Fig. A.1. High level Matlab Simulink model of a PV panel composed of series-connected PV cells protected by an anti-parallel-connected bypass diode.

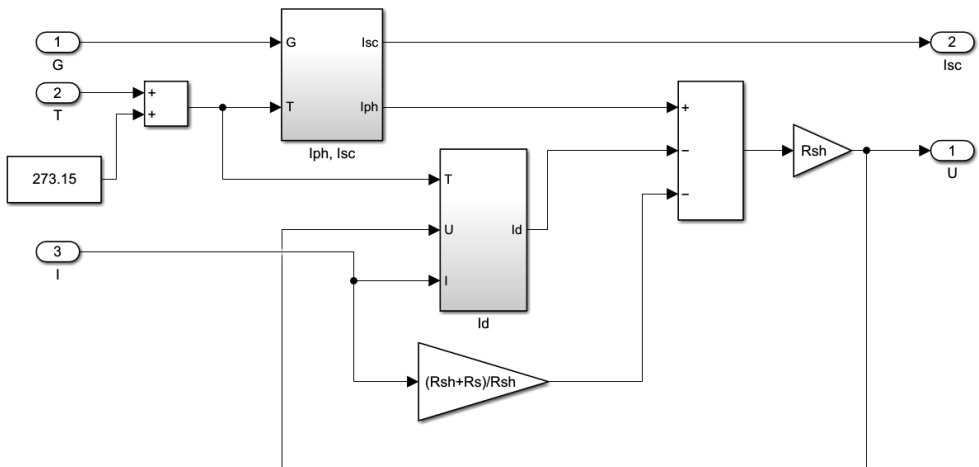


Fig. A.2. Matlab Simulink model of a PV panel subsystem.

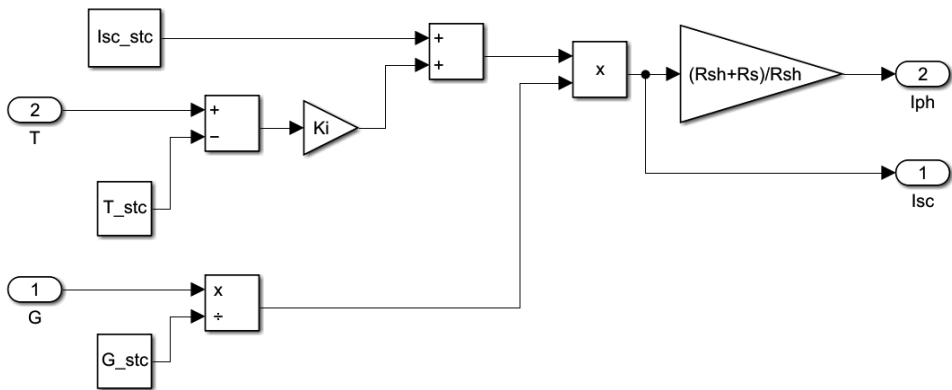


Fig. A.3. Matlab Simulink model of Iph, Isc subsystem

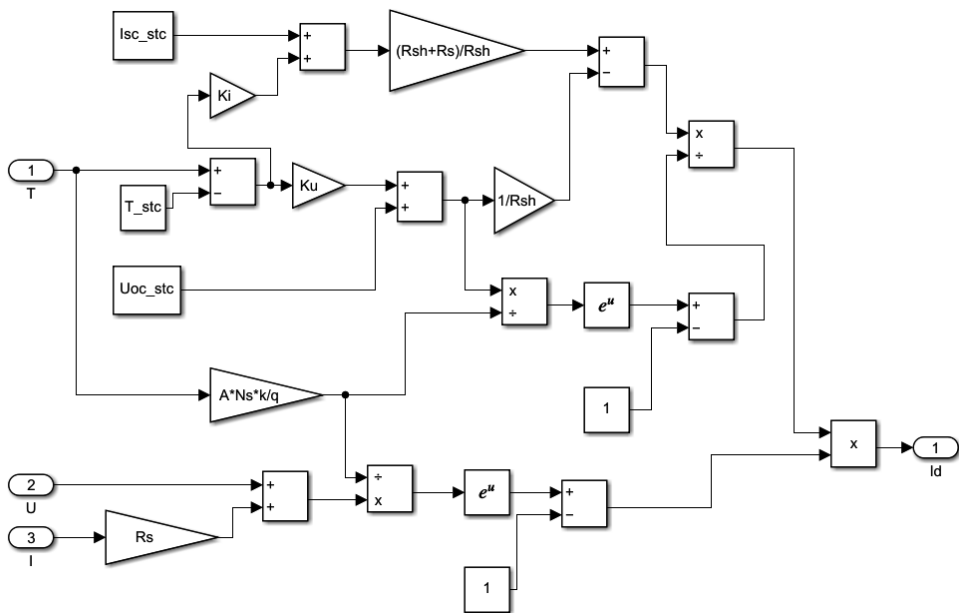


Fig. A.4. Matlab Simulink model of Id subsystem

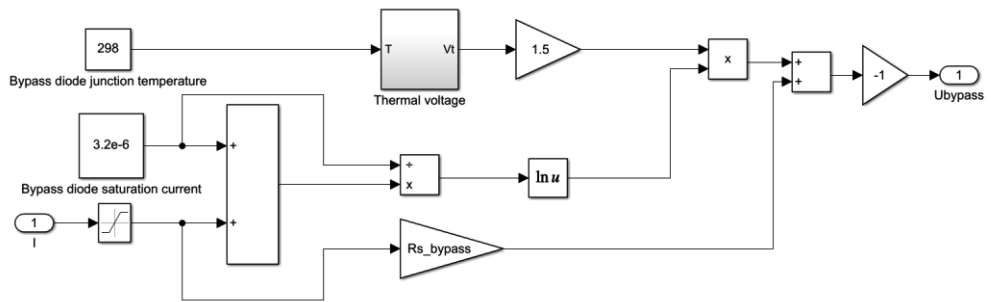


Fig. A.5. Matlab Simulink model of bypass diode subsystem

APPENDIX B. MATLAB FUNCTIONS

This appendix presents some of the Matlab functions used in this thesis.

```
function G = calculateIrradianceProfile(x, y, g)
% This function interpolates irradiance values between
% irradiance sensors
%
% x, y: coordinates of irradiance sensors
% g:    corresponding irradiance values

[X, Y] = meshgrid(min(x):max(x), min(y):max(y));
G = griddata(x, y, g, X, Y, 'linear');

end
```

```
function G = calculateAverageIrradiance(v, d, g, t)
% This function calculates the average irradiance based on
% the overirradiance area speed estimate and single-point
% irradiance measurement data
%
% v    Overirradiance area speed
% d    Diameter
% g    Irradiance
% t    time

T0 = t - d/.2./v;
T1 = t + d/.2./v;

G = zeros(1, length(t));
dt = zeros(length(t), 500);

for i = 1:length(T0)
    dt(i,:) = linspace(T0(i), T1(i), 500);
end

G = mean(interp1(t, g, dt)');

end
```

```

function [U, I] = seriesConnection(U, I, res)
% This function calculates I-U curve of series connected
% panels
%
% U(i,:)    Voltage of i:th panel.
% I(i,:)    Current of i:th panel.
% res       Resolution

dI = linspace(max(min(I')), min(max(I')), res);

[n, ~] = size(I);

for i = 1:n
    U_(i, :) = interp1(I(i,:), U(i,:), dI)
end

U = sum(U_);
I = dI;

end

```

```

function [U, I] = parallelConnection(U, I, res)
% This function calculates I-U curve of series connected
% panels
%
% U(i,:)    Voltage of i:th string.
% I(i,:)    Current of i:th string.
% res       Resolution

dU = linspace(min(max(U')), max(min(U')), res)

[n, ~] = size(U);

for i = 1:n
    I_(i, :) = interp1(U(i,:), I(i,:), dU)
end

I = sum(I_);
U = dU;

end

```